1-1-2015

Islanded Wind Energy Management System Based on Neural Networks

Ziqiao Liu
University of Denver

ISLANDED WIND ENERGY MANAGEMENT SYSTEM BASED ON NEURAL NETWORKS

A Dissertation

Presented to

the Faculty of the Daniel Felix Ritchie School of Engineering and Computer Science

University of Denver

In Partial Fulfillment

of the Requirements for the degree

Doctor of Philosophy

by

Ziqiao Liu

November 2015

Advisor: Dr. Wenzhong Gao

Author: Ziqiao Liu
Title: Islanded wind energy management system based on neural networks
Advisor: Dr. Wenzhong Gao
Degree Date: Nov 2015

Abstract

Wind power, as the main renewable energy source, is increasingly deployed and connected into electrical networks thanks to the development of wind energy conversion technologies. This dissertation is focusing on research related to wind power system include grid-connected/islanded wind power systems operation and control design, wind power quality, wind power prediction technologies, and its applications in microgrids. The doubly fed induction generator (DFIG) wind turbine is popular in the wind industry and thus has been researched in this Dissertation. In order to investigate reasons of harmonic generation in wind power systems, a DFIG wind turbine is modeled by using general vector representation of voltage, current and magnetic flux in the presence of harmonics. In this Dissertation, a method of short term wind power prediction for a wind power plant is developed by training neural networks in Matlab software based on historical data of wind speed and wind direction. The model proposed is shown to achieve a high accuracy with respect to the measured data. Based on the above research work, a microgrid with high wind energy penetration has been designed and simulated by using Matlab/Simulink. Besides wind energy, this microgrid system is operated with assistance of a diesel generator. A three-layer energy management system (EMS) is designed and applied in this microgrid system, which is to realize microgrid islanded operation under different wind conditions. Simulation results show that the EMS can ensure stable operation of the microgrid under varying wind speed situations.

Acknowledgments

This Dissertation is submitted to the Daniel Felix Ritchie School of Engineering & Computer Science at University of Denver as a fulfilment of the requirements for the Ph.D. degree in Electrical Engineering. The research has been conducted at the Department of Electrical Engineering, which is part of the Daniel Felix Ritchie School of Engineering & Computer Science at University of Denver.

Firstly I would like to thank my advisor Dr. Wenzhong Gao, who supports my PhD program as my advisor. I would like to express my gratitude to Dr. Eduard Muljadi, who is always giving me valuable advice on my wind energy research. And I am really appreciate help from Dr. Josep M. Guerrero, who develops me a lot especially on understanding of microgrid concept. Also, I would like to thank Dr. Peter Magyar, who gives me a chance to work for IEEE organization. Finally, I would like to thank my other committee members: Dr. Cynthia McRae, Dr. Mohammad Martin, Dr. Jun Zhang, for your attendance, support and questions. I gained valuable knowledge, ideas and inspiration from all those great people.

I gratefully acknowledge the funding sources that made my Ph.D. work possible. I was funded by the Department of Electrical Engineering, Daniel Felix Ritchie School of Engineering & Computer Science at University of Denver and National Science Foundation of USA Grant.

Finally, I owe many thanks to my parents and husband for all their love, understanding and supports in my pursuits, for periods where I have been apart away from them. Thank you!

Table of Contents

Chapter One: Introduction 1

1.1 Background and motivation 1

1.1.1 Wind turbine technology and control 2

1.1.2 Harmonics in wind power systems 4

1.1.3 Wind power prediction 5

1.2 Problem statement 6

1.3 Outline of Dissertation 7

Chapter Two: Wind power system and DFIG wind turbine control 10

2.1 Wind power from the air stream 10

2.2 Aerodynamic wind power control 12

2.3 Control of Doubly Fed Induction Generator Wind Turbine 12

2.3.1 Description of DFIG wind power system model 17

2.3.2 DFIG steady state equivalent circuit 21

2.3.3 PWM model 25

2.3.4 Control theory in DFIG wind turbine 26

2.3.5 Control results with DFIG wind power system 37

2.4 Summary 40

Chapter Three: Harmonic issues in DFIG wind turbines 41

3.1 Harmonics modeling in DFIG using the general vector representation form 43

3.1.1 Modeling with stator side 44

3.1.2 Modeling with Rotor Side 47

3.2 Harmonic resonance mode analysis in DFIG wind power system 53

3.3 Summary 61

Chapter Four: Wind power prediction by using neural networks 63

4.1 Data preparation 63

4.2 Neural network models for wind power prediction 74

4.3 Wind power prediction results 76

4.4 Summary 80

Chapter Five: Islanded wind power system with EMS 81
5.1 The microgrid concept 81
5.2 Wind powered microgrid description 83
5.3 Application of wind prediction for improving EMS performance 101

Chapter Six: Conclusions 112

Chapter Seven: Contributions and future work 115
7.1 Contributions of the Dissertation 115
7.2 Future work 118

References 120

List of Figures

Figure 1.1 Total installed capacity of wind energy in the world 2011-2014 [1]. 2
Figure 2.1 Wind turbine power output vs rotor speed for different wind speeds. 11
Figure 2.2 DFIG wind turbine structure. 19
Figure 2.3 Rotor side plot. 21
Figure 2.4 Stator side plot. 21
Figure 2.5 d-axis equivalent circuit. 25
Figure 2.6 q-axis equivalent circuit. 25
Figure 2.7 DFIG equivalent circuit. (Note: Ug represents the grid voltage.). 26
Figure 2.8 Structure of grid side converter. 28
Figure 2.9 dq frame at grid side. 29
Figure 2.10 Grid side control structure. 31
Figure 2.11 dq frame at rotor side. 32
Figure 2.12 Structure of rotor side control. 35
Figure 2.13 Internal model control structure. 37
Figure 2.14 Voltage (phase a) at DFIG wind turbine integration point. 40
Figure 2.15 DC link voltage. 41
Figure 2.16 Reactive power at the grid integration point. 42
Figure 2.17 Active power at grid integration point. 42
Figure 3.1 The self-magnetic flux in the stator winding of phase a. 49
Figure 3.2 The self and mutual magnetic flux of the stator winding of phase a. 49
Figure 3.3 The mutual flux from the rotor to the stator windings of phase a. 51
Figure 3.4 Area of interface between the stator and rotor poles. 52
Figure 3.5 Areas of interface for phase a stator poles to phase a rotor pole. 52
Figure 3.6 The three phase mutual fluxes from the rotor to the stator winding. 54
Figure 3.7 The window pulses of the rotor's three phases on stator's phase a. 54
Figure 3.8 DFIG equivalent circuit for HRMA. 60
Figure 3.9 Bus1-5. 62
Figure 3.10 Bus 6. 62
Figure 3.11 Harmonic filter. 64
Figure 3.12 HRMA results with passive filter. 65
Figure 4.1Wind power plant distribution. 70
Figure 4.2 Scatter plot wind speed vs. wind power from single wind turbine. 71
Figure 4.3 Structure of PNN. 73
Figure 4.4 Classification results of data in Fig. 4.2 by method 1. 75
Figure 4.5 Filtered scatter plot of Group 1 data points classified by method 1 (2010 Jan-Mar). 75
Figure 4.6 Classification results of data in Fig. 4.2 by method 2. 76

Figure 4.7 Filtered scatter plot of Group 1 data points classified by method 2 (2010 Jan-Mar). 77
Figure 4.8 Wind direction at 3/18/2010 10:00 PM. 80
Figure 4.9 Wind direction at 4/10/2010 8:40 AM. 80
Figure 4.10 Wind vector. 81
Figure 4.11 Recurrent neural network training structure. 82
Figure 4.12 Prediction results by 10-min time delay SP mode RNN. 87
Figure 5.1 Islanded wind power system under study. 93
Figure 5.2 Diesel engine and governor system [107]. 99
Figure 5.3 Wind speeds during black start. 101
Figure 5.4 Microgrid frequency transient response. 102
Figure 5.5 Diesel generator transient response (all in p.u.). 102
Figure 5.6 Rotor speed (p.u.) and pitch angle (degrees) of WT1. 103
Figure 5.7 Rotating speed (p.u.) and pitch angle (degrees) of WT2. 103
Figure 5.8 Circulating current concept. 104
Figure 5.9 f – P and V – Q droop control principle. 107
Figure 5.10 Block diagram of the secondary control in relation with the primary control. 107
Figure 5.11 Wind power generation of WT1 and WT2 (p.u.). 109
Figure 5.12 Frequency for microgrid and wind turbines. 110
Figure 5.13 Modules that integrate the energy management system. 112
Figure 5.14 Training process of the neural network. 114
Figure 5.15 Forecasting process to estimate the future wind power generated. 114
Figure 5.16 Predicted wind speed of 10 and 20 minutes in advance. 115
Figure 5.17 Predicted wind power of 10 and 20 minutes in advance. 116
Figure 5.18 Wind speed discretization process. 117
Figure 5.19 Pitch angle variations according to the changes of wind speed. 118
Figure 5.20 Rotor speed variations according to the changes in wind speed. 119
Figure 5.21 Microgrid frequency response according to wind variations. 120
Figure 5.22 Voltage regulation. 121
Figure 5.23 Diesel generator output power. 121
Figure 5.24 Wind turbine output power generated. 122

List of Tables

Table 2.1 DFIG vs. PMSG comparison. 14
Table 2.2 Parameters of the DFIG wind turbine. 39
Table 3.1 Wind power system parameters. 61
Table 3.2 Harmonic resonance point. 63
Table 3.3 Participation bus for harmonic resonance point. 63
Table 3.4 Harmonic filter parameters. 64
Table 4.1 Raw data classification. 70
Table 4.2 2010 Wind speed data analysis. 78
Table 4.3 Data for building prediction model. 83
Table 4.4 Prediction results analysis. 84
Table 4.5 Prediction results analysis. 84
Table 4.6 Prediction methods comparison. 85

Chapter One: Introduction

This Dissertation aims exploring an islanded wind power system modeling and design of energy system management (EMS) based on neural networks, which includes doubly fed induction generator (DFIG) wind turbines' control and modeling, harmonic analysis for DFIG wind energy systems, and power management by using wind power predictions from neural networks.

Background knowledge about wind power system based on previously published research papers and motivation for the research are presented in this Chapter. Also, the problem statement is given and an outline of each individual subchapter is given in this Chapter.

1.1 Background and motivation

Wind energy, which is friendly to the environment, plays an important role in the sustainable development of the world. In the past decades, the penetration of wind energy is increasing, so that it is beneficial to the electrical power systems if we make use of wind energy efficiently and safely.

According to a report from the World Wind Energy Association [1], 35 GW of new installations of wind turbine capacity installed in the second half of 2014, the world-wide wind capacity has reached 370 GW, as shown in Figure 1.1. The phenomena of increasing wind power may be due to windy weather of certain areas, is supported by governments and the development of wind power technologies. Those technologies could not be successful without the development of mechanical engineering, material sciences,

aerodynamics, power electronics, computer sciences, and testing and analytics methods [2] below. With the increasing wind power penetration, wind energy management systems need to be designed and implemented to cope with different supply-demand situations according to the following background.

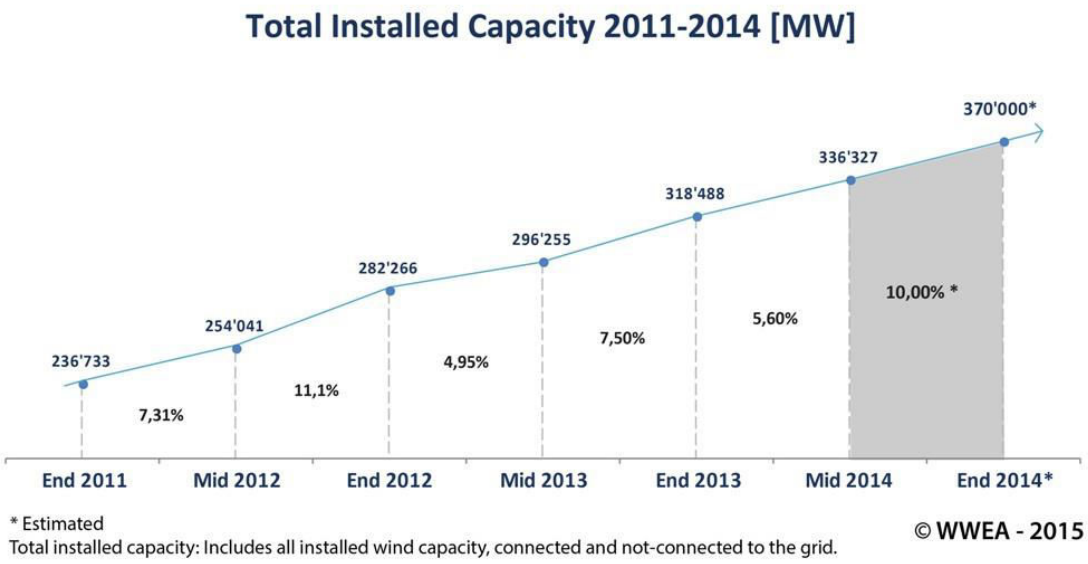

Figure 1.1 Total installed capacity of wind energy in the world 2011-2014 [1].

1.1.1 Wind turbine technology and control

Wind turbines can be operated under either fixed speed with a changing range about 1% or in variable speed [2]. For a fixed speed wind turbine, an induction generator is directly connected to the grid. A fixed speed wind turbine can hardly be controlled because the rotor speed is almost fixed by the grid frequency, which may not tolerate wind turbulences. As a result, the turbulences of the wind would result in power oscillations and instabilities and affect the power quality of the grid [3]. For a variable-speed wind turbine, power electronics equipment are often applied to control rotor speed of the generator so that the power fluctuations caused by varying wind speeds could be absorbed more or less by changing the rotor speed. Therefore, compared to the fixed

speed wind turbines, the power quality of the electricity generated by a variable speed wind turbine can be easily enhanced. The rotational speed of a wind turbine can be adjusted to match the electrical frequency specifications. There are two methods for adjusting the rotor speed: (i) by using a gearbox or (ii) by changing the number of pole pairs of the generator. The gearbox can adjust the rotor speed of the turbine to match the required mechanical speed of the generator. The number of pole pairs can set the mechanical speed of the generator with respect to the electrical frequency [2]. In practice, the rotor speed is controlled according to the needs of a certain wind turbine with a fixed number of pole pairs.

According to the differences between the aforementioned wind turbine structures, there are mainly four types of wind turbine technologies:

- Type1: Fixed speed wind turbine with an induction generator.
- Type2: Variable speed wind turbine equipped with a cage-bar induction generator or synchronous generator.
- Type 3: Variable speed wind turbine equipped with a doubly-fed induction generator (DFIG wind turbine).
- Type 4: Variable speed wind turbine equipped with multiple-pole synchronous generator or multiple-pole permanent magnet synchronous generator (PMSG) wind turbine.

In this Dissertation, type 3 DFIG based wind power systems are researched since it is very commonly used in practical installations due to the good balance between performances and cost.

1.1.2 Harmonics in wind power systems

In a DFIG wind turbine, controllers manipulate the rotor's voltage, current and frequency to ensure maximum power generation at a given wind speed. The rotor voltage is controlled by having an AC/DC converter connected from the grid to a DC bus, and then another DC/AC converter is applied to control the rotor current forming a back-to-back converter [4]. Consequently, harmonics are injected into the rotor side due to power electronics' operation.

Rotor currents, including fundamental component and its harmonics, are coupled with rotor mechanical speed and then transformed to the stator side through the air gap. Consequently, stator currents, fundamental and harmonics, are injected into the grid. Those harmonics are of great concern because they may degrade the quality of the wind power and have potential harmonic resonance frequency points, which may threaten the grid. This phenomenon will be analyzed in Chapter 4 of this Dissertation.

As most wind farms are installed in remote and/or rural areas, often are connected to weak grids with large impedance, so that the power quality problem becomes more dramatic[4]-[6]. In [6] high frequency and low frequency non-integer harmonics exist in DFIG wind power system is reported. The existence of non-integer harmonics is due to modulation of the low frequency rotor current, which is coupled with mechanical rotation speed. In Chapter 4, it is shown that when the two frequencies are coupled, a harmonic at the sum of the two frequencies is generated, which is the synchronous speed. Further, low frequency non-integer harmonics are generated based on the difference between the two frequencies.

According to IEEE519, under power systems 69kV and below, harmonic voltage distortion should be limited to 5% total harmonic distortion, where variable speed wind turbine could satisfy this standard [7].Harmonic resonance may generate over-voltages and/or currents in the wind power system, which would damage equipment and has a high potential risk. Harmonic resonance modal analysis (HRMA) is an analysis method to detect harmonic frequency in power systems [8]. Any distribution feeder system will present its own resonance frequency due to different modes of the system impedance. HRMA provides useful information for mitigating potential harmonic resonance danger. In this Dissertation, harmonic resonance phenomena are analyzed and discussed in a DFIG wind power system and the conclusion maybe used for designing filters in wind power systems.

1.1.3 Wind power prediction

Due to different geographical patterns, weather, and properties of a wind power plant (WPP), two wind turbines of the same type would present different performances given different situations. If the wind power generation can be predicted with high accuracy, more useful information can be provided to energy management system. This information will allow a more flexible and intelligent control of wind turbines, e.g., improve the working schedule of wind turbines, active/reactive power control, etc. Methods for predicting wind power generation can be categorized into physical methods, statistical methods, methods based on neural networks, and hybrid methods [9].

Physical methods rely heavily on numeric whether predictions, which are limited by the sensors and monitoring devices placed within the wind turbine. The quality of the hardware chosen, parameter settings, computation time, time delays and sampling rates

influence the accuracy of data collected from the wind turbine. It is easier to predict a single wind turbine's performance rather than a whole wind power plant's power generation [10]. Statistical and neural network methods are based on the historical data and have a low prediction cost. The relationship between input data and output data based on historical measured data is researched and then a nonlinear relationship model between them is built. When new data that is not previously included in the training data set, and is used as input into this kind of model, the prediction error might be larger. The different abovementioned prediction methods can be combined forming hybrid methods to achieve better prediction results, while increase the complexity of the model. In Chapter 5, the recurrent neural network approach is applied to predict wind power generation of a DFIG-based wind turbine based on wind profile data obtained from a wind power plant located in northeast Colorado.

1.2 Problem statement

The integration of wind power as a distributed generator (DG) into the distribution electrical network is changing the structure of the grid. Firstly, wind speed variations may have a significant influence on the amount and quality of wind power generated. Sudden changes of wind power can lead to a losses or increase of power generation, which may cause voltage and frequency disturbances, resulting in dramatically unstable situations and trip relays inside the grid [11]. For instance, FERC 661-A requires wind power system operating at power factors greater than 0.95 [12], so that many wind farm operators currently prefer to work constantly at the unity power factor [13][14].

A wind power system can be better developed with deep understanding of its operation mechanism. Therefore, the first aim of this research is to study and design an efficient control method for DFIG wind turbines and to realize active power frequency and reactive power voltage control of wind power under stochastic weather conditions.

The increasing DG penetration into the grid promotes the development of a new grid concept, called microgrid. A microgrid consists of DGs and controllable loads, being an integrated energy delivery system that can work independently from the main power grid [15]. DGs in a microgrid reduce the transmission losses and increase distribution efficiency with the proper power management. So that an energy management system (EMS) can assist a microgrid operating in either grid-connected or islanded modes, as well as in the smoothly transfer between those modes. The main task of an EMS is to manage the power and energy between sources and loads in a microgrid [16]. The intermittency of wind power raises new challenges in microgrid operation and control, especially during high wind power penetration. To have a good understanding of coordinated operations of multiple DFIG wind turbines within a microgrid in islanded mode, the second aim of this research is to build an EMS for an islanded wind power system to realize power sharing among DFIG wind turbines with assigned active and reactive power references. In this EMS of the islanded wind power system, wind power prediction technique will be implemented to improve active and reactive powers profile in advance before control action is done.

1.3 Outline of Dissertation

The research of this Dissertation is to deal with the abovementioned problems. The outline of this Dissertation is described as follows.

- Chapter 1: Introduction.

The background and motivation for the research presented in this Dissertation have been introduced along with a general description of the published research work related to wind power. Next problem statement and outlines of this Dissertation are introduced.

- Chapter 2: Wind power system and DFIG wind turbine control

Wind energy conversion system is introduced and how wind power is related to wind speed, power co-efficiency, pitch angle, wind turbine parameters, and so forth. The DFIG wind turbine model is presented, which employs two back-to-back power electronic converters and allows reactive power exchange with the network. Control blocks in rotor part and stator part of DFIG with vector control schemes are designed by using conventional PI controllers and the internal model control (IMC) principle. The performance of the control algorithms are described in detail.

- Chapter 3: Harmonic issues in DFIG wind turbines

The reason for harmonic generation in DFIG wind turbine are analyzed, and then a DFIG wind turbine including harmonic emissions is modeled by using generator vector representation. The potential problems caused by harmonic emissions in DFIG wind turbines are analyzed by using harmonic resonance mode analysis (HRMA), which can find out the harmonic resonance frequency point and corresponding mitigation method is proposed to enhance the wind power system reliability.

- Chapter 4: Wind power prediction by using neural networks

Wind power estimation plays an important role in EMS, helping to set references power generation points in the islanded wind power system. In this Chapter, a neural network is applied to build a wind power prediction system with wind profile data (wind

speed, wind direction, and wind power generation) provided by the National Renewable Energy Lab. Prediction results are compared with the measured wind power generation, which are achieved with an acceptable accuracy.

- Chapter 5: Islanded wind power system with EMS

An islanded wind power system with harmonic mitigation blocks is built, which includes wind power generator, auxiliary generator and a variable load. This Chapter is to investigate how DFIG wind turbines operate under reference power point set by EMS, and how EMS set power references by using load sharing method with the help of wind power prediction and how DFIG wind turbines track power references under changing wind speeds.

Chapter Two: Wind power system and DFIG wind turbine control

Power generation produced by a wind turbine depends on the interaction between the wind and the turbine rotor. The blades of a wind turbine rotor extract some of the energy flow from air in motion, convert it into rotational energy, and then deliver it via a mechanical drive unit into the generator.

2.1 Wind power from the air stream

Wind turbine could obtain velocity and absorbs energy from the air stream of wind. It is a complex aerodynamic system in which rotor of the wind turbine extracts the energy from the wind and converts it into mechanical energy.

The relationship between the wind speed and aerodynamic power may be described by the following equation:

$$P_{wt} = \frac{1}{2}\rho\pi R^2 v^3 C_p(\theta,\lambda) \tag{2.1}$$

The corresponding aerodynamic torque can be expressed as:

$$T_{wt} = \frac{P_{wt}*R}{\lambda*v} \tag{2.2}$$

where

P_{wt} : aerodynamic power extracted from the wind [W]

T_{wt} : aerodynamic torque extracted from the wind [Nm]

ρ : air density [kg/m^3]

R : wind turbine blade radius [m]

v : equivalent wind speed [m/s]

θ: pitch angle of rotor [deg]

λ: tip speed ratio$\lambda = \omega_r R/v$, where ω_r is the wind turbine rotor speed [rad/s]

C_p: power coefficient, which is approximated with given values of θ and λ[17][18]as follows

$$C_p(\theta,\lambda) = 0.22\left(\frac{116}{\lambda_1} - 0.4\theta - 5\right)e^{-\frac{12.5}{\lambda_i}} \tag{2.3}$$

$$\lambda_i = \frac{1}{\frac{1}{\lambda+0.08\theta} - \frac{0.035}{\theta^3+1}} \tag{2.4}$$

The curves family of P_{wt} –ω_r for a 1.5 MW wind turbine at different wind speeds are shown in Figure 2.1. Notice that there is a maximum power point for each given wind speed. E.g. at 12 m/s, maximum power can be found at 1.2 p.u. turbine speed.

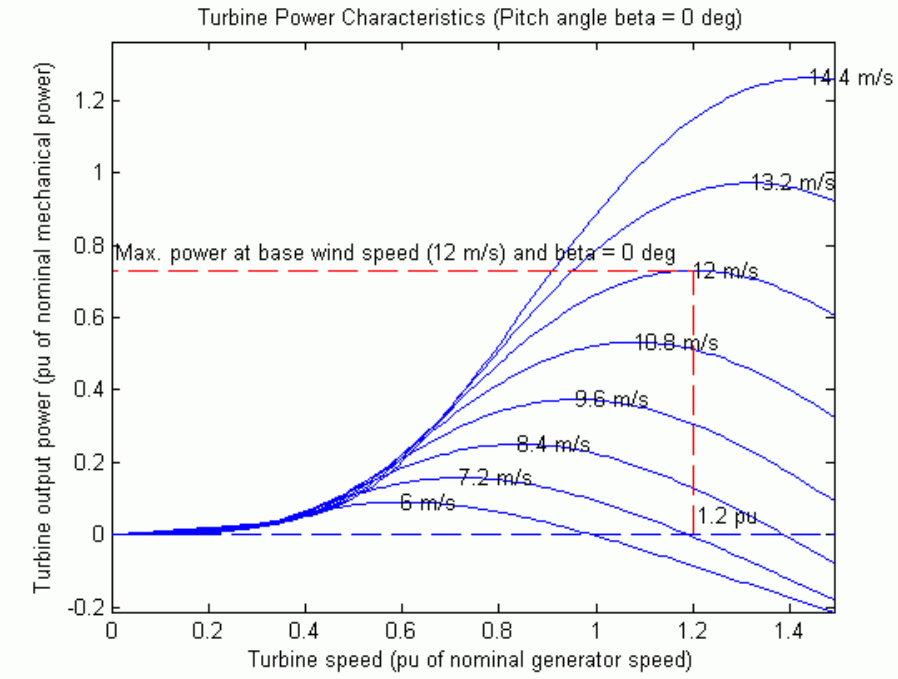

Figure 2.1 Wind turbine power output vs rotor speed for different wind speeds.

2.2 Aerodynamic wind power control

Aerodynamic control is used to limit power absorption in wind turbines during high wind speed scenarios. The three major approaches used in aerodynamic control are passive stall control, pitch control, and active stall control [19]. In passive stall control, the wind turbine blades are supposed to stall in high wind speed period and no pitch control is required. Pitch control is the most common method especially in applications for variable wind speed turbines. When wind speed is below the rated wind speed, the wind turbine can maximize the captured wind energy by using pitch angle control. When the wind speed reaches the rated wind speed, the pitch angle of wind turbine is controlled to keep the aerodynamic power at its rated value. Active stall control is applied to tune fixed speed wind turbine during high wind speeds and then limit the aerodynamic power.

2.3 Control of Doubly Fed Induction Generator Wind Turbine

Variable wind speed wind turbines are popular in wind power system application, which include DFIG type wind turbine and permanent magnet induction synchronous generator (PMSG) type wind turbine. Nowadays, DFIG wind turbine represents the 50% of the worldwide wind power market [20]. The range of DFIG wind turbine's rated power is mostly within 1.5-3.0 MW [20]. Compared to fixed speed wind turbines, variable speed wind turbines have more possibilities in handling a wide range of wind speeds. Compared to PMSG wind turbines, DFIG wind turbines are equipped with gearbox, which decreases the reliability due to the potential mechanical problems. However, DFIG wind turbines need only partial scale converters (about 30% of the nominal power), while PMSG needs to be equipped with full scale converters, Thus, DFIG are economically more feasible, which is the main reason for the popularity of this

kind of generators in practical wind energy applications. A more detailed comparison maybe seen in Table 2.1[21].

Table 2.1DFIG vs. PMSG comparison.

	DFIG	PMSG
Pros	• Speed range is±30% around synchronous speed • Low cost, small capacity (less than 30%) PWM converter • Active, reactive power can be controlled completely	• Have full speed range • Possible to remove gear • Active, reactive power can be controlled completely • Brushless
Cons	• Potential mechanical problems due to: ➢ Slip rings ➢ Gear box	• Full scale power converter • Big and heavy multi-pole generator • Need permanent magnetics

Control approaches for DFIG wind turbines have been researched under different situations, such as wind power system in grid connection mode, islanded wind energy system operation and control, low voltage ride through (LVRT) performance of wind power system, and so on. Currently, DFIG wind turbine energy management in islanded mode microgrids, DFIG sensorless controllers, DFIG optimum switching controllers, droop control, and DFIG performance under unbalanced load situations are promising research topics [20][21].

The main purpose of controlling DFIG wind turbines is to generate quality electricity to supply the demanded load. However, due to the variations of wind speed, different load situations, and poorly damped eigenvalues (poles) in the dynamics of DFIG wind turbines with an operation frequency near the line frequency, DFIG wind power system may present unstable performance under some operation conditions[22][23]. Moreover, rotor current/voltage would be reduced by the stator-to-rotor turns ratio. The reduced rotor voltage may limit the DFIG's ability to handle voltage sags [23].

The most common control approach for DFIG control is based on a vector control method, with PI regulators and a phase locked loop (PLL) to achieve equality of voltage magnitude, phase, and frequency that comply with the grid standards[24]-[26]. The conventional vector control method is based on rotor current vector control with d-q decoupling [27]-[29], [30]-[33]or stator flux orientation to control rotor current [34],[35]or air gap flux to control rotor current[36].

The control system is usually defined in the synchronous d-q frame with the d-axis fixed to either the stator voltage [27], [28] or the stator flux [29], and it involves relatively complex transformation of voltages, currents and control outputs among the stationary, the rotor and the synchronous reference frames. This conventional vector control method requires accurate information of machine parameters such as stator, rotor resistance, inductance, mutual inductance, and so forth. Thus, the performance is degraded when actual machine parameters differ from those values used in the designed control system. In addition, the rotor current controllers need to be carefully tuned to ensure system stability and adequate response within the whole operating range.

The research presented in [27]-[29] show conventional controller design of DFIG wind turbine based on rotor current vector control with d-q transformation. But if the stator resistance can be considered small, stator-flux orientation is considered with the stator voltage [37], [38], [39]. The stator flux could be influenced and has damped oscillation when load or stator power changes [35].

Besides conventional vector control method for DFIG, the most widely used control for RSC are direct control techniques such as direct torque control (DTC)

[40][41]and direct power control (DPC) [42], [43]. Those techniques do not require current PI regulators, coordinate transformations, or specific modulation in PWM converters. DTC achieves better steady state and transient torque control performance, but it presents the drawback of variable switching frequency control which might be improved by using predictive control [44].

The DTC method for induction machines was developed in the mid-1980s [45][46]. DTC method eliminates the parameter tuning and machine parameters dependence, while requiring no PI controllers for active or reactive power control. The machine torque is controlled directly by selecting appropriate voltage vectors with the stator flux and torque information. The stator flux is usually calculated according to the stator voltage. One of the main problems associated with the basic DTC scheme is that its performance deteriorates during starting and at very low speed operation. This is largely due to the fact that the method repeatedly selects zero voltage vectors at low speed resulting in flux level reduction owing to a lower value of stator resistance [47]. Several methods have been applied to solve this problem, such as dither signal [48], modified switching tables to apply available voltage vectors in accordance [49], or predictive methods, among others. Moreover, DTC could also be applied to control PMSG [50] and switched reluctance motors [51].

In [52], DTC is used to control a DFIG as follows. The converter is connected to the rotor side within a DFIG system, and the rotor flux is estimated. The rotor flux reference was calculated based on the required operating power factor. A switching factor was then selected from the optimal switching table based on the estimated rotor flux

position, the torque and the rotor flux errors. Since the frequency of the rotor supply, which is equal to the DFIG slip frequency, could become very low, the rotor flux estimation method presents difficulties, and its accuracy is significantly affected by machine parameter variations. Furthermore, the calculation of the rotor flux reference according to the required power factor also requires the availability of actual parameters and, therefore, has the same problem.

In [53], a grid-connection control strategy for frequency and a voltage control in DFIG wind system based on the direct control of both a virtual torque and rotor flux of the generator are presented. This control is achieved with no PI regulators and only requires the measurement of grid voltages for grid synchronization. From the performance of torque control, it is seen that mechanical constrains and wear process on the gearbox are reduced [54].

A DTC approach for grid connection case has been presented in [55], which relies on a switching table, but still needs PI regulators for active and reactive power control, information of rotor position and currents, and both stator and grid voltage measurements.

Based on the principles of DTC for electrical machine drives, direct power control (DPC) for three phase PWM rectifiers was proposed in [56]-[58]. In [56], the converter switching states are selected from an optimal switching table based on the instantaneous errors between the reference and estimated values of active and reactive power, and the angular position of the estimated converter terminal voltage vector. The converter terminal voltage is estimated using the dc link voltage and converter switching states, so that no voltage sensor is required. In [58], output regulation subspace (ORS) is used to

modify the original vector position for selecting the switching states to improve the system performance, especially under distorted or unbalanced supply conditions.

In a new direct power control method proposed by [36], stator active and reactive power controls are realized by adjusting rotor side voltage vectors, which show effectiveness and robustness during variations of active and reactive power, rotor speed, machine parameters, and converter dc link voltage cause by wind fluctuations.

Reference [34] proposes a new DPC control method for a DFIG based wind energy generation system, which is based on the stator flux and only needs the value of stator resistance. This control strategy eliminates the rotor flux estimation procedure. An optimal switching table has been derived and two three-level hysteresis comparators are used to determine the power errors. Simulation results presented confirm the effectiveness and robustness of the proposed DPC strategy during various operating conditions and variations of parameter and converter dc link voltage.

In this Dissertation, a modified vector control is applied for individual DFIG wind turbine control in order to maintain the voltage stability in a microgrid system.

2.3.1 Description of DFIG wind power system model

The most common structure of variable-speed wind generation of DFIG type wind turbine is as shown in Figure 2.2.

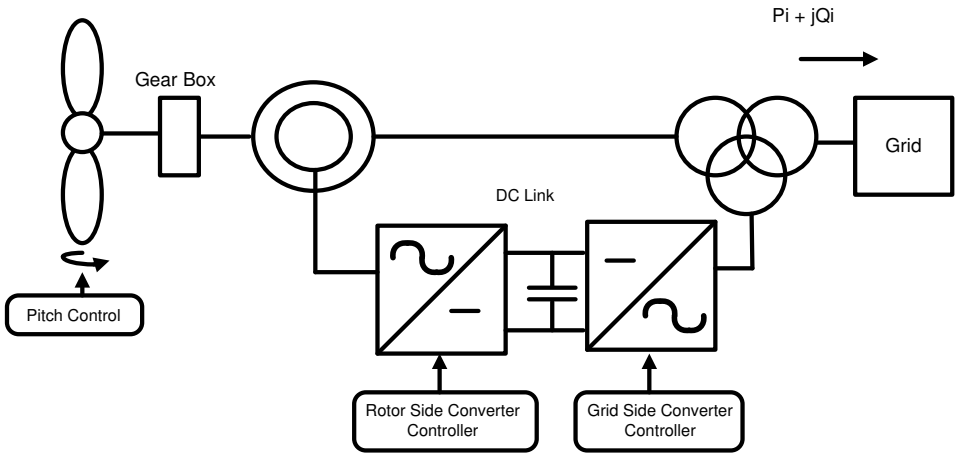

Figure 2.2 DFIG wind turbine structure.

A DFIG consist on a wound rotor induction generator and two pulse width modulation (PWM) voltage source current-regulated converters that are connected back to back between rotor and grid. The rotor side converter can work at different frequencies, according to the speed of the blade. The grid side converter works at grid frequency (leading or lagging so as to produce more or less reactive power). By operating the rotor circuit at a variable AC frequency one is able to control the mechanical speed of the machine; the rotor could have below, above and through synchronous speed so as to exchange power with grid in both directions; the rotor side converter could realize independent control of the generator torque and reactive power; power factor of the DFIG wind system could be adjusted according to converter control strategy. For a variable speed wind turbine with doubly fed induction generator, it is possible to control the torque at the generator directly, so that the speed of the turbine rotor can be varied within certain limits (±30%).

A three winding transformer is needed to connect the grid side converter, the stator and the supply side. In this design the net power out of the machine is a

combination of the power coming out of the machine's stator and that from the rotor and through the converter into the grid system.

An advantage of variable speed wind turbine is that the rotor speed can be adjusted in proportion to the wind speed in low to moderate wind speeds so that optimal tip speed ratio is maintained. At this tip speed ratio the aerodynamic efficiency, Cp, is at the maximum, which means that the energy conversion is maximized. In general, variable speed wind turbines may have two different control goals, depending on the wind speed. In low to moderate wind speeds, the control is to maintain a constant optimum tip speed ratio for maximum aerodynamic efficiency. In high wind speeds, the control goal is the maintenance of the rated output power with the aid of turbine blade pitch angle control. The performance of DFIG is quite different from conventional induction generators.

DFIG has been usually applied in environments that require high power transmission and a relatively narrow range of speed. Operations at different speeds have several advantages: rotor speed could be adjusted according to wind speed in order to improve wind turbine's efficiency; mechanical stress could be reduced and torque oscillations are not transmitted to the grid.

The control purpose is to make sure DFIG supply constant voltage with grid frequency at the terminal of stator regardless of shaft speed. A decoupled orthogonal control using field-oriented techniques can be used leading to direct control of the active power and reactive power of DFIG wind turbine.

In modern wind power plants, currents at converters are controlled using conventional vector control methods. In the rotor side, the current is decoupled into two

components: (i) $i_{dr}(\varphi)$ controls the machine excitation, which is in phase with the stator flux linkage; and (ii) $i_{qr}(\varphi)$ in quadrature with $i_{dr}(\varphi)$, which controls the electric torque. Figure 2.3 shows the plot of relationships between the rotor current I_r, the stator flux linkage φ_s, currents vector applied in the control system $i_{dr}(\varphi)$ and $i_{qr}(\varphi)$, a synchronous rotating reference frame {d, q} which forms an angle ϕ with respect to φ_s, and currents in such reference frame i_{dr} and i_{dr}.

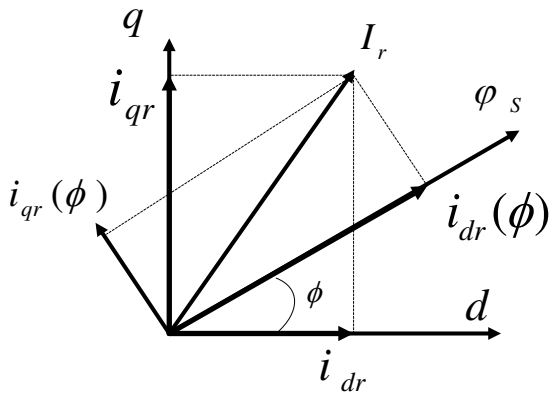

Figure 2.3 Rotor side plot.

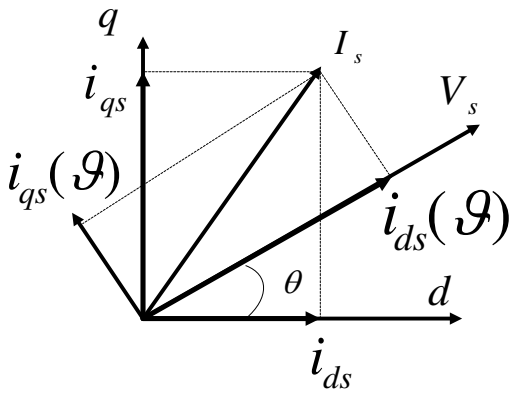

Figure 2.4 Stator side plot.

In the grid side, the current is also decoupled into two components: (1) $i_{ds}(\theta)$ controls the active power/ DC-link voltage level, which is in phase with the stator voltage; and (2) $i_{qs}(\theta)$ in quadrature with $i_{ds}(\theta)$, which controls the reactive power. Figure 2.4 shows the plot of relationships between the stator voltageV_s, the grid side converterI_s, current components used by the control system $i_{ds}(\theta)$ and $i_{qs}(\theta)$, a synchronous rotating frame {d,q} which forms an angle θ with respect to V_s, and current in such reference framei_{ds} and i_{qs}.

2.3.2 DFIG steady state equivalent circuit

Two assumptions are made for building the DFIG steady state equivalent circuit. The first assumption is that the current control loop responds faster than the electro mechanical transient response, so that it could be considered as instantaneous [40]. This is because the time constant of the converter current control loops are very small, i.e. in terms of milliseconds, and the time constant involved in transient stability studies is in terms of seconds. Moreover, fast dynamics of control process do not affect the electromechanical oscillations. The second assumption is that electromechanical transients among stator, converter, and grid can be neglected, which is a common simplification method in transient stability analysis of synchronous and asynchronous machines [41], [42].

The equivalent circuit model is based on the basic equations of the asynchronous machine. These equations are expressed in a reference frame aligned with synchronous speed, and taking positive currents. The machine equations can be written in the synchronous rotating *d-q* reference frame as follows:

$$\varphi_{ds} = L_s i_{ds} + L_m i_{dr} \; ; \; \frac{d\varphi_{ds}}{dt} = L_s \frac{di_{ds}}{dt} + L_m \frac{di_{dr}}{dt} \tag{2.5}$$

$$\varphi_{qs} = L_s i_{qs} + L_m i_{qr} \; ; \; \frac{d\varphi_{qs}}{dt} = L_s \frac{di_{qs}}{dt} + L_m \frac{di_{qr}}{dt} \tag{2.6}$$

$$\varphi_{dr} = L_m i_{ds} + L_r i_{dr} \; ; \; \frac{d\varphi_{dr}}{dt} = L_m \frac{di_{ds}}{dt} + L_r \frac{di_{dr}}{dt} \tag{2.7}$$

$$\varphi_{qr} = L_m i_{qs} + L_r i_{qr} \; ; \; \frac{d\varphi_{qr}}{dt} = L_m \frac{di_{qs}}{dt} + L_r \frac{di_{qr}}{dt} \tag{2.8}$$

$$u_{ds} = R_s i_{ds} + \frac{d\varphi_{ds}}{dt} - \omega_s \varphi_{qs} \tag{2.9}$$

$$u_{qs} = R_s i_{qs} + \frac{d\varphi_{qs}}{dt} + \omega_s \varphi_{ds} \tag{2.10}$$

$$u_{dr} = R_r i_{dr} + \frac{d\varphi_{dr}}{dt} - (\omega_s - \omega_r)\varphi_{qr} \tag{2.11}$$

$$u_{qr} = R_r i_{qr} + \frac{d\varphi_{qr}}{dt} + (\omega_s - \omega_r)\varphi_{dr} \tag{2.12}$$

$$T_{em} = \varphi_{qr} i_{dr} - \varphi_{dr} i_{qr} = \frac{3}{2} p L_m \left(i_{qs} i_{dr} - i_{ds} i_{qr}\right) \tag{2.13}$$

$$s = \frac{\omega_s - \omega_r}{\omega_s} \tag{2.14}$$

$$L_s = L_{s1} + L_m \; ; \; L_r = L_{r1} + L_m \tag{2.15}$$

being,

φ_{ds} , φ_{qs} : the stator flux linkage φ_{dr} , φ_{qr} : the rotor flux linkage

u_{ds}, u_{qs} : the stator voltage u_{dr}, u_{qr}: the rotor voltage

i_{ds}, i_{qs}:the stator current i_{dr}, i_{qr}: the rotor current

ω_s: the synchronous speed ω_r: the rotor speed s: rotor slip

L_s, R_s : stator inductance, stator resistance L_m: mutual inductance

L_r, R_r : rotor inductance, rotor resistance p: number of pole pairs

L_{s1}, L_{r1}: leakage inductance in stator side and rotor side

When the equations (2.5)-(2.15) are applied in the analysis, assumptions would be made and noticed. Stator flux linkage angle would be developed based on $\varphi_{ds}, \varphi_{qs}$, which is related to perform the change of the reference frame in the rotor side controller; $\frac{d\varphi_{ds}}{dt}$ and $\frac{d\varphi_{qs}}{dt}$ in (2.9) and (2.10) would be removed, so that the stator transients could be neglected. Since the rotor current is an independent variable in the rotor current control loop, expressions regarding$\varphi_{dr}, \varphi_{qr}, u_{dr}, u_{qr}$ are removed from the (2.5)-(2.8), (2.11) and (2.12).

The active and reactive powers in stator part and rotor part could be calculated as below, by considering$P_r = sP_s$:

$$P_s = \frac{3}{2}\left(u_{ds}i_{ds} + u_{qs}i_{qs}\right) \tag{2.16}$$

$$Q_s = \frac{3}{2}\left(u_{qs}i_{ds} - u_{ds}i_{qs}\right) \tag{2.17}$$

$$P_r = \frac{3}{2}\left(u_{dr}i_{dr} + u_{qr}i_{qr}\right) \tag{2.18}$$

$$Q_r = \frac{3}{2}\left(u_{qr}i_{dr} - u_{dr}i_{qr}\right) \tag{2.19}$$

Equivalent circuits for *d* and *q* axes can be set up according to the above mentioned equations (2.16)-(2.19) and are shown in Figure 2.5, Figure 2.6, and Figure 2.7.

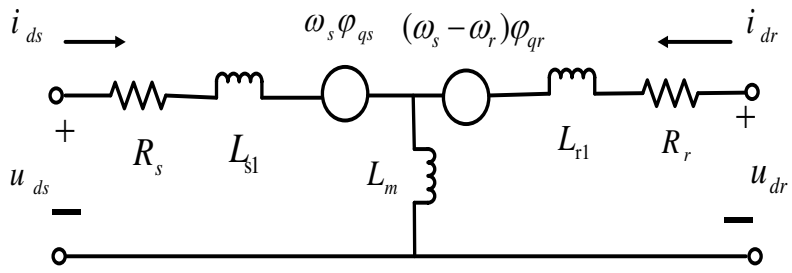

Figure 2.5 d-axis equivalent circuit.

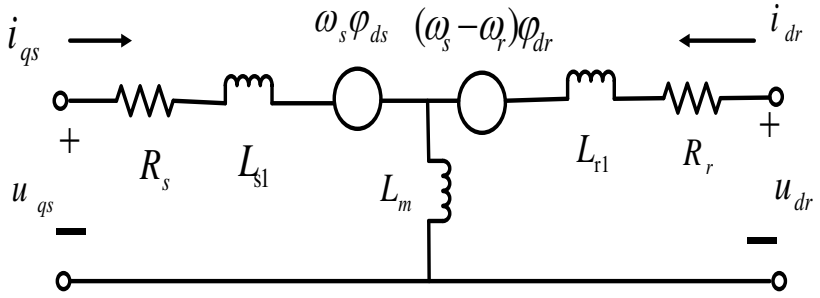

Figure 2.6 q-axis equivalent circuit.

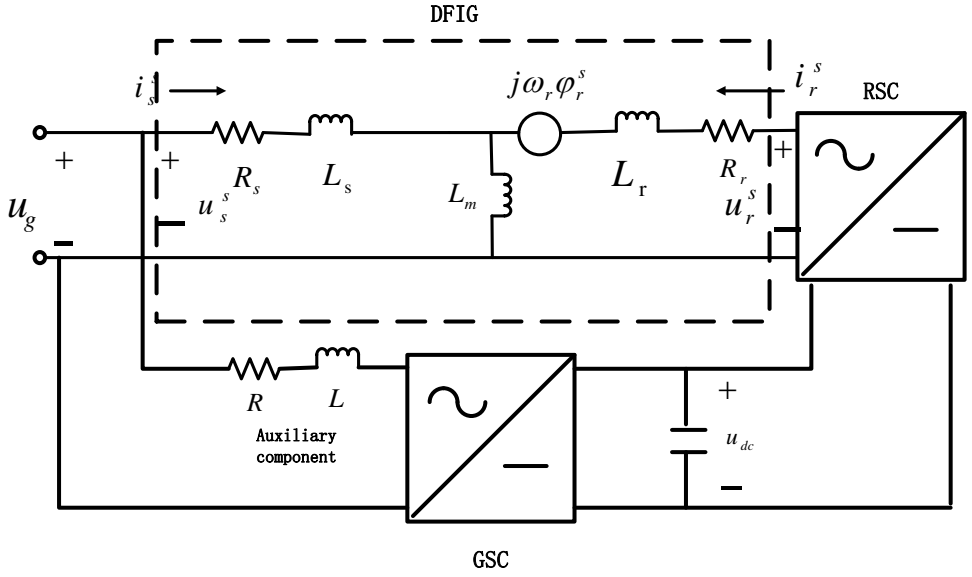

Figure 2.7 DFIG equivalent circuit. (Note: Ug represents the grid voltage.).

2.3.3 PWM model

The back-to-back connected PWM voltage source converters could reduce harmonic generation shortcomings of most converters. Magnitude and frequency of sinusoidal AC output voltage from the PWM could be controlled though the PWM converter switches. Detailed information of PWM voltage source converter model could be checked in [45], [46].

The switches in PWM voltage source converter are switched on and off at high frequency (few kHz or higher) during operation, which needs a very small simulation step to represent the PWM waveform results a fairly slow simulation step. In this Dissertation, PWM voltage source converter is not the main focus, an average model which is based on energy conversion theory without taking into consideration the switch is built in order to allow using larger simulation steps [47].

According to the energy conversion theory, PWM voltage source converter is assumed ideal without loss in this Dissertation, converter DC side instantaneous power must be equal to that of the AC side as shown below.

$$u_{dc}i_{dc} = u_a i_a + u_b i_b + u_c i_c \tag{2.20}$$

where

u_{dc}, i_{dc}: DC-link voltage and current

$u_a, u_b, u_c, i_a, i_b, i_c$: three phases AC voltages and currents

According to (2.20), the DC side current can be calculated. The DC-link voltage can be calculated based on DC side current and the capacitor in the DC-link, which could be DC-link voltage control reference value.

2.3.4 Control theory in DFIG wind turbine

A. Grid side converter control

The control purpose in the grid side converter is to maintain DC-link voltage regardless of the rotor side power situation. In the vector control in the grid side, the control reference frame is along the stator voltage position, enabling independent control of the active and reactive power flowing between the grid and grid side converter. The d-axis control is used to regulate the DC-link voltage and the *q*-axis control is used to regulate the reactive power.

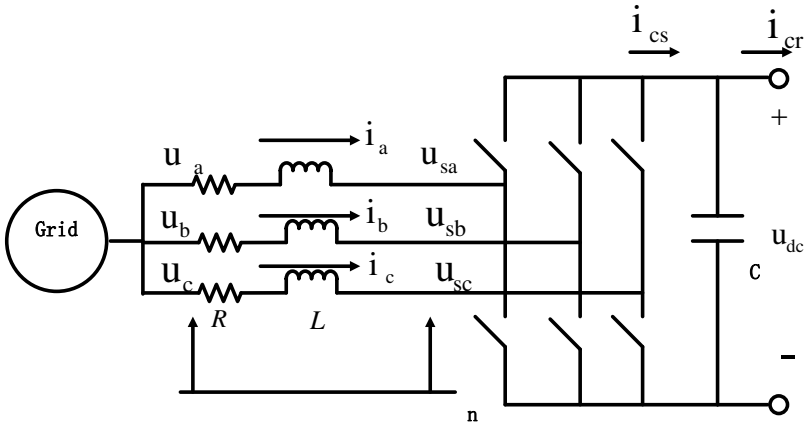

Figure 2.8 Structure of grid side converter.

From the power stage of the grid side converter shown in Figure 2.8, we can write the following three-phase (in *abc* coordinates) model:

$$\begin{bmatrix} u_{sa} \\ u_{sb} \\ u_{sc} \end{bmatrix} = R \begin{bmatrix} i_a \\ i_b \\ i_c \end{bmatrix} + L \frac{d}{dt} \begin{bmatrix} i_a \\ i_b \\ i_c \end{bmatrix} + \begin{bmatrix} u_a \\ u_b \\ u_c \end{bmatrix} \tag{2.21}$$

where *L* and *R* the grid side inductor and its equivalent series resistor.

By using *abc-dq* transformation, voltage equations in *dq* form could be developed below, u_{ds}' and u_{qs}' are the reference values for the supply side converter, and the terms in brackets constitute voltage compensation terms.

$$u_{ds} = Ri_{ds} + L\frac{di_{ds}}{dt} - \omega_s Li_{qs} + u_{ds1} \tag{2.22}$$

$$u_{qs} = Ri_{qs} + L\frac{di_{qs}}{dt} + \omega_s Li_{ds} + u_{qs1} \tag{2.23}$$

Assume $u'_{ds} = u_{ds} + \omega_s Li_{qs} - u_{ds1}$, and $u'_{qs} = u_{qs} - \omega_s Li_{ds} - u_{qs1}$, then $u'_{ds} = Ri_{ds} + L\frac{di_{ds}}{dt}$, $u'_{qs} = Ri_{qs} + L\frac{di_{qs}}{dt}$.

From equations above, the transfer equation of the plant for the current control loop can be obtained as follows:

$$f(s) = \frac{i_d(s)}{u'_{ds}(s)} = \frac{i_q(s)}{u'_{qs}(s)} = \frac{1}{Ls + R} \tag{2.24}$$

The active Ps and reactive Qs power flow between the grid and the grid side converter have already been given before. The angular position θ_s of the stator voltage is calculated as

$$\theta_s = \int \omega_s \, dt = \tan^{-1}\frac{u_{\beta s}}{u_{\alpha s}} \tag{2.25}$$

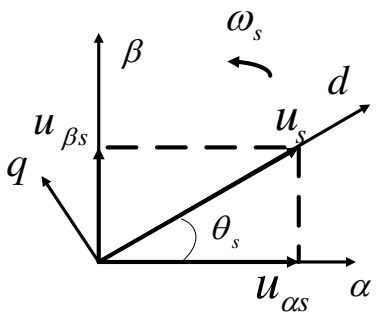

Figure 2.9 dq frame at grid side.

The plot of the vector control through *dq* reference frame in the grid side is shown in Figure 2.9. From this figure, it can be seen that$u_{ds} = u_s, u_{qs} = 0$. The active and reactive power flow between the grid and grid side converter are given as:

$$P_s = \frac{3}{2} u_{ds} i_{ds} \tag{2.26}$$

$$Q_s = -\frac{3}{2} u_{ds} i_{qs} \tag{2.27}$$

It is seen that the active power and reactive power are proportional to i_{ds} and i_{qs} respectively. Here, harmonics due to the switching and losses in resistance and converter are ignored, following equations can be developed.

$$u_{dc} i_{cs} = \frac{3}{2} u_{ds} i_{ds} \tag{2.28}$$

$$u_{ds} = \frac{m}{2} u_{dc} \tag{2.29}$$

$$i_{cs} = \frac{3}{4} m i_{ds} \tag{2.30}$$

$$C\frac{du_{dc}}{dt} = i_{cs} - i_{cr} = \frac{3}{4}mi_{ds} - i_{cr} \tag{2.31}$$

where *m* is the PWM modulation depth of the grid side converter, the value used in this Dissertation is around 0.75 [38].

From (2.28), it is seen that u_{dc}can be controlled via i_{ds}. Therefore, the current control loop is based on i_{ds} and i_{qs}. Reference value of i_{ds}can be derived from the DC link voltage error. Normally i_{qs} is set to zero since it is assumed that there is no reactive power flow between the grid and grid side converter.

The reference values of u_{sd} and u_{sq} can be calculated as follows:

$$u_{ds\_ref} = -u'_{ds} + \omega_s L i_{qs} + u_{ds1} \tag{2.32}$$

$$u_{qs\_ref} = -u'_{qs} - \omega_s L i_{ds} \tag{2.33}$$

The vector control scheme for grid side PWM voltage source converter is shown in Figure 2.10.

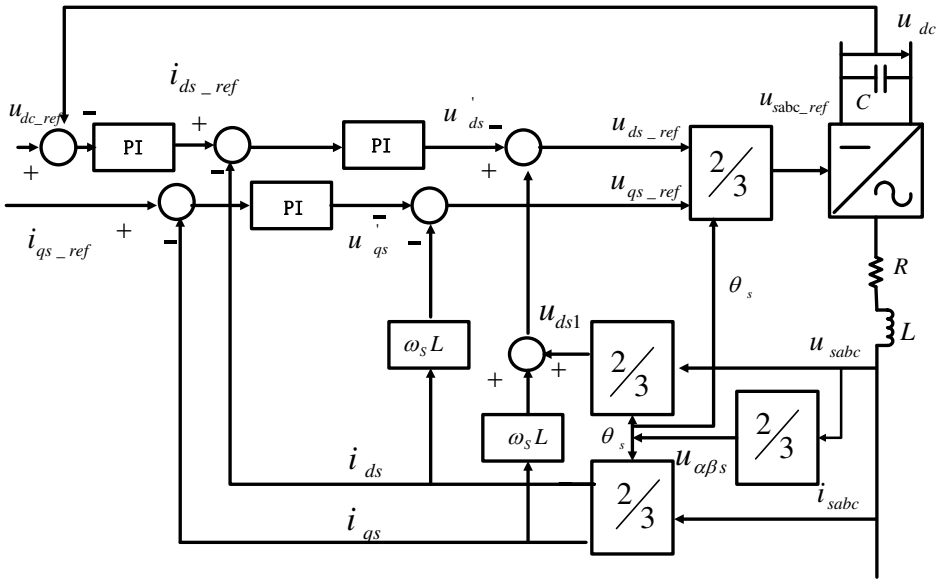

Figure 2.10 Grid side control structure

B. Rotor side control with traditional PI control design

The rotor side converter is controlled in a synchronously rotating *dq* axis frame with the *d* axis aligned with the stator flux vector position. In this way, a decoupled control for stator side active and reactive powers is acquired. The control strategy needs to measure the stator and rotor side currents, stator voltage and the rotor position. The *dq* frame at the rotor side is shown in Figure 2.11.

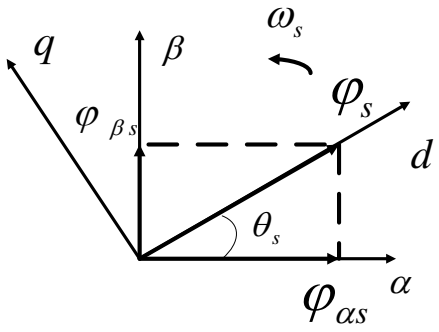

Figure 2.11 dq frame at rotor side.

The stator flux angle position θ_s is calculated as:

$$\theta_s = \int \omega_s \, dt = \tan^{-1} \frac{\varphi_{\beta s}}{\varphi_{\alpha s}} \tag{2.34}$$

$$\varphi_{\alpha s} = \int (u_{\alpha s} - r_s i_{\alpha s}) dt \tag{2.35}$$

$$\varphi_{\beta s} = \int \left(u_{\beta s} - r_s i_{\beta s}\right) dt \tag{2.36}$$

The $d-$ axes aligned with φ_s , so that $\varphi_{ds} = \varphi_s, \varphi_{qs} = 0$ .The stator flux is assumed constant since it is connected to the grid, so that the influence of the stator resistance is small. Thus the DFIG model can be written as:

$$\varphi_{ds} = \varphi_s = L_m i_{ms} = L_s i_{ds} + L_m i_{dr} \tag{2.37}$$

$$\varphi_{dr} = \frac{L_m^2}{L_s} i_{ms} + \sigma L_r i_{dr} \tag{2.38}$$

$$\varphi_{qr} = \sigma L_r i_{qr} \tag{2.39}$$

$$0 = L_s i_{qs} + L_m i_{qr} \; ; \; i_{qs} = -\frac{L_m}{L_s} i_{qr} \tag{2.40}$$

$$u_{dr} = R_r i_{dr} + \sigma L_r \frac{di_{dr}}{dt} - (\omega_s - \omega_r) \sigma L_r i_{qr} \tag{2.41}$$

$$u_{qr} = R_r i_{qr} + \sigma L_r \frac{di_{qr}}{dt} + (\omega_s - \omega_r) \left(\frac{L_m^2}{L_s} i_{ms} + \sigma L_r i_{dr}\right) \tag{2.42}$$

$$T_e = -\frac{3}{2} P \frac{L_m^2}{L_s} i_{ms} i_{qr} \tag{2.43}$$

$$\sigma = 1 - \frac{L_m^2}{L_s L_r} \tag{2.44}$$

$$u_{qs} = 0 \tag{2.45}$$

$$u_s = u_{ds} = \omega_s \varphi_{ds} \tag{2.46}$$

The stator side active power and reactive power can be expressed as follows:

$$P_s = \frac{3}{2}\left(u_{ds} i_{ds} + u_{qs} i_{qs}\right) = -\frac{3}{2}\frac{L_m}{L_s} u_s i_{qr} \tag{2.47}$$

$$Q_s = \frac{3}{2}\left(u_{qs} i_{ds} - u_{ds} i_{qs}\right) = \frac{3}{2} u_s \left(\frac{u_s}{\omega_s L_s} - \frac{L_m}{L_s} i_{dr}\right) \tag{2.48}$$

It is seen that P_s and Q_s can be controlled through i_{qr} and i_{dr} respectively. The rotor control structure includes inner control loop for controlling i_{qr} and i_{dr} and outer control loop for P_s and Q_s. There are two parts in the rotor side control. The inner control loop is used to control the *dq* rotor currents, while the outer control loop is used to control the active and reactive power of the stator side.

$$u'_{dr} = R_r i_{dr} + \sigma L_r \frac{di_{dr}}{dt} \tag{2.49}$$

$$u'_{qr} = R_r i_{qr} + \sigma L_r \frac{di_{qr}}{dt} \tag{2.50}$$

Then

$$u_{dr\_ref} = u'_{dr} - (\omega_s - \omega_r)\sigma L_r i_{qr} \tag{2.51}$$

$$u_{qr\_ref} = u'_{qr} + (\omega_s - \omega_r)\left(\frac{L_o^2}{L_s} i_{ms} + \sigma L_r i_{dr}\right) \tag{2.52}$$

The plant for the current control loop is calculated as below.

$$\frac{i_{dr}(s)}{u'_{dr}(s)} = \frac{i_{qr}(s)}{u'_{qr}(s)} = \frac{1}{\sigma L_r s + R_r} \tag{2.53}$$

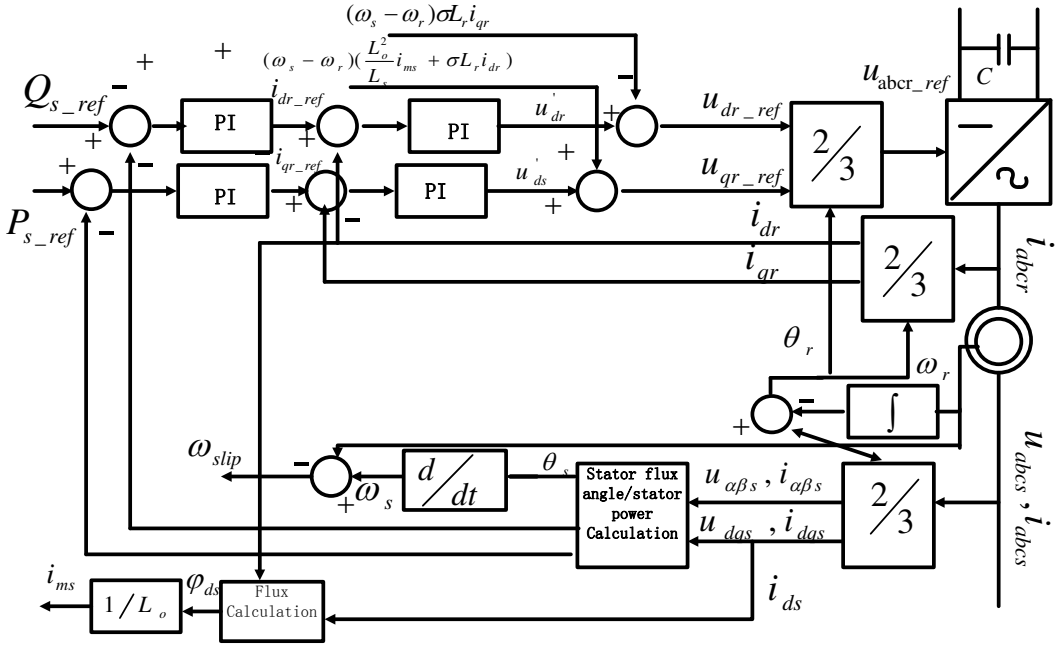

Figure 2.12 Structure of rotor side control.

C. Rotor side control with internal model control (IMC) design

Internal model control (IMC) can be applied in DFIG wind turbine control design for active power and reactive power control for wind power generation [62]. The control structure of IMC is shown in Figure 2.13. In this Dissertation, direct torque control (DTC) and internal model control (IMC) method are applied to DFIG wind turbine control design for active power and reactive power control for wind turbine. The control structure of the DFIG is shown in Figure 2.13, where F(s) is the model of the DFIG in (2.54); $\widehat{F(s)}$ is an internal model of the DFIG; Q_{s_est}, T_{e_est} are estimated values by $\widehat{F(s)}$; , Q_{s_ref}, T_{e_ref} are reference values of stator side reactive power and torque; C(s) is the internal model controller. The reactive power, torque and stator flux are processed by the internal model control (IMC) controller to generate the command rotor voltage and

realize control purpose. In order to get the transfer function of DFIG, all the equations are in Laplace form:

$$\begin{pmatrix} Q_s(s) \\ T_e(s) \end{pmatrix} = F(s) \begin{pmatrix} u_{dr}(s) \\ u_{qr}(s) \end{pmatrix} \tag{2.54}$$

The differences between the measured and estimated values of stator reactive power and torque are computed, and then compared with reference values to launch controller *C(s)*. *C(s)* changes values of rotor voltages in accordance. If $\widehat{F(s)}$ is the exact model of the DFIG, the difference between the measured and estimated values would be zero, then the feedback values are zero and the control system becomes an open loop system. Then *C(s)* can be designed as the inverse of *F(s)*, and outputs of IMC block would follow inputs immediately. While overreacted rotor voltage signals might be generated at *C(s)* during high frequencies, a low pass filter is included in *C(s)* to filter out the noise. DFIG transfer function is developed based on the generator characteristics so as to have a correct model of $\widehat{F(s)}$ and then *C(s)* can be designed.

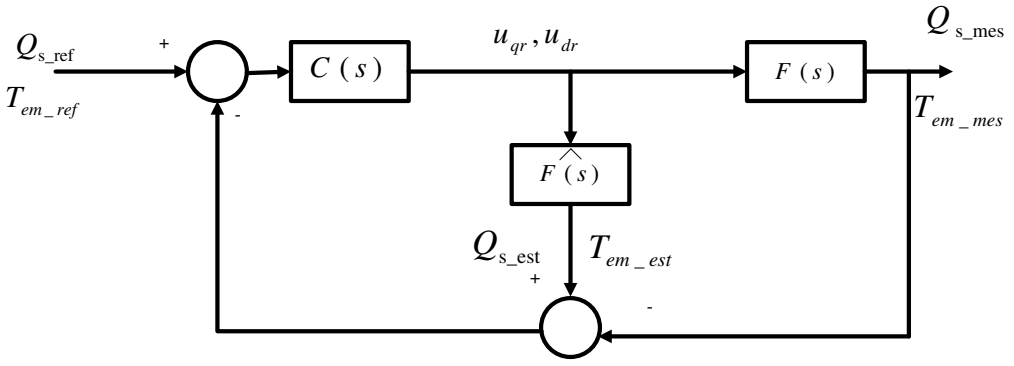

Figure 2.13 Internal model control structure

The stator flux is assumed to be constant and the stator voltage can be approximated with the stator flux with the ignorance of stator resistance, $u_{ds}(s)$ is aligned with the stator flux as follows:

$$\begin{pmatrix} u_{qs}(s) \\ u_{ds}(s) \end{pmatrix} \cong \varphi_s(s) \begin{pmatrix} 0 \\ \omega_s \end{pmatrix} \tag{2.55}$$

According to (2.5) and (2.6), relationships between rotor and stator currents changes can be expressed as follows:

$$\begin{pmatrix} \Delta i_{ds}(s) \\ \Delta i_{qs}(s) \end{pmatrix} = -\frac{L_m}{L_s} \begin{pmatrix} \Delta i_{dr}(s) \\ \Delta i_{qr}(s) \end{pmatrix} \tag{2.56}$$

where Δ represents small changes of variables. From (2.5)-(2.8), rotor flux can be represented by stator flux and currents as:

$$\begin{pmatrix} \varphi_{dr}(s) \\ \varphi_{qr}(s) \end{pmatrix} - \begin{pmatrix} \varphi_s(s) \\ 0 \end{pmatrix} = L_{r1} \begin{pmatrix} \Delta i_{dr}(s) \\ \Delta i_{qr}(s) \end{pmatrix} - L_{s1} \begin{pmatrix} \Delta i_{ds}(s) \\ \Delta i_{qs}(s) \end{pmatrix} \tag{2.57}$$

During a small change in the rotor flux, (2.57) becomes

$$\begin{pmatrix} \Delta\varphi_{dr}(s) \\ \Delta\varphi_{qr}(s) \end{pmatrix} = L_{r1} \begin{pmatrix} \Delta i_{dr}(s) \\ \Delta i_{qr}(s) \end{pmatrix} - L_{s1} \begin{pmatrix} \Delta i_{ds}(s) \\ \Delta i_{qs}(s) \end{pmatrix} \tag{2.58}$$

Taking (2.56) into (2.58), (2.58) becomes

$$\begin{pmatrix} \Delta\varphi_{dr}(s) \\ \Delta\varphi_{qr}(s) \end{pmatrix} = \left(\frac{L_{r1}L_m}{L_{s1}} + L_{r1}\right) \begin{pmatrix} \Delta i_{dr}(s) \\ \Delta i_{qr}(s) \end{pmatrix} = L_k \begin{pmatrix} \Delta i_{dr}(s) \\ \Delta i_{qr}(s) \end{pmatrix} \tag{2.59}$$

Taking (2.59) into (2.11) and (2.12), voltage changes at rotor side can be derived as below.

$$\begin{pmatrix}\Delta u_{dr}(s)\\ \Delta u_{qr}(s)\end{pmatrix}=\begin{pmatrix}R_r+sL_k & -L_k\omega_{slip}\\ L_k\omega_{slip} & R_r+sL_k\end{pmatrix}\begin{pmatrix}\Delta i_{dr}(s)\\ \Delta i_{qr}(s)\end{pmatrix} \tag{2.60}$$

According to the torque expression in (2.13), the rotor current can be developed below

$$i_{qr}(s)=-\frac{2}{3}\frac{L_s}{pL_m\varphi_s(s)}T_{em}(s) \tag{2.61}$$

And with (2.55), the reactive power becomes,

$$Q_s(s)=\omega_s\varphi_s(s)i_{ds}(s)=\omega_s\varphi_s(s)\left(\frac{\varphi_s(s)-L_m i_{dr}(s)}{L_s}\right) \tag{2.62}$$

Then the expression of $i_{dr}(s)$ could be developed as below

$$i_{dr}(s)=\frac{\varphi_s(s)}{L_m}-\frac{L_s}{\omega_s L_m\varphi_s(s)}Q_s(s) \tag{2.63}$$

Small changes in (2.63) yields to:

$$\Delta i_{dr}(s)=-\frac{L_s}{\omega_s L_m\varphi_s(s)}\Delta Q_s(s) \tag{2.64}$$

Due to (2.61) and (2.64), (2.60) becomes

$$\begin{pmatrix}\Delta u_{dr}(s)\\ \Delta u_{qr}(s)\end{pmatrix}=-\frac{L_s}{L_m\varphi_s(s)}\begin{pmatrix}R_r+sL_k & -L_k\omega_{slip}\\ L_k\omega_{slip} & R_r+sL_k\end{pmatrix}\begin{pmatrix}\frac{\Delta Q_s(s)}{\omega_s}\\ \frac{\Delta T_{em}(s)}{p}\end{pmatrix} \tag{2.65}$$

From (2.65), DFIG transfer function can be acquired as below

$$\widehat{F(s)}=-\frac{L_s}{L_m\varphi_s(s)}\begin{pmatrix}R_r+sL_k & -L_k\omega_{slip}\\ L_k\omega_{slip} & R_r+sL_k\end{pmatrix}\begin{pmatrix}\frac{1}{\omega_s}\\ \frac{1}{p}\end{pmatrix} \tag{2.66}$$

2.3.5 Control results with DFIG wind power system

Matlab is a popular software which can be used to simulate DFIG wind power system under different situations (different wind speed, fault situations) and realize DFIG wind turbine control. The control methods are implemented on a 9MW DFIG wind turbine power system, which is connected to the ground after a 3km transmission line. Parameters of the DFIG wind turbine are shown in Table 2.2.

Table 2.2 Parameters of the DFIG wind turbine.

Parameter	***Value***	***Parameter***	***Value***
Rs	0.023 p.u.	L1s	0.18 p.u.
Rr'	0.016 p.u.	L1r'	0.16 p.u.
Lm	2.9 p.u.	Inertia constant H(s)	0.685
pairs of poles (p)	3	Initial conditions of slip	-0.2

Control results with IMC method are as shown below, and the wind speed is 10m/s. From Figure 2.14, it is seen that voltage at grid integration point is stable but with minor harmonic components. From Figure 2.15, dc link voltage is controlled around 1150 V at steady state. The reactive power can be controlled at 0Mvar finally and active power is controlled to converge in the steady state as shown in Figure 2.16 and Figure 2.17.

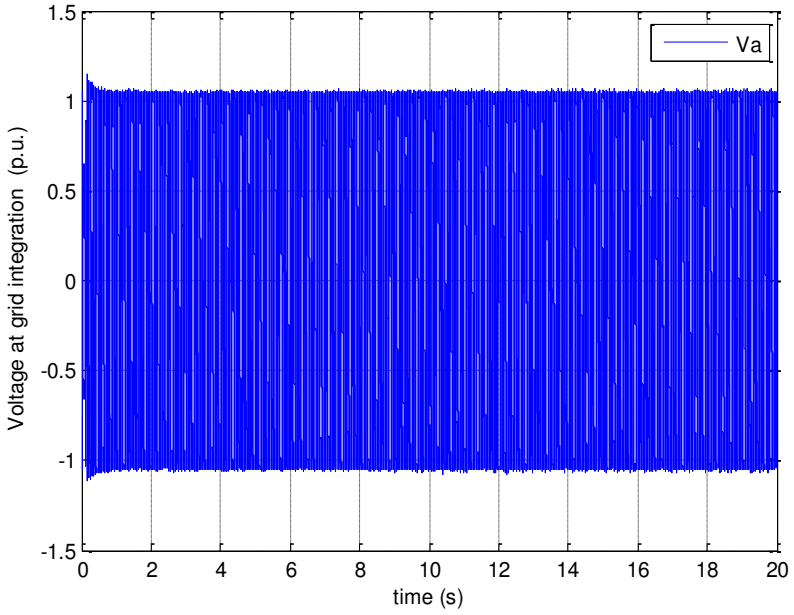

Figure 2.14 Voltage (phase a) at DFIG wind turbine integration point.

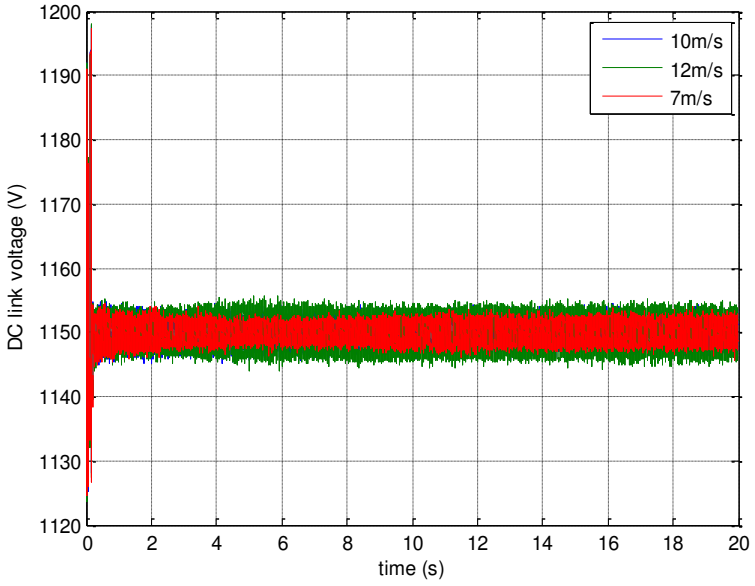

Figure 2.15 DC link voltage.

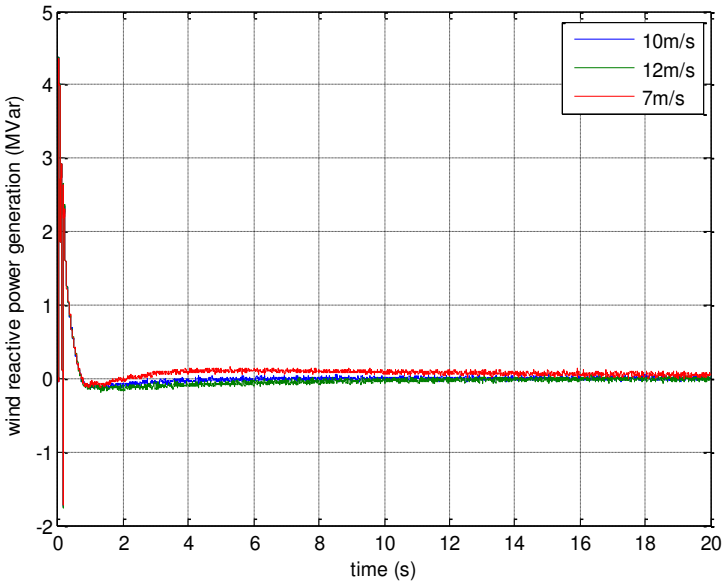

Figure 2.16 Reactive power at the grid integration point.

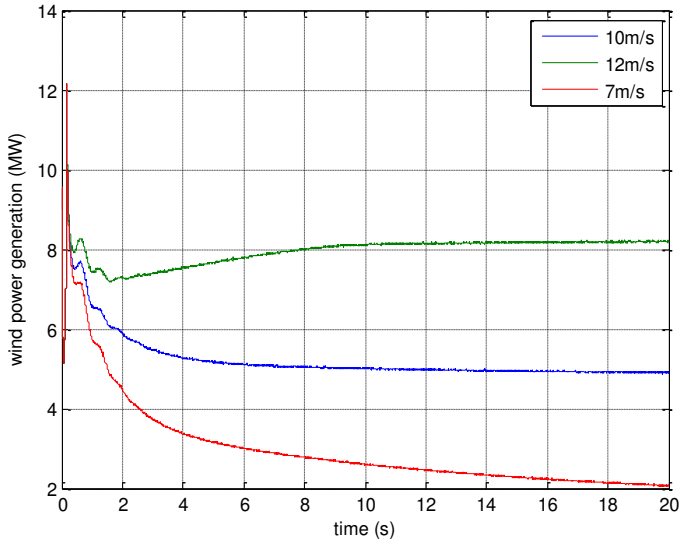

Figure 2.17 Active power at grid integration point.

2.4 Summary

This Chapter introduces the doubly fed induction generator (DFIG) wind turbine, which is a popular variable speed wind turbine and simulated by using dedicated *SimPowerSystems* toolbox in *Matlab/Simulink*. Firstly, the aerodynamic wind power generation theory and the factors that affect wind power generation are shown. Secondly, the structure of DFIG wind power system is explained and modeled, where the rotor circuit is connected to the grid through power electronic devices. Within the DFIG wind power system, an average PWM voltage source converter model is built based on the energy conversion, which allows a longer time step to speed up the computer-aided simulations. Finally, with a comprehensive review on DFIG wind turbine control approaches, internal model control is applied to DFIG wind power systems, and then simulation results are obtained in situations under different wind speeds. This Chapter is essential for wind power system research, which suggests further research in wind power based microgrids.

Chapter Three: Harmonic issues in DFIG wind turbines

In wind power systems it is important to inject high quality power electricity to supply the grid. However, due to operation characteristics of generator, it is inevitable to have harmonic components in current and voltage waveforms in wind energy signals. The problem is those harmonics can found resonances that may amplify them, turning the system unstable and needing to stop the wind power production [96]. In this chapter, reasons for harmonic generation in DFIG wind turbines are revealed and approaches to analyze and avoid the harmonic effects in power systems are derived.

Firstly, the general vector representation of an AC signal is presented. A real value signal *v* (*t*) which contains multiple frequencies is given as follows.

$$v(t) = A_1 \cos(\omega_1 t + \varphi_1) + A_2 \cos(\omega_2 t + \varphi_2) + \cdots + A_n \cos(\omega_n t + \varphi_n) \tag{3.1}$$

where $\omega_1, \cdots, \omega_n$ are not necessarily harmonically related which may include non-integer harmonics. Therefore, *v* (*t*) is considered to be a general representation of voltage, current or flux. Without loss of generality, a voltage signal is assumed in the following discussion. Each sinusoidal term could be expressed as the real part of its complex form. Then *v* (*t*) could be expressed as follows.

$$v(t) = Re\left\{A_1 e^{j\varphi_1} e^{j\omega_1 t} + A_2 e^{j\varphi_2} e^{j\omega_2 t} + \cdots + A_n e^{j\varphi_n} e^{j\omega_n t}\right\} \tag{3.2}$$

$$v(t) = Re\left\{V_1 e^{j\omega_1 t} + V_2 e^{j\omega_2 t} + \cdots + V_n e^{j\omega_n t}\right\} \tag{3.3}$$

where $V_1, V_2, \ldots, V_n$ are voltage vectors which represent the magnitude and phase for each frequency component. $v(t)$ could be arranged via vector algebra as follows:

$$v(t) = Re\{U^T \hat{V} \hat{E}\} \tag{3.4}$$

where $\hat{V}$ is called phasor matrix and $\hat{E}$ is called eigen functions vector. To simplify our notation, the operator Re{} could be omitted and $v(t)$ could be expressed by using complex form. Let $V(t)$ (capital V) be a complex function, such that $v(t) = \mathrm{Re}\{\mathrm{V(t)}\}$.

$$V(t) = U^T \hat{V} \hat{E} \tag{3.5}$$

where

$$U = \begin{bmatrix} 1 \\ 1 \\ : \\ 1 \end{bmatrix}_n \qquad \hat{V} = \begin{bmatrix} V_1 & 0 & 0 & 0 \\ 0 & V_2 & 0 & 0 \\ 0 & 0 & .. & 0 \\ 0 & 0 & 0 & ..V_n \end{bmatrix}$$

$$I = \begin{bmatrix} 1 & 0 & 0 & 0 \\ 0 & 1 & 0 & 0 \\ 0 & 0 & .. & 0 \\ 0 & 0 & 0 & .1 \end{bmatrix}_n \qquad \hat{\mathrm{E}} = \begin{bmatrix} e^{j\omega_1 t} \\ e^{j\omega_2 t} \\ .... \\ e^{j\omega_n t} \end{bmatrix}$$

By differentiating (3.5), the following equation could be acquired:

$$\frac{dV(t)}{dt} = jU^T \hat{V} \hat{\Omega} \hat{E} \tag{3.6}$$

where $\hat{\Omega}$ is the frequency matrix which is given as:

$$\hat{\Omega} = \begin{bmatrix} \omega_1 & 0 & 0 & 0 \\ 0 & \omega_2 & 0 & 0 \\ 0 & 0 & \ldots & 0 \\ 0 & 0 & 0 & \omega_n \end{bmatrix}$$

Equations (3.5) and (3.6) could be easily extended to the three phase form as follows:

$$\begin{aligned} V_a(t) &= U_a^T \hat{V}_a \hat{E}_a \\ V_b(t) &= U_b^T \hat{V}_b \hat{E}_b \\ V_c(t) &= U_c^T \hat{V}_c \hat{E}_c \end{aligned} \tag{3.7}$$

also,

$$\begin{aligned} \frac{dV_a(t)}{dt} &= jU_a^T \hat{V}_a \hat{\Omega}_a \hat{E}_a \\ \frac{dV_b(t)}{dt} &= jU_b^T \hat{V}_b \hat{\Omega}_b \hat{E}_b \\ \frac{dV_c(t)}{dt} &= jU_c^T \hat{V}_c \hat{\Omega}_c \hat{E}_c \end{aligned} \tag{3.8}$$

Further, (3.7) can be developed in the matrix form as follows:

$$\begin{bmatrix} V_a(t) \\ V_b(t) \\ V_c(t) \end{bmatrix} = \begin{bmatrix} U_a^T \\ U_b^T \\ U_c^T \end{bmatrix} \begin{bmatrix} \hat{V}_a & & \\ & \hat{V}_b & \\ & & \hat{V}_c \end{bmatrix} \begin{bmatrix} \hat{E}_a \\ \hat{E}_b \\ \hat{E}_c \end{bmatrix} \tag{3.9}$$

$$V_{abc}(t) = U_{abc}^T \hat{V}_{abc} \hat{E}_{abc} \tag{3.10}$$

Similarly, (4.8) can be expressed in a compact form:

$$\frac{dV_{abc}(t)}{dt} = jU_{abc}^T \hat{V}_{abc} \hat{\Omega}_{abc} \hat{E}_{abc} \tag{3.11}$$

Equations (3.10) and (3.11) are more general as they may also include non-periodic and unbalanced three phase signals. Clearly, using general vector representation is convenient for modeling DFIG wind power system because it could reveal the interrelationship between harmonics of the rotor's current and mechanical speed of wind turbine.

3.1 Harmonics modeling in DFIG using the general vector representation form

In this section, a general vector representation is applied to model DFIG's rotor and stator sides' voltage, current and flux in three-phase form. This work can be easily extended to other cases under different conditions, balanced or unbalanced. Model development is started from a very simple self-inductance in the stator side, and then extended by adding mutual inductance on the stator side and finally magnetization effect

from the rotor to the stator side is included. In this paper, v (t), i(t) and λ(t) are used to indicate real value signals of voltage, current and flux, respectively. We have also used *V (t)*, *I (t)* and *Λ (t)* (in capital case) to indicate complex value signals of voltage, current and flux, respectively.

3.1.1 Modeling with stator side

Firstly, only one phase (phase a) winding in the stator is modeled without presence of any other rotor windings as shown in Figure3.1. The stator voltage of phase *a*, $v_{s,a}(t)$, may include multiple frequency components. Hence, this voltage could be expressed by using the general vector representation similar to (3.5):

$$V_{s,a}(t) = I_{s,a}(t)R_{s,a} + \frac{d\Lambda_{s,a}}{dt} \tag{3.12}$$

By substituting phasor matrices and eigen function vectors into equation (4.12), the following could be derived.

$$U^T\hat{V}_{s,a}\hat{E} = U^T\hat{I}_{s,a}\hat{E}R_{s,a} + jU^T\hat{\Lambda}_{s,a}\widehat{\Omega}\hat{E} \tag{3.13}$$

Moreover, voltage phasor matrix $\widehat{V}_{s,a}$ is a function of current phasor matrix $\hat{I}_{s,a}$, flux phasor matrix $\widehat{\Lambda}_{s,a}$ and frequency matrix $\widehat{\Omega}$ as shown below.

$$\hat{V}_{s,a} = \hat{I}_{s,a}R_{s,a} + j\hat{\Lambda}_{s,a}\widehat{\Omega} \tag{3.14}$$

which could be expressed in more detail by a function of current phasor matrix $\hat{I}_{s,a}$ and self-inductance of the stator's winding $L_{s,a}$. Then (3.14) becomes as follows:

$$\hat{V}_{s,a} = \hat{I}_{s,a}\left[R_{s,a} + jL_{s,a}\widehat{\Omega}\right] \tag{3.15}$$

For all practical purposes, it is assumed that self-inductance of the stator winding phase a, $L_{s,a}$ is constant for all frequencies and saturation of magnetic field is ignored.

Otherwise, self-inductance at each frequency is needed to be evaluated and included in (3.15).

Now considering three phases form of stator windings as shown in Figure3.2, where each winding is separated by 120^{o} and three phase rotor windings are still omitted. In this situation, stator voltage across phase-*a* could be given as below.

$$V_{s\to s,a}(t) = I_{s,a}(t)R_{s,a} + \frac{d\Lambda_{s,a}}{dt} + \frac{d\Lambda_{s,b\to a}}{dt} + \frac{d\Lambda_{s,c\to a}}{dt} \tag{3.16}$$

where $\Lambda_{s,b\to a}$ and $\Lambda_{s,c\to a}$ are mutual flux in stator between phase a and b, phase a and c respectively. Equation (3.17) could be acquired by converting (3.16) into the general form.

$$\begin{aligned} &U^T\hat{V}_{s\to s,a}\hat{E} \\ &= U^T\hat{I}_{s,a}\hat{E}R_{s,a} + jU^T\hat{\Lambda}_{s,a}\widehat{\Omega}\hat{E} + jU^T\hat{\Lambda}_{s,b\to a}\widehat{\Omega} \\ &+ jU^T\hat{\Lambda}_{s,c\to a}\widehat{\Omega}\hat{E} \end{aligned} \tag{3.17}$$

In (3.17), $\widehat{V}_{s\to s,a}$is stator voltage across phase a due to coupling among all stator windings. $\widehat{E}$ and $\widehat{\Omega}$ include all eigen functions and all frequencies, respectively. Hence, some of diagonal elements in the phasor matrices may be zero when frequency components are not identical among three phases. Now, voltage phasor matrix $\widehat{V}_{s\to s,a}$ could be expressed as below.

$$\hat{V}_{s\to s,a} = \hat{I}_{s,a}R_{s,a} + j\hat{\Lambda}_{s,a}\widehat{\Omega} + j\hat{\Lambda}_{s,b\to a}\widehat{\Omega} + j\hat{\Lambda}_{s,c\to a}\widehat{\Omega} \tag{3.18}$$

which could be rearranged in the following compact form.

$$\hat{V}_{s\to s,a} = \hat{I}_{s,a}R_{s,a} + j\left[\hat{\Lambda}_{s,a} + \hat{\Lambda}_{s,b\to a} + \hat{\Lambda}_{s,c\to a}\right]\widehat{\Omega} \tag{3.19}$$

$$\hat{V}_{s\to s,a} = \hat{I}_{s,a}R_{s,a} + j\hat{\Lambda}_{s,aa}\widehat{\Omega} \tag{3.20}$$

where $\hat{\Lambda}_{s,aa} = \hat{\Lambda}_{s,a} + \hat{\Lambda}_{s,b\to a} + \hat{\Lambda}_{s,c\to a}$.

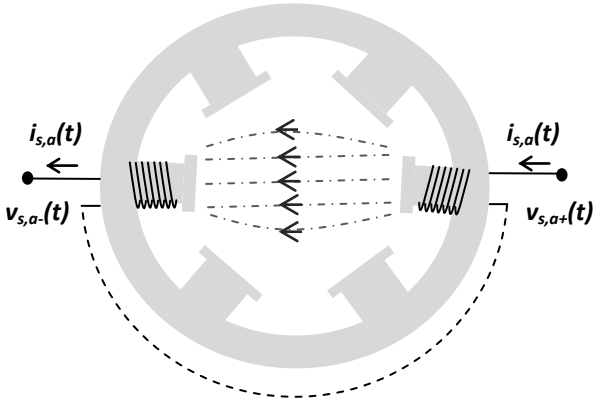

Figure 3.1 The self-magnetic flux in the stator winding of phase a.

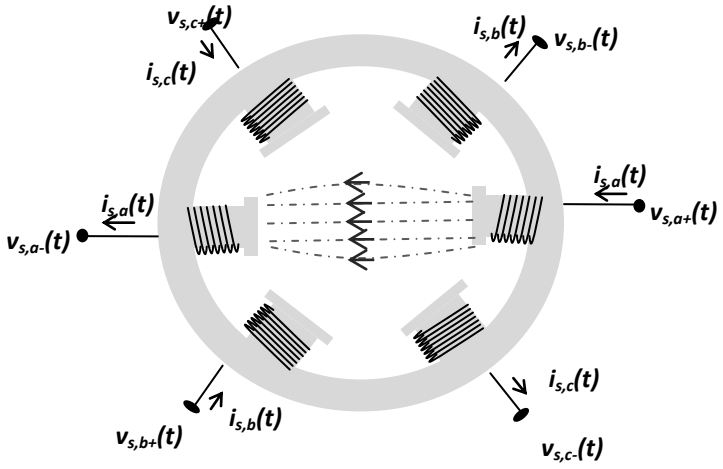

Figure 3.2 The self and mutual magnetic flux of the stator winding of phase a.

Equation (3.20) includes mutual coupling flux as well as self-flux linkage. If windings are balanced, which means mutual coupling flux replaced with their mutual inductances and they are equal. Flux could be replaced with current as shown in (3.21).

$$\hat{V}_{s\to s,a} = \hat{I}_{s,a}R_{s,a} + j[L_s\hat{I}_{s,a} + L_{s,m}(\hat{I}_{s,b} + \hat{I}_{s,c})]\widehat{\Omega} \tag{3.21}$$

3.1.2 Modeling with Rotor Side

After considering the effect of the rotor winding on the stator side, modeling could be started with one phase rotor and one phase stator as shown in Figure 3.3 In DFIG, rotor current carries current with fundamental frequency ω_{r1} in addition to other frequency components, such that the fundamental rotor frequency is related to the slip and synchronous frequency $s\omega_s$. The rotor is also rotating at its mechanical speed ω_m.

The rotor's current creates a magnetic flux $\lambda_{r,a}(t)$ which is linked to the stator winding through the air gap. When two poles are perfectly facing one another, only portion of the magnetic flux is flowing through the air gap from rotor to stator. Let $k\lambda_{r,a}(t)$ indicate the flux from the rotor to the stator, where $0<k<1$. After including the rotor's mechanical speed ω_m, the projected rotor flux $\lambda_{r,a->s,a}(t)$ on the stator is given as below.

$$\lambda_{r,a\rightarrow s,a}(t) = k\lambda_{r,a}(t)\cos(\omega_m t) \tag{3.22}$$

Equation (3.22) assumes that stator pole is perfectly aligned along the horizontal axis at 0^o angle. If ω_{r1} is included in $\lambda_{r,a}(t)$, then according to modulation theorem, $\lambda_{r,a\rightarrow s,a}(t)$ will contain two frequencies, which are $\omega_m+\omega_{r1}$ and $\omega_m-\omega_{r1}$. $\omega_r+\omega_o$ is set to be the synchronous speed at 60Hz. So that, a low non-integer frequency component, $\omega_m-\omega_{r1}$is expected in the stator side.

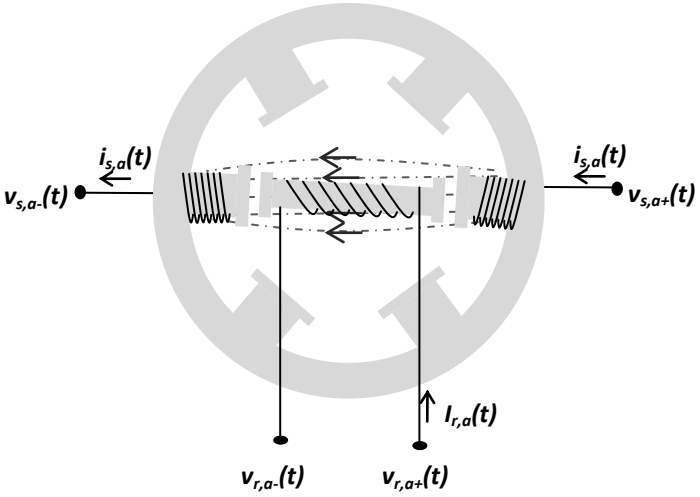

Figure 3.3 The mutual flux from the rotor to the stator windings of phase a.

Equation (3.22) is valid only when the rotor pole is perfectly facing the stator pole. However, the area of interface between the two poles changes as a function of time as the rotor continues rotating. Hence, a rectangular pulse with rising and falling edges is proposed as shown in Figure 3.4, which is called window rectangular pulse. The window rectangular pulse is used to model the area of interface between the two poles as a function of time.

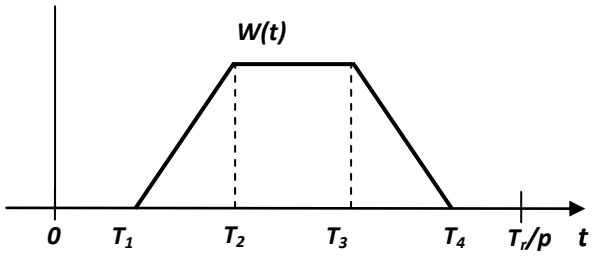

Figure 3.4 Area of interface between the stator and rotor poles.

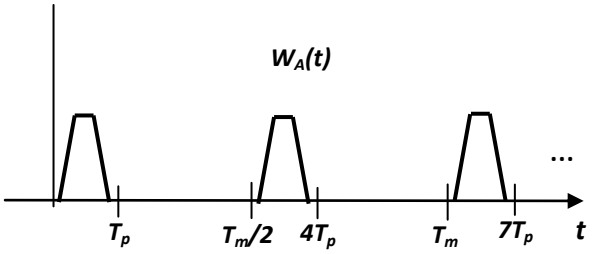

Figure 3.5 Areas of interface for phase a stator poles to phase a rotor pole.

If the rotor is rotating at a constant speed, then two poles are interfaced twice in one complete cycle as the rotor has two poles one at each end. Hence, the window pulse is periodic. $W_A(t)$ is used to model the area of interface between stator's pole and rotor's pole for phase a as shown in Figure 3.5. Note that $W_A(t)$ is periodic over half the rotation time Tm. By including $W_A(t)$, (3.22) becomes as below.

$$\lambda_{r,a\to s,a}(t) = k\lambda_{r,a}(t)\cos(\omega_m t)\, W_A(t) \tag{3.23}$$

In (3.23), replacing $\lambda_{r,a}(t)$ with its matrix equivalent general vector form and $\cos(\omega_r t)$ with its complex conjugate form, the following could be obtained.

$$\Lambda_{r,a\to s,a}(t) = kU^T \hat{\Lambda}_{r,a}\hat{E}\left[\frac{e^{j\omega_m t} + e^{-j\omega_m t}}{2}\right] W_A(t) \tag{3.24}$$

which can be expressed as below.

$$\Lambda_{r,a\to s,a}(t) = \frac{1}{2} kU^T \hat{\Lambda}_{r,a}\left[\hat{X}_+ + \hat{X}_-\right] W_A(t) \tag{3.25}$$

In (3.25),

$$\hat{X}_+ = \begin{bmatrix} e^{j(\omega_{r1}+\omega_m)t} \\ e^{j(\omega_{r2}+\omega_m)t} \\ \vdots \\ e^{j(\omega_{rn}+\omega_m)t} \end{bmatrix} \text{and} \hat{X}_- = \begin{bmatrix} e^{j(\omega_{r1}-\omega_m)t} \\ e^{j(\omega_{r2}-\omega_m)t} \\ \vdots \\ e^{j(\omega_{rn}-\omega_m)t} \end{bmatrix}.$$

where $\omega_{r1}, \ldots, \omega_{rn}$ are frequency components in rotor's flux. Then the current induced by the stator due to the rotor's flux is given as below.

$$I_{r,a\to s,a}(t) = \frac{1}{2} k U^T \hat{I}_{r,a} \left(\frac{N_r}{N_s}\right) \left[\hat{X}_+ + \hat{X}_-\right] W_A(t) \tag{3.26}$$

$$\frac{d\Lambda_{r,a\to s,a}(t)}{dt}$$

$$= \frac{1}{2} k U^T \hat{\Lambda}_{r,a} \left\{ j\left[\hat{\Omega}_{\omega r+} \hat{X}_+ + \hat{\Omega}_{\omega r-} \hat{X}_-\right] W_A(t) + \left[\hat{X}_+ + \hat{X}_-\right] \frac{d}{dt} W_A(t) \right\} \tag{3.27}$$

where $\hat{\Omega}_{\omega r+} = \hat{\Omega} + \hat{\mathrm{I}}\omega_m,\ \hat{\Omega}_{\omega r-} = \hat{\Omega} - \hat{\mathrm{I}}\omega_m$.

Equation (3.27) defines the voltage induced at the stator due to the rotor's flux, and it can be expressed as a function of the mutual inductance and the rotor's current.

$$\frac{d\Lambda_{r,a\to s,a}(t)}{dt} = V_{r,a\to s,a} = \frac{1}{2} L_m U^T \hat{I}_{r,a} \left\{ j\left[\hat{\Omega}_{\omega r+} \hat{X}_+ + \hat{\Omega}_{\omega r-} \hat{X}_-\right] W_A(t) + \left[\hat{X}_+ + \hat{X}_-\right] \frac{d}{dt} W_A(t) \right\} \tag{3.28}$$

Now the effect of three phases' rotor windings could be considered. As shown in Figure 3.6, three phase rotor windings are rotating at ω_m so that that each pole of rotor has its own window signal which defines the overlapping area of interface. Figure 3.7 illustrates window pulses of each phase of the rotor poles into phase *a* of the stator poles. Hence the flux linked from phase *b* and *c* of the rotor to phase *a* of the stator are described as below.

$$\lambda_{r,b\to s,a}(t) = k\lambda_{r,b}(t) \cos\left(\omega_m t + \frac{2\pi}{3}\right) W_B(t) \tag{3.29}$$

$$\lambda_{r,c\to s,a}(t) = k\lambda_{r,c}(t) \cos\left(\omega_m t + \frac{4\pi}{3}\right) W_C(t) \tag{3.30}$$

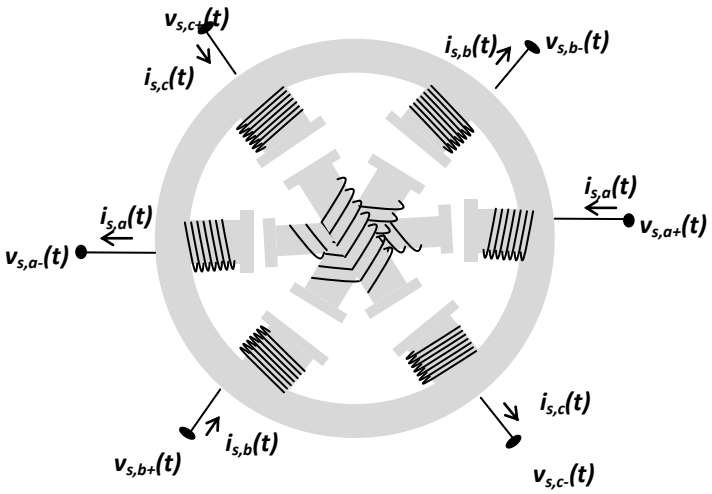

Figure 3.6 The three phase mutual fluxes from the rotor to the stator winding.

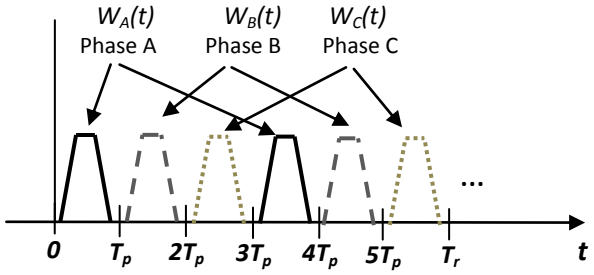

Figure 3.7 The window pulses of the rotor's three phases on stator's phase a.

Using the complex form, (3.29) and (3.30) would become as below.

$$\Lambda_{r,b\to s,a}(t) = kU^T \hat{\Lambda}_{r,b} \hat{E} \left[\frac{e^{j\omega_m t+\frac{2\pi}{3}} + e^{-j\omega_m t-\frac{2\pi}{3}}}{2} \right] W_B(t) \tag{3.31}$$

$$\Lambda_{r,c\to s,a}(t) = kU^T \hat{\Lambda}_{r,c} \hat{E} \left[\frac{e^{j(\omega_m t+\frac{4\pi}{3})} + e^{-(j\omega_m t+\frac{4\pi}{3})}}{2} \right] W_C(t) \tag{3.32}$$

Then current and voltage in phase *a* of the stator due to phase b of the rotor is given as below.

$$I_{r,b\to s,a}(t) = \frac{1}{2} k U^T \hat{I}_{r,b} \left(\frac{N_r}{N_s}\right) \left[\hat{X}_+ + \hat{X}_-\right] W_B(t) \tag{3.33}$$

$$\begin{aligned}\frac{d\Lambda_{r,b\to s,a}(t)}{dt} &= V_{r,b\to s,a}(t) \\ &= \frac{1}{2} L_m U^T \hat{I}_{r,b} \left\{ j\left[\widehat{\Omega}_{\omega r+} \hat{X}_+ + \widehat{\Omega}_{\omega r-} \hat{X}_-\right] W_B(t) \right. \\ &+ \left[\hat{X}_+ \right. \\ &\left. \left. + \hat{X}_-\right] \frac{d}{dt}[W_B(t)] \right\}\end{aligned} \tag{3.34}$$

Similarly, current and voltage in phase *a* of the stator side due to phase *c* of the rotor are shown below.

$$I_{r,c\to s,a}(t) = \frac{1}{2} k U^T \hat{I}_{r,c} \left(\frac{N_r}{N_s}\right) \left[\hat{X}_+ + \hat{X}_-\right] W_C(t) \tag{3.35}$$

$$\begin{aligned}\frac{d\Lambda_{r,C\to s,a}(t)}{dt} &= V_{r,c\to s,a}(t) \\ &= \frac{1}{2} L_m U^T \hat{I}_{r,C} \left\{ j\left[\widehat{\Omega}_{\omega r+} \hat{X}_+ + \widehat{\Omega}_{\omega r-} \hat{X}_-\right] W_C(t) \right. \\ &+ \left[\hat{X}_+ \right. \\ &\left. \left. + \hat{X}_-\right] \frac{d}{dt}[W_C(t)] \right\}\end{aligned} \tag{3.36}$$

Finally, stator current in phase a affected by three phase rotor currents could be developed.

$$\mathrm{I_{s,a}(t) = I_{r,a\to s,a}(t) + I_{r,b\to s,a}(t) + I_{r,c\to s,a}(t)} \tag{3.37}$$

$$\mathrm{I_{s,a}(t) = \frac{1}{2} k \left(\frac{N_r}{N_s}\right) U^T \left[\hat{I}_{r,a} W_A(t) \;\; + \hat{I}_{r,b} W_B(t) + \hat{I}_{r,c} W_C(t)\right]\left[\hat{X}_+ + \hat{X}_-\right]} \tag{3.38}$$

The voltage across phase *a* of the stator can be expressed as following:

$$\begin{aligned}&\widehat{V}_{s\to s,a} \\ &= \hat{I}_{s,a}\, R_{s,a} + j\left[L_s \hat{I}_{s,a} + L_{s,m}\left(\hat{I}_{s,b} + \hat{I}_{s,c}\right)\right]\widehat{\Omega} \;\; + V_{r,a\to s,a}(t) + V_{r,b\to s,a}(t) \\ &+ V_{r,c\to s,a}(t)\end{aligned} \tag{3.39}$$

Equation (3.37) describes the current injected into the stator. It is clear that the stator current contains harmonics due to DC/AC switching in the rotor current. Those harmonics are modulated with mechanical speed to generate higher frequency coefficients that are injected into stator. Also, the window pulses in 6-pole machine would create multiples of the sixth fundamental frequency which would be modulated with the fundamental synchronous frequency. Thus$(n6\omega_s \mp \omega_s)$ harmonics are expected at the stator side. In addition, a low non-integer harmonics ($\omega_m - \omega_{r1}$) is expected due to the difference between the rotor's mechanical frequency (ω_m) and the fundamental rotor frequency (ω_{r1}).

3.2 Harmonic resonance mode analysis in DFIG wind power system

Harmonic resonance frequency point will cause harmonic resonance phenomenon, which makes the inductance and capacitance cancelled each other in the equivalent circuit of the system [63]. Since a wind power system comprises a lot inductive elements and capacitive elements coming from large capacities of wind turbines, reactive compensation equipment and transmission lines, the need of resonance analysis is essential[64]. Such resonant frequencies can be a concern when they are close to any of the harmonic frequencies existing in the power system， which would increase the total harmonic distortion in the current and voltage depending on the resonance impedance seen at that location. The evaluation of such problem is complex as harmonic study needs to be carried out for all buses in the system [65]. References [66] and [67] show that variable speed wind turbines by themselves are not a significant source of harmonic injection in the system however they may cause a problem due to harmonic resonances in the system. When interconnecting wind power generator in the grid, shunt capacitor bank

is installed at main substation or an underground cable is used to connect wind farm to the grid, harmonic distortion becomes a significant issue.

A resonance frequency point would cause voltage distortion amplification due to parallel resonance or high harmonic current due to series resonance. Parallel resonance frequency shows high network equivalent impedance, which is commonly used and means that small harmonic currents can generate high harmonic voltage in the grid. Series resonance frequency shows low network equivalent impedance, which means that small harmonic voltages can generate high harmonic current in the grid.

When the value of inductive elements is equal to that of parallel capacitive elements, parallel resonance occurs. The parallel resonant frequency is calculated as follows:

$$f_r = \frac{1}{2\pi}\sqrt{\frac{1}{L_{eq}C}} \tag{3.40}$$

At this frequency, the apparent impedance seen from the harmonic current becomes high [68]. Series resonances occurs when low impedance is seen at the resonant frequency, which causes high current and high voltage distortion even at a location with no or little harmonic emission [68]. Since the transformer inductance and capacitor bank is small enough to be ignored, the series impedance of transformer is only limited by its resistance. Same as the situation of capacitor bank, the series impedance of capacitor bank is only limited by its resistance. When series resonance happens, harmonic currents will flow freely in this circuit with amplified magnitude and may cause equipment overheating and tripping.

It is usually assumed that harmonic sources are concentrated to a few buses with harmonic producing loads for conducting harmonic study. Harmonic resonance modal analysis (HRMA) is a kind of frequency scan method and could be described as follows:

$$[\mathrm{I_f}] = [\mathrm{Y_f}] \cdot [\mathrm{V_f}] \tag{3.41}$$

where I_f is the nodal current injection vector in the frequency scan in p.u; V_f is the nodal voltage vector; Y_f is the nodal admittance matrix, which could be inversed to get the nodal harmonic impedance; note that Y_f is different at every specific frequency. When Y_f approaches singularity at certain frequency, harmonic resonance happens and that frequency should be avoided. According to (3.41), the plot of frequency vs. impedance of a power system equivalent circuit could be got and the peak in the plot reveals the potential harmonic resonance frequency point.

In order to get more deep understanding of the network admittance matrix, Y_f is decomposed as follows:

$$\mathrm{Y_f} = \mathrm{L}\Lambda\mathrm{T} \tag{3.42}$$

where $\Lambda = \mathrm{diag}(\lambda_1, \dots, \lambda_n)$ is the diagonal eigenvalue matrix. L and T are left and right eigenvalue matrices. When one of the eigenvalues approaches zero, which also means Y_f approaches singularity, the resonance happens. This eigenvalue is called *critical eigenvalue* and the inverse of the critical eigenvalue's magnitude is named *critical modal impedance*, which indicates the severity of the resonance.

Some further information about the system L and T could be utilized to investigate the impact of the network components on a resonance mode, which could be used to investigate the impact of the network components on a resonance mode. The

sensitivity results are ranked to quantify the impact of each component. The modal impedance sensitivity index and the modal frequency sensitivity index are derived in following the analysis.

$$L = [l_1, \dots, l_n], T = [t_1, \dots, t_n]^T \tag{3.43}$$

$$l_k = [l_{1k}, \dots, l_{nk}]^T, t_k = [t_{k1}, \dots, t_{kn}] \tag{3.44}$$

In (3.43) and (3.44), the critical right and left eigenvectors represent the excitability and observability of each bus to the resonance mode. The work [69] introduces the sensitivity matrix, in which the diagonal values of the sensitivity matrix are called *participation factors*, which shows how much each bus participates in a certain modal resonance. The bus with the largest participation factor is called the frequency center, which can be expressed as:

$$F = l_k * t_k = \begin{pmatrix} l_{1k} \\ \cdots \\ l_{jk} \\ \vdots \\ l_{nk} \end{pmatrix} \begin{pmatrix} t_{k1} & \dots t_{kj} \dots \dots \dots t_{nk} \end{pmatrix} \tag{3.45}$$

For example, HRMA is applied in a wind power system as shown in Figure 3.8 and parameters for this system are shown in Table 3.1. A 9MV wind turbine model with numbered buses is researched in this paper, which includes a harmonic filter, transformers (*Y* type, *Lt*, *Lb*), transmission line, phase reactor (*L*) and a tuned filter (*C1*).

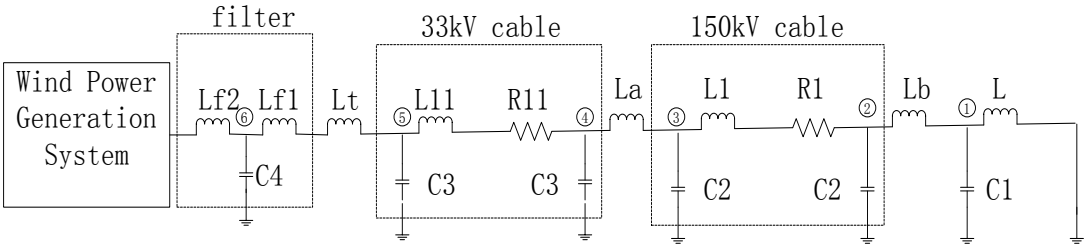

Figure 3.8 DFIG equivalent circuit for HRMA.

All the values used in the table are transferred in the grid level and all the harmonic current injection satisfies IEEE Std 519 rules. Resources of harmonic emission depend on the wind turbine type. In case of the DFIG, it is a variable speed type wind turbine, so that the power electronics converters' operation, rotation process in wind power generator would form harmonic emissions that may distort the voltage and currents of the wind power system. The harmonic resonance mode analysis below the 45thharmonic order results are shown in Figure 3.9 and Figure 3.10.

Table 3.1Wind power system parameters.

Component	Values
150 kV cables	
L1	1.0mH
R1	0.056Ω
C2	0.52μF
Three winding transformers	
La	38.676mH
Lt	51.568mH
33kV cables	
L11	0.018181H
R11	0.37188Ω
C3	1.7126e-4F
LCL filter	
Lf2	1.2H
Lf1	0.641H
C4	5.964 μF
In the grid connection side	
Lb	19.338mH
L	19.3mH
C1	5.658 μF

In Figure 3.9 and Figure 3.10, peaks of the mode shape show sensitive buses and fragile points in this wind power system. Table 3.2 and Table 3.3 reveal the most participation bus for each harmonic resonance frequency point, which is denoted by the most participation factor. Bus 5 and bus 6 are most sensitive and have great impacts in harmonic resonance phenomena, which are heavily involved in a resonance condition. At the frequency order of 13, the wind power system represents has the highest equivalent impedance.

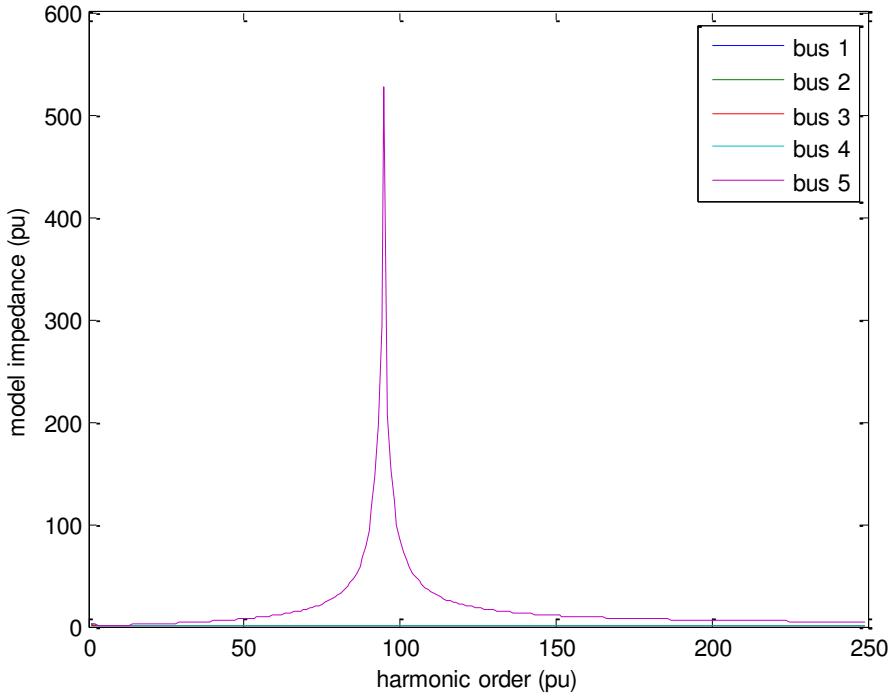

Figure 3.9 Bus1-5.

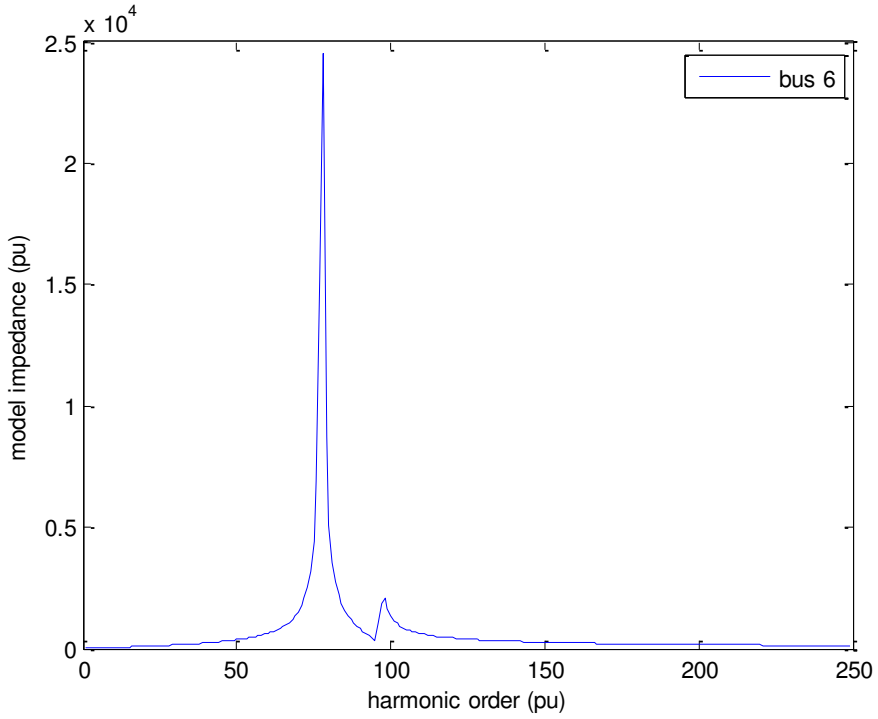

Figure 3.10 Bus 6.

Table 3.2 Harmonic resonance point.

Mode No.	***Modal Resonance Freq. Order (p.u.)***	***Frequency (Hz)***	***Largest Value of Zm (p.u.)***
1	15.83	949.8	527.4293
2	13	780	24526.190
3	16.17	970.2	1875.191

Table 3.3 Participation bus for harmonic resonance point.

	Bus 1	***Bus2***	***Bus3***	***Bus4***	***Bus5***	***Bus6***
Mode 1	0	0	0	0	0.9998	0.002
Mode 2	0	0	0	0	0.001	0.9999
Mode 3	0	0	0	0	0.002	0.9998

A passive filter is designed to compensate the 13^{th} and 15^{th} harmonic. A classic passive harmonic filter as shown in Figure 3.11 is placed in wind power system of Figure

3.8 at bus 6.In filter shown in Figure 3.11, R is installed in parallel with C, so the filter looks like a LRL filter in the low frequency range which will cause some loss. In the high frequency range, the passive filter equals to a LCL filter, which details can be found in Table 3.4. The harmonic currents are injected at the end of the branch using the harmonic current source in accordance to IEEE 519 standards. The measured harmonic currents with respect to the injected harmonics current are shown in Figure 3.12.

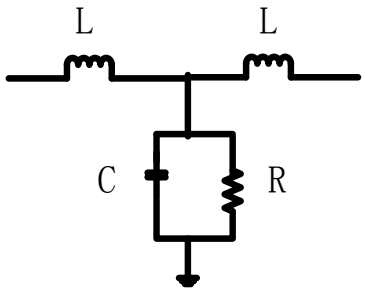

Figure 3.11 Harmonic filter.

Table 3.4 Harmonic filter parameters.

Components	***Values***
L	551.68μH
C	0.52μF
R	0.056Ω

From the HRMA results shown in Figure 3.12, it is seen that the passive filter can damp harmonic resonance points at the designed frequency (13^{th} and 15^{th}harmonic frequency) but it introduces another peak due to its interaction with the wind power system impedance. The potential harmonic resonance points could not be totally cleared in the wind power system, but they could be shifted to above 100^{th} harmonic order which is a higher value. Finally, passive filter could be applied to which could not totally clear

potential harmonic resonance points but it shifts the harmonic resonance points above 100^{th} harmonic order into a more safe zone.

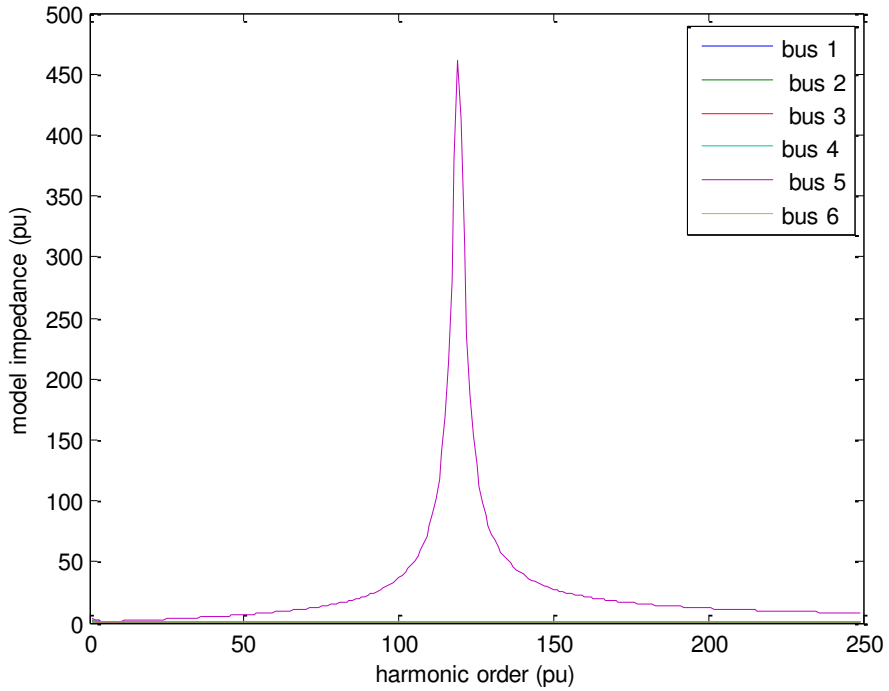

Figure 3.12 HRMA results with passive filter.

3.3 Summary

In this chapter, harmonic issues in DFIG wind power system are analyzed from two viewpoints. Firstly, reasons of harmonic generation due to the machine operation characteristic are revealed and a general vector representation is developed to model DFIG from the harmonic viewpoint. Secondly, the potential risk of harmonic emissions to the grid is analyzed by the harmonic resonance mode analysis (HRMA) approach. HRMA could indicate harmonic resonance frequency points in the wind power system, which is exist in the wind power system grid integration point. Results of wind power harmonic resonance frequency points reveal potential dangerous in wind power system,

which provides useful information in wind power system design and operation. Since components in wind power system are changing all the time in order to adjust different needs in the grids and avoid risks in operation at the same time, it is important to know how to mitigate harmonic signature of these devices, which is proved in this part by applying passive filters. Those resonance points could be easily excited by just harmonic emission from PWM switching process. The analysis results also show that most parts in wind power system are safe in operation except some critical points. Research on harmonic resonance frequency is meaningful in how to design a safe network based on the HRMA results.

Chapter Four: Wind power prediction by using neural networks

In a wind power plant (WPP), data of wind information, such as wind speed, wind direction, wind power generation, humidity and air pressure are collected by a plant information system as wind profile data, and the output of the entire WPP is monitored by the utility's supervisory control and data acquisition (SCADA) system. The raw wind profile data contains some invalid data which is not useful for wind power prediction and has a minor effect on the power grid and need to be filtered out. In this Dissertation, the raw wind profile data set will be screened by probabilistic neural network to prepare high quality data for building neural network models. A neural network model would be applied for predicting wind power with following characteristics. Firstly, model inputs are expressed as complex-valued data (vector representation) which combine wind speed and wind direction. Secondly, the complex-valued recurrent neural network model's time series inputs are generated based on the historical data values of the WPP in northeastern Colorado [75].

4.1 Data preparation

Data preparation process is a very important step in mathematical modeling, since the quality of raw data acquired by plant information system contains errors. For raw wind profile data, there are two kinds of wind turbines in this WPP. The layout of wind turbines and two meteorological towers (MET1&2) is shown in Figure 4.1. In Group 1 there are 53 turbines, rated power at 1.5 MW each one. In Group 2 there are 221 turbines rated at 1MW. The rated power of the whole WPP is 300.5 MW.

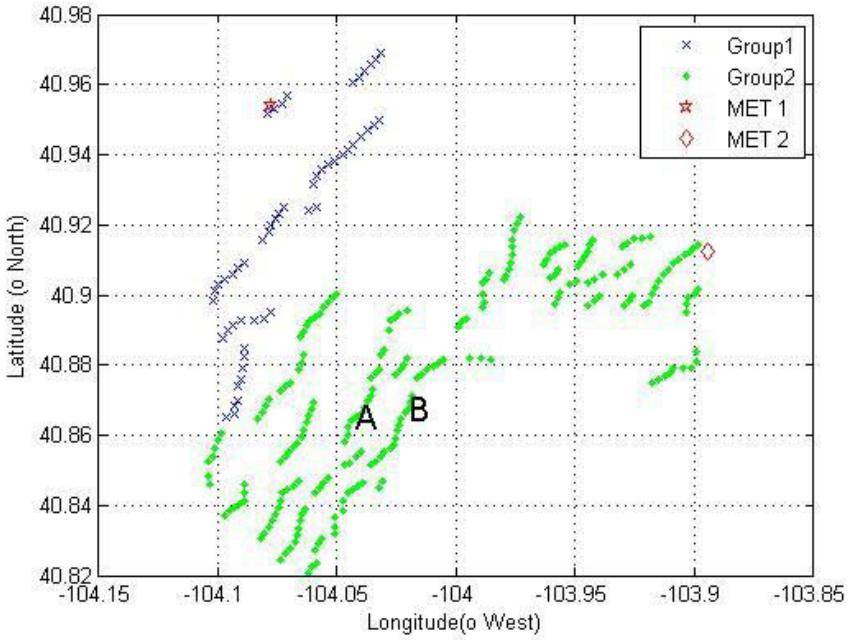

Figure 4.1 Wind power plant distribution.

The data of wind speed (m/s), wind direction (in degrees: 0^{o}~360^{o}), total metered plant-output power (MW), temperature (^{o}C) and air pressure is monitored by the sensors installed at the two meteorological (MET) towers. From individual wind turbines, data of wind speed, wind direction and power output is also collected. The data of the total metered WPP output power is recorded at the point of interconnection, which is very useful to a utility company as a reference to compute power revenue. Following the IEC standard 61400, all the data acquired, except the turbine status, is averaged over a 10-minute period by turbine power curve measurement [75]. Figure 4.2 shows a raw scatter plot of WPP output and wind speed data from MET 1.

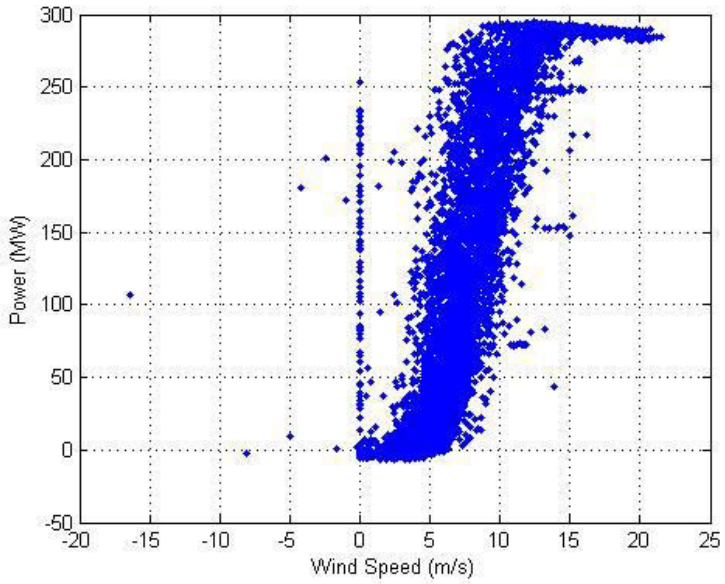

Figure 4.2 Scatter plot wind speed vs. wind power from single wind turbine.

The raw data set (consisting of 8486 dots) contains some invalid data which is not useful for power prediction and has a minor effect on the power grid. The raw data can be classified into five types, as shown in Table 4.1.

Table 4.1 Raw data classification.

Type	***Description***
1	data points following the main power stream
2	data points in low wind speed period with high power generation
3	data points with negative value wind speed
4	data points with negative value power generation
5	data points with low power generation at high wind speed period

The existence of type 2 data might be due to some physical problems, disabled sensors or data distortion in communication channels. Type 3 data does not exist in reality and may be caused by anemometer that needs to be calibrated. Type 4 data is due

to the fact that sometimes the wind turbine cannot generate enough power to offset the electrical consumption of the turbine itself and was drawing, i.e. consuming, power from the grid. The existence of type 5 data might be due to the fact that not all turbines are always online during high wind speed period, especially near cut-off wind speed, and some wind turbines maybe disabled during that period. Another reason can be derived from [10], in case that a strong wind from wrong direction can make a turbine work at low efficiency. In sum, all types of data except type 1 data should be filtered out.

In data selection process, probabilistic neural network (PNN) is a feed-forward neural network with supervised learning using Bayes decision rule and Parzen window [97]. PNN can be used for data classification. The structure of PNN is usually a two-layer model, as shown in Figure 4.3. In the pattern units, the distance between the input vector and the target vector will be calculated. A new vector will be generated to indicate how close the input is to the target vector. The summation units add these distances for each type of inputs to produce a vector of probabilities as output of the network. The output unit generates a 1 for the target class and a 0 for the other classes with the use of a competing transfer function, which picks the maximum the vector of probabilities [98].

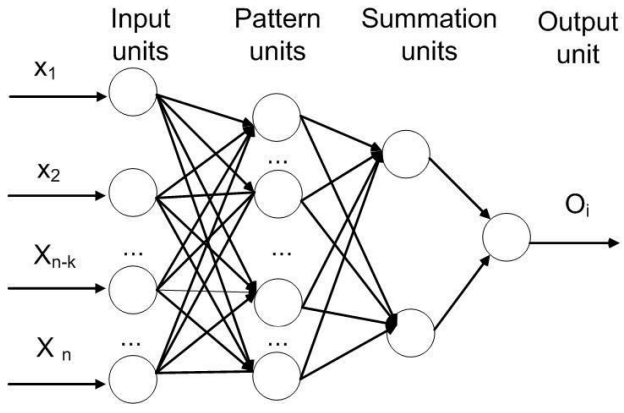

Figure 4.3 Structure of PNN.

In this chapter, PNN was applied to filter out invalid data in the raw data set. For example, data points in Figure 4.2 were classified into five types and the portion for each type of data is different based on statistical analysis. The order of proportion from the largest to the smallest is as follows: type 1, type 4, type 5, type 2, and type 3. In the process of building the PNN model, about 20% of the data points in Figure 4.2, which contains 1700 data points, were selected as training data set. The PNN model was trained by using the sampled data.

Since only type 1 data is the useful information and should be kept, there are two strategies in training the PNN model. We will call them method 1 and method 2, which are described in the following paragraphs.

1) Method 1 is simpler, for which the classification results of PNN are assumed to have only two types. PNN is trained based on two groups: the first group is type 1; the second group includes type 2-5. 1700 data points are selected, among which 1540 were randomly selected from type 1 data points, the rest 160 data points were from type 2-5. In the training data set, the input data vector includes data of wind speed and wind power generation, and the target vector has only two elements, which are 1 (group 1) and 2 (group 2). And then, the rest data points (about 80%) were used as testing data set as input to be classified by the PNN model already built. The number of neurons in the input layer is equal to that of the output layer, which is 2. The training results are shown in Figure 4.4 and Figure 4.5. As shown in Figure 4.5, the classification result using method 1 is not ideal; PNN model could not succeed in diagnosing all the unwanted data. And the classification accuracy is 92.7%, which means the number of the correctly classified data points versus the number of type 1 data as shown in Figure 4.2.

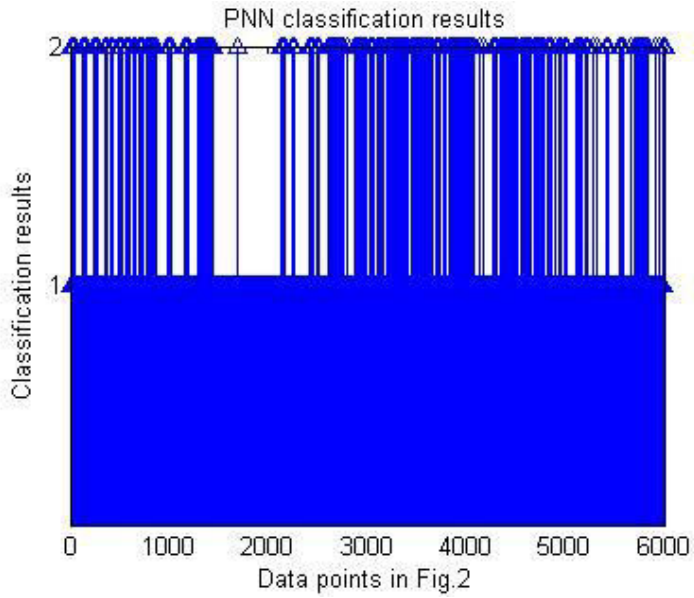

Figure 4.4 Classification results of data in Fig. 4.2 by method 1.

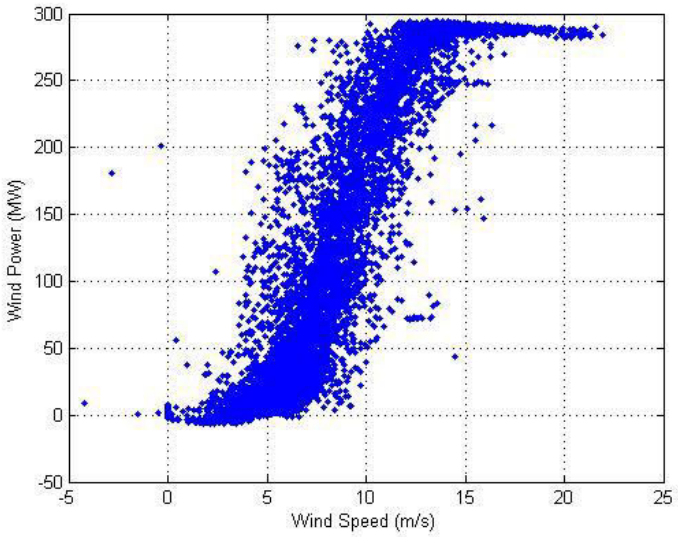

Figure 4.5 Filtered scatter plot of Group 1 data points classified by method 1 (2010 Jan-Mar).

2) In **Method 2**, there are five classification results of PNN, which are type 1, type 2, type 3, type 4, and type 5. PNN is trained based on five types of data points as shown in

Table 4.2. In the 1700 selected data points, 1540 data points were sampled from type 1 data. For the rest 160 data points, according to the portion of each data type, number of data points sampled from type 2, 3, 4, 5 were 20, 10, 70 and 60 respectively. The number of neurons in the input layer is 2 and the number of neurons in the output layer is 5. And results done by testing the rest of the data set can be seen in Figure 4.6 and Figure 4.7.

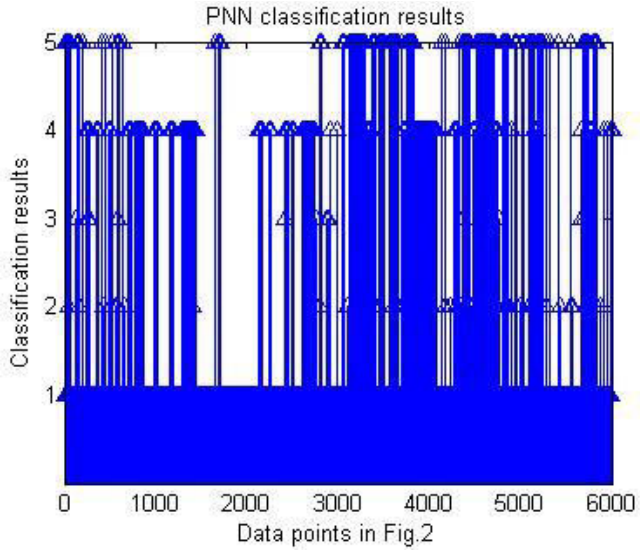

Figure 4.6 Classification results of data in Fig. 4.2 by method 2.

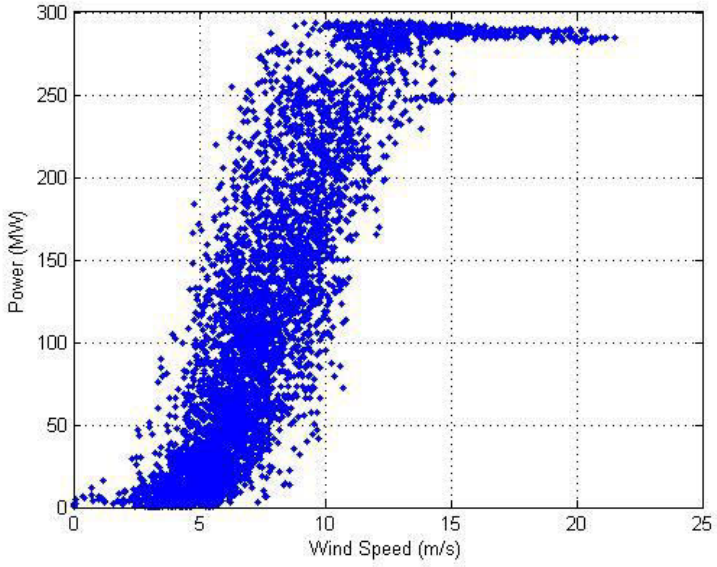

Figure 4.7 Filtered scatter plot of Group 1 data points classified by method 2 (2010 Jan-Mar).

In Figure 4.6, type 1 data can be separated from the testing data set as shown in the classification result and were plotted in Figure 4.7. The PNN model built by using the method 2 could succeed in screening the raw data even though the power curve is not totally smooth. The classification accuracy is 96.5%, which is higher than that of method 1. The classification result using method 2 has a better accuracy than the one performed using method 1, because simply combining type 2-5 data points into a group will disturb the process of building PNN and may create confusion in dividing the line between type 1 data and type 2-5 data.

Wrong classification data points will decrease the accuracy of the prediction model. In the data preparation process of the WPP power prediction model, we adopted method 2 to train PNN model and the problem of wrong classification can be solved by improving the PNN's training data set. For example, after the PNN is built, data points with wrong classification results from testing data set can be added into the training data

set. Then, PNN model should be trained again with the expanded training data set in order to have more accurate classification ability.

The following content is related to data for building models. In this chapter, the power prediction results of the WPP are based on wind speed and wind direction. At first, wind speed factor is a key point in determining the available power generated from a single wind turbine within a certain cross sectional area [71]. The wind speed experienced by individual wind turbines is acquired by the anemometer and comes from the direction of horizontal axes of turbine's hub. The hub is behind the blades, which has an effect of decreasing the natural wind speed. The wind speed acquired from the MET towers represents the natural wind speed at the location on the tower. Even though the height of the hub and MET tower are the same, they have different physical meanings. When we predicted wind power generation, wind speed from turbine should be adopted as input information of the model.

Secondly, wind direction, i.e. direction from which the wind blows, is another kind of useful information to predict wind power based on previous research results [72]. Wind can come from every direction when the wind speed is low. The higher the wind speed, the more uniform and more focused the wind direction. So that during the same wind speed period, wind turbines can have different efficiencies due to different wind directions. However it is not convenient to predict the total power generation of the whole WPP by processing data information from all the turbines. It is better to find individual wind turbines from which the wind speed and wind direction can be most representative of the WPP area's wind situation. The wind speed situation after the data selection process) of the whole year of 2010 is shown in Table 4.2. The data from 2010

Apr-Jun covers a wide range and has the largest mean value of wind speed, which is suitable for training neural network model and is investigated in this Dissertation.

Table 4.2 2010 Wind speed data analysis.

Wind speed (m/s)	***Avg.***	***Std.***	***Maximum***
2010 Jan-Mar	6.945	3.919	21.362
2010 Apr-Jun	8.812	3.927	22.635
2010 Jun-Sep	6.371	3.212	19.552
2010 Oct-Dec	7.330	4.117	21.912

Wind directions of the two groups of wind turbines at 3/18/2010 10:00 PM and 4/10/2010 8:40 AM are shown in Figure 4.8 and Figure 4.9 respectively. The arrows indicate the direction of the wind. The wind directions of Group 2 turbines are focused on a certain direction. The reason of the disordered directions of Group 1 turbine is likely to have its origin in the data distortion due to the data transmission channel or bad performance sensors. The total output of the WPP can be predicted according to only one or two turbine's information [74]. Based on the filtered data set, the average wind speed of all the wind turbines can be acquired. By using correlation, the wind turbine that has the highest correlation value with the average wind speed can be determined. In Figure 4.1, turbine A was selected, which is the one that has the most representative wind speed.

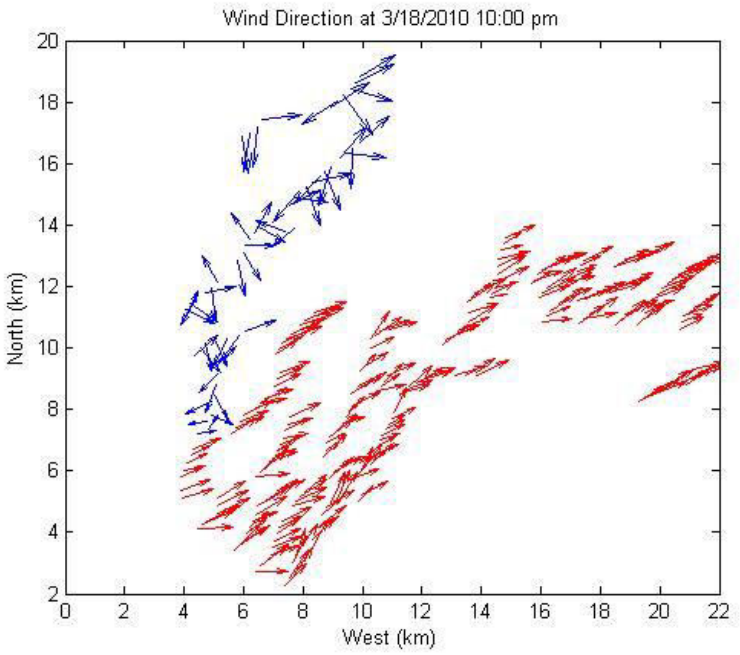

Figure 4.8 Wind direction at 3/18/2010 10:00 PM.

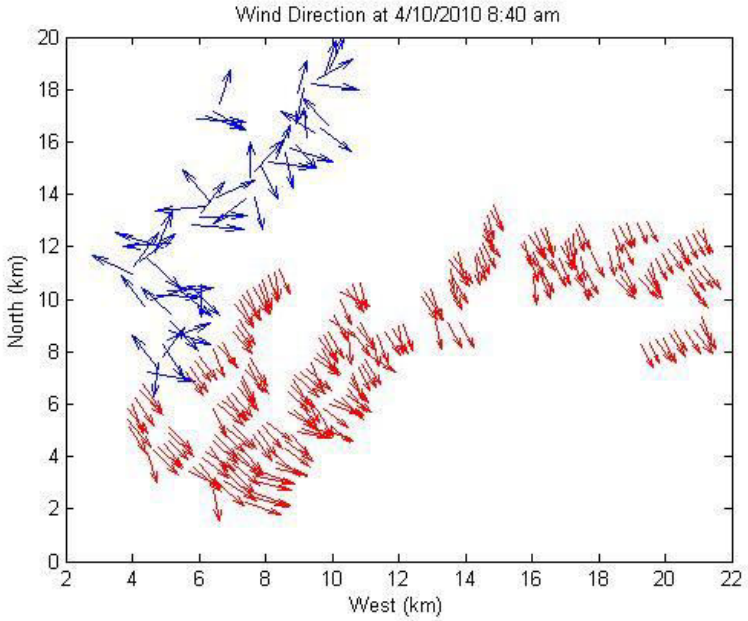

Figure 4.9 Wind direction at 4/10/2010 8:40 AM.

Following the same method, the turbine which has the most representative wind direction can also be found, which was turbine B in Figure 4.1. In this chapter, data

acquired from turbine A and B will be used to predict the total output of the WPP. The wind profile data is obtained during year 2010 and 2011, and the data from 2010 Apr-Jun is selected for building a wind power prediction model in this part.

4.2 Neural network models for wind power prediction

Data of wind speed and direction from turbine A and turbine B can be combined and expressed as a vector on a two-dimensional complex coordinates, as shown in Figure 4.10. The wind vector can be expressed as equation (4.1). In [73], it is demonstrated that the prediction effect by using complex-valued neural network outperforms more than using real-valued neural network.

$$\vec{v} = v\cos\theta + i\, v\sin\theta \tag{4.1}$$

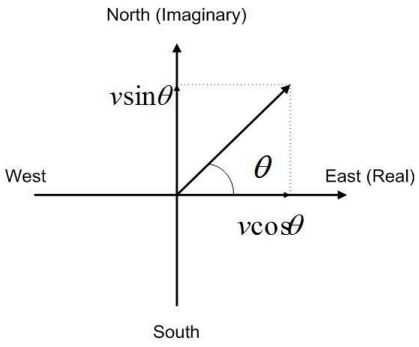

Figure 4.10 Wind vector.

Inputs of recurrent neural network can be either a series of historical measured data or simulated data generated by the model as shown in Figure 4.11. The advantage of this kind of model is that the output signal does not just rely on the current input signals of the system, but it also has an internal memory in its training process. The disadvantage is that the training time of the recurrent neural network is longer than that of the static neural network. In this part, a complex-valued recurrent neural network (CRNN) is

applied to predict a single wind turbine's power generation. The CRNN can be trained under two kinds of modes: parallel (P) mode and series-parallel (SP) mode, as seen in Figure 4.11. In the P mode, the simulated outputs $\tilde{\mathrm{p}}(\mathrm{n}-2), \tilde{\mathrm{p}}(\mathrm{n}-1), \tilde{\mathrm{p}}(\mathrm{n})$ are fed back as input signals. In the SP mode, actual outputs in the previous time step $\mathrm{p}(\mathrm{n}-2), \mathrm{p}(\mathrm{n}-1), \mathrm{p}(\mathrm{n})$ are fed back as input signals, which are applied in this Dissertation. Paper [74] demonstrates that prediction model with P mode inputs will result in accumulation of error if the previous prediction results are not accurate. Therefore, SP mode neural network is adopted to build prediction model in this Dissertation.

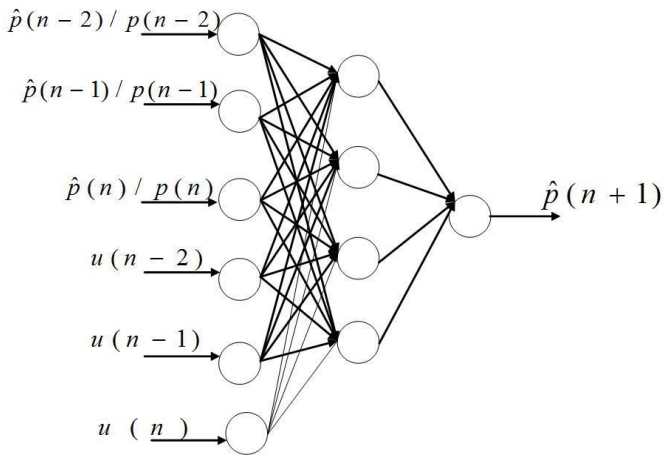

Figure 4.1 Recurrent neural network training structure.

In Figure 4.11, p indicates the power readings from wind turbine,u includes the wind speed vectors from wind turbine, and, n indicates the time step of 10 minutes period. Usually a two-layer NN model can reasonably approximate any nonlinear function [97]. In this neural network model, a single hidden layer NN with fifteen neurons and one output was used. A bias of 1 was set initially. The longer the length of delay, the heavier the load of the training process is, which will also inevitably increase the training time of

the model. The complex-valued recurrent neural network is trained in 10-min, 20-min, 30-min, 40-min, 50-min, and 60-min time delay modes. For the transfer function, *log-sigmoid* function was selected to be the hidden layer's transfer function due to its efficiency. A linear transfer function was used in the output layer as a convention. *Levenberg-Marquardt* back propagation algorithm is used as the training function for the whole recurrent neural network model. This method is typically used in minimization problems because it appears to be the fastest method in terms of convergence. The weights of each connection between neurons are adjusted in the training process until the errors are within the pre-determined range. To compare the performance of the two modes of recurrent neural network, the accuracy of the model can be evaluated by means of the absolute error (MAE), root mean squared error (RMSE), and mean absolute percentage error (MAPE), as follows:

$$\mathrm{MAE} = \frac{1}{n}\sum_{i=1}^{n}|x_i - \tilde{x}_i| \tag{4.2}$$

$$\mathrm{RMSE} = \sqrt{\frac{1}{n}\sum_{i=1}^{n}(x_i - \tilde{x}_i)^2} \tag{4.3}$$

$$\mathrm{MAPE} = \frac{1}{n}\sum_{i=1}^{n}\left|\frac{x_i - \tilde{x}_i}{x_i}\right| \times 100\,\% \tag{4.4}$$

where x_i and $\tilde{x}_i$ are the i^{th} component of the actual power and predicted wind power respectively, n is the length of the vector.

4.3 Wind power prediction results

Based on the abovementioned, the data shown in Table 4.3was selected to finish wind power prediction model. Data of each group consists of wind speed, wind direction, and wind power generation.

Table 4.3 Data for building prediction model.

Data group	***Start time***	***End time***	***No. of data points***	***Description***
A	4/1/2010 0:00	5/8/2010 23:50	5474	Training data set
B	4/1/2011 0:10	5/8/2011 23:50	5362	Testing data set

In the modeling process, the Group A's data is used for training the model and the Group B's data is used for testing and validate the model. In the training process of neural network, according to the principle of the neural network, training set data will be divided into two parts randomly, one part is for learning the relationship between input data and output data and building the model, which occupies 60% of the total data. The rest 40% data is reserved for validation of the model and for further adjusting value of its weights. So that models built by a same training data set could be different due to neural network's randomness in training. In order to get more accurate results, each model was built by Group A data repeatedly for three times and the prediction results were tested by Group B data repeatedly for three times and then average values are computed. Results from the proposed model were compared with the actual values of the historical data. The error statistics of the prediction results by different time series SP mode CRNN is shown in Table 4.4 and Table 4.5. Model 1 denotes SP mode CRNN with only wind speed as input and, while Model 2 denotes SP mode CRNN with wind vectors as inputs. Table 4.6 shows the error analysis of prediction results by the complex-valued neural network (CVNN) and real-valued neural network (RVNN) models.

Table 4.4 Prediction results analysis.

(MW)	***MAE***		***RMSE***	
Input type	Model 1	Model 2	Model 1	Model 2
10 min	0.113154	0.089989	0.155577	0.10752
20 min	0.116069	0.098686	0.160766	0.110594
30 min	0.128057	0.105806	0.18592	0.120023
40 min	0.152811	0.10768	0.18664	0.123943
50 min	0.159211	0.107691	0.20864	0.126983
60 min	0.170983	0.109486	0.212389	0.129989

Table 4.5 Prediction results analysis.

	MAE		***RMSE***	
Input type	***Model 1***	***Model 2***	***Model 1***	***Model 2***
10 min	0.139006	0.128046	0.122537	0.10752
20 min	0.166274	0.138183	0.134869	0.12824
30 min	0.207417	0.145749	0.158103	0.131131
40 min	0.260309	0.158537	0.175566	0.141543
50 min	0.279406	0.203109	0.1972	0.145394
60 min	0.333623	0.206754	0.223109	0.149074

Table 4.6Prediction methods comparison.

	MAE	***RMSE***	***Std. of Error***	***MAPE***
CVNN	0.161703	0.17136	0.167257	14.867%
RVNN	0.185257	0.195269	0.350537	22.535%

From Table 4.4, Table 4.5 and Table 4.6, the results show that the 10-min delay mode of Model 2 has better performances in the CRNN models, and can be adopted to build power prediction models for WPP. The accuracy suggested by MAPE is 11.2%, which also outperforms the prediction results of CVNN and RVNN, as shown in Table 4.6. In the CRNN models, the accuracy of CRNN's prediction results decreases when increasing the delay length in the model training process. The reason is that the wind is changing rapidly, and thus it is better to predict the wind power by referring the wind status in the nearest previous time. Apparently, the accuracy of prediction results and its consistency for different delay lengths are improved when the direction of the wind is combined into input signals of the neural network. The prediction results of CVNN and RVNN models, which do not include time delay in their training data set, have worse prediction results even compared to Model 2 with 40-min delay. Figure 4.12 shows the prediction results from 4/1/2011 1:20 AM to 4/2/201110:40 AM, where the predicted power generation points are very close to those actual ones. Additionally, there are always some prediction data points with large relative errors, which are larger than 100%. The characteristic of those data points are always generated during low wind speed period, i.e. below 4m/s, which is not important for wind power integration and can be ignored. According to the errors of the prediction results, the power company can compensate the errors by allocating proper power reserve and make some adjustment in scheduling the wind power generation.

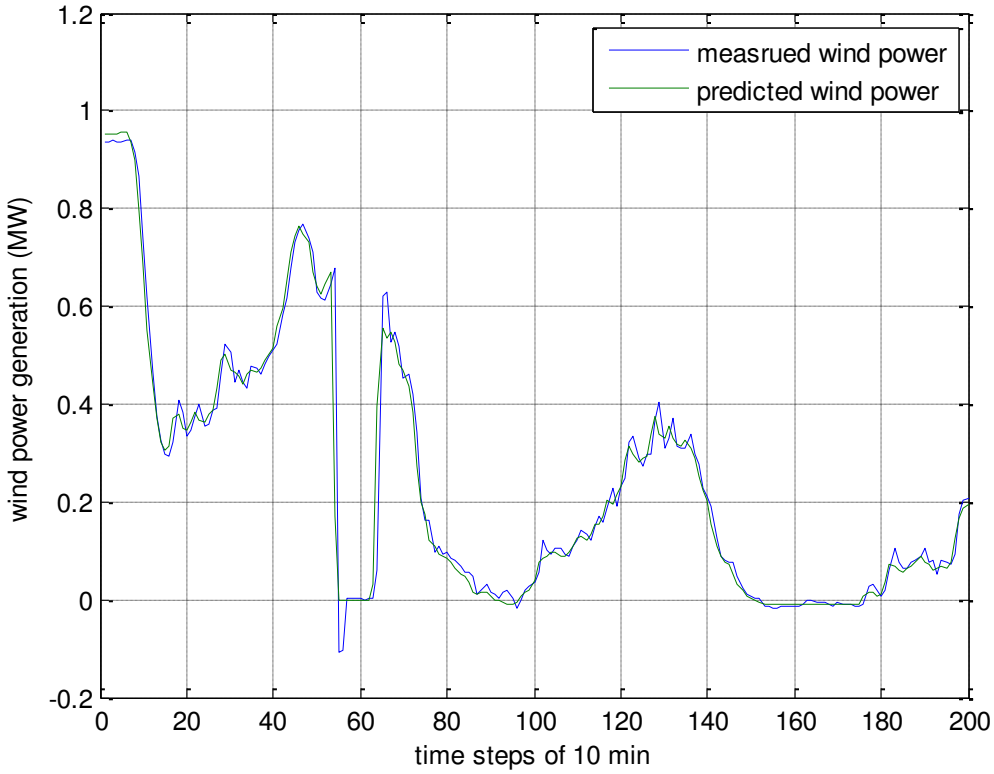

Figure 4.12 Prediction results by 10-min time delay SP mode RNN.

4.4 Summary

This part describes a procedure of predicting wind turbines power generation by using neural networks. A wind turbine in the WPP is selected as an input data source for modeling and to simplify the input signals to the model. In the last step, based on the previous wind power prediction experience [75]-[77], complex-valued recurrent neural network (CRNN) model was chosen to predict the total output of WPP with high accuracy. The methodology has been tested for DFIG type wind turbines in the range of 1-1.5 MW, but may be extended to other types and sizes of wind turbines.

Chapter Five: Islanded wind power system with EMS

5.1 The microgrid concept

The 21st century has brought one of the most revolutionary concepts to the electrical distribution networks: the microgrid, which was defined for the first time in 2001 by Prof Lasseter as "A microgrid is a cluster of micro-sources, storage systems and loads which presents itself to the grid as a single entity that can respond to central control signals." [100]. This definition has been modified along the time since the concept has been applied in many different applications [101], especially in places in which the electrical grid is not present or is very weak, such as islands, rural or emerging countries like China, India or Brazil in which the need of energy is growing with the requirements of industrial development and welfare. This concept has been extended not only to inherently islanded (disconnected from the main grid) systems such as aircrafts [105], ships [106], and even oil platforms, but also to urban areas and camps (e.g. military and U.N. refugees camps) that require high reliability and availability of energy supply. A Microgrid is also able to integrate renewable and non-renewable energy resources and energy storage systems next to the local consumption, giving a unique feature of drastic reduction of transmission losses [103]. Microgrids represent the natural expansion of uninterruptible power supplies and are expected to be the building blocks of the future Smart Grids [104]. Thus, those microgrids should be able to operate flexibly in both grid-connected and islanded modes, allowing resilience, reconfiguration, scalability, and expandability.

One paradigmatic example of a microgrid is placed in Sendai (Japan), supplying 1MW of critical loads, including hospital clinics, a high school and a water plant facility, by using photovoltaic systems, batteries, fuel cells and gas gen-sets. In Sept 9th 2011, the disaster of the 9.0-magnitude earthquake of Fukushima's tsunami produced an electricity blackout in Sendai, except by the area supplied by the microgrid, which was islanded for three days and supplying electricity to clinic laboratories, hospital lights and equipment. The project was proposed and deployed by the largest telecom company in Japan, Nippon Telegraph and Telecom, NTT, which after 4 years of government funding under NEDO, in 2008 the company took complete responsibility. Nowadays, this project represents an alternative solution for centralized electrical systems. "Today, people have no options," says Keiichi Hirose, the head of the Sendai microgrid project. "The idea is to provide some options for electricity." In the Sendai system, customers pay different rates according to the level of reliability that they need.

Wind power generators are often applied in microgrids to meet local needs for electricity. Moreover, a microgrid with wind energy can also benefit customers by providing uninterruptible power, enhancing local reliability, reducing transmission loss and congestion, and supporting local voltage and frequency [78]. However, in a variable speed wind generator based microgrid, stochastic fluctuations in wind speed, weather changing cause fluctuations in electrical supply and may result power quality issues [78][79]including variations in bus voltages [80][81]. In this sense, the wind is a variable and highly fluctuating energy source and the inability to control the amount of energy generated, remains a fundamental problem in microgrids. A paradigmatic example of wind powered islanded microgrid can be found in the Faroe Islands (Denmark), in which

the small island of Nólsoy contains a remote village inhabited by 250 people in 100 households. Notice that most community size systems are combined wind-diesel generation. The idea on Nólsoy was to use traditional Danish version induction generator wind turbines, as they are readily available and cheap, because they are dismantled in high numbers from their sites to give place for new and larger turbines [99]. In order to do this, the generator is operated as a self-excited induction generator (SEIG), which requires a reliable and accurate control system to keep nominal frequency and voltage while running in variable wind and load conditions. However, the output voltage and frequency of a SEIG are totally dependent on the system to which it is connected, in this case to the Microgrid. This inconvenience may be overcome by using DFIG, which has been pointed out as a practical solution for islanded electrical systems and microgrids. This Chapter will present a case study of wind powered microgrid including DFIG based wind turbines and diesel generator.

5.2 Wind powered microgrid description

In this Dissertation, DFIG wind turbines are used to build a microgrid which works in islanded mode. Since DFIG wind turbine has control blocks to realize active power and reactive power control, it is possible to realize load sharing by active power control and the controllable reactive power eliminates the necessity of installation of voltage regulating devices. In a DFIG based islanded wind power system, the active power frequency support and the reactive power voltage support can be accomplished by adjusting active power generation from the rotor side control of DFIG and reactive power from the stator side control of DFIG [82]-[84] separately. The proposed islanded wind power system is local without the need of considering widespread communication system.

An energy management system (EMS) is necessary for operating an islanded wind power system, which can provide control for active power and reactive power among DFIG wind turbines in the islanded wind power system especially for varying wind power generations. The EMS would be responsible to estimate the wind power generated by using neural networks, which should be trained first. The EMS can also decide to disconnect the diesel generator in order to save the amount diesel needed in standby mode, and thus increasing system efficiency while reducing CO2 emissions. The amount of savings can vary depending on the climatic circumstances, diesel generator used, and so on, being out of scope of this Dissertation. In this Dissertation, there is a two-layer control in the EMS, which includes a supervisory control layer and a machine control layer. The purpose of the EMS is to maintain the supply-demand balance in the islanded wind power system. The proposed islanded wind power system is shown in Figure 5.1, which includes a wind power plant (WPP), an auxiliary generator (AG), and a local load.

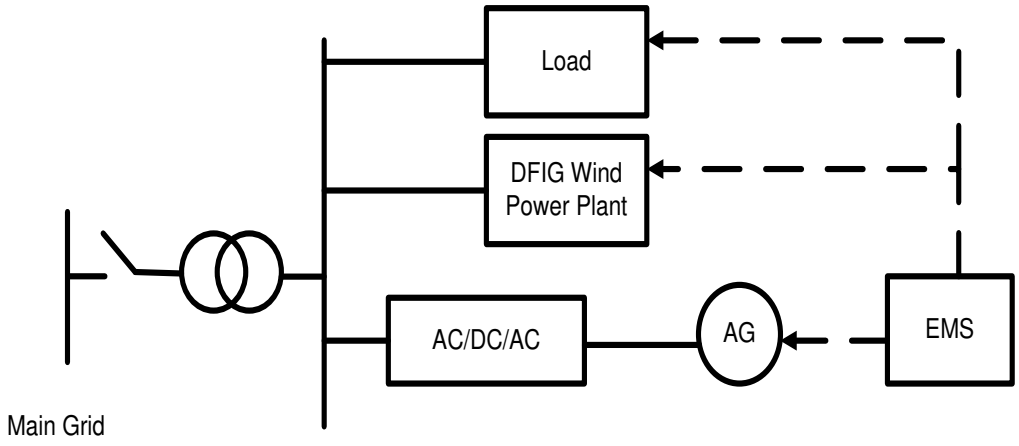

Figure 5.1 Islanded wind power system under study.

Several points have been considered for building this islanded system. Firstly, since wind power is intermitted, frequent wind power generation needs to be updated

timely which could be improved by wind prediction techniques as mentioned in Chapter 4. Wind power prediction technology could solve the problem that wind power generator may not respond timely when operation strategy changes rapidly and unexpectedly. Secondly, if two or more generators are trying to impose frequency and voltage, load sharing local control is needed, since the required power generation may be less than the maximum wind power generation, as discussed in [85][86]. This is the case when the diesel generator is not operating, so that the two DFIGs has to fix frequency and voltage of the islanded system.

The load sharing control is to realize supply-demand balance of the grid because maximum peak power tracking (MPPT) method may cause imbalance in supply-demand when maximum generation of wind is more than required. This problem can be resolved by using energy storage devices, such as super capacitor, flywheel, and pumped hydro [87]-[89]. But methods above can be limited by geography environment, high installation and operation cost, and sometimes it is easy to run out of energy storage. Therefore, energy storage system is not considered to apply in this islanded wind power system. Thirdly, it is important to consider the situation that when wind power generation cannot supply demand. In this Dissertation, fast resource such as gas turbine generator, diesel generator can be applied as auxiliary generator to compensate when wind power production cannot supply the load.

The main purpose of this Dissertation is to research EMS performance on an islanded mode wind power system with coordination of multiple DFIGs' control that can ensure the static supply-demand balance and have good dynamic performances. A microgrid, similarly as a large power system, can be controlled by using hierarchical

control architectures. The typical hierarchical control in micro and macro grids is based on three levels. The primary control (first layer) is based on adding virtual inertia to the system, thus creating dependence between frequency and active power, similarly as in big power systems, in which big inertia machines are always synchronized thanks to this relationship. This way active power sharing is performed at the expenses of drooping the frequency of the generators when the active power increases. This mechanism is also called droop control. It should be noticed that without this mechanism, if two generators try to impose the frequency within an islanded microgrid, due to drifts and differences between them, the angle difference will increase dramatically, thus large circulating currents may produce low efficiency of the system and even trips and damages. For the same reason, the reactive power also can be controlled by means of regulating the voltage. Notice that even though good active/reactive power sharing among generators can be achieved, the frequency and voltage amplitude regulations are compromised.

In the secondary control (second layer), frequency compensation is designed to adjust frequency amplitude deviations within the microgrid produced by the primary control. The control mechanism measures both frequency and voltage errors and if one error is higher than the non-desirable value, which will be processed by a linear controller, typically a proportional-integral (PI) controller sends reference signals to all generators, through this way the droop characteristics can change the operation point without affecting the power sharing performed by the primary control action. The secondary control level in big power systems is well-known as automatic generation control (AGC), which acts over the frequency of the system and is placed in a centralized SCADA system. In a microgrid, this control level takes care of frequency and voltage, and it also

could be used to compensate harmonics and unbalances in some critical points of the microgrid.

The third layer, which is also called the tertiary control layer, is the energy management system of the microgrid. The objective within this layer is to optimize power and energy of the system, according to constraints and electrical variables of the microgrid. Reactive power is normally optimized in this level by using optimization algorithms. However, active power optimization needs to take a reference of the historical energy performance, which means that future variables and states need to be predicted in order to create a rolling horizon. Based on the above analysis, decisions of connection/disconnection or active/reactive power adjusts. This level has not been explored enough in the literature of wind-powered microgrids, which constitutes one of the major focus and contributions of this Dissertation. In order to avoid undesired interactions among levels, the bandwidth is progressively reduced when increasing the control level in the microgrid. Thus the primary control is the faster and the third layer is the slowest one.

In order to test the methodology developed in previous chapters, a wind power microgrid simulation model is presented in this subsection as shown in Figure 5.1. The microgrid system is operated at the voltage level of 575V and then connected to the main grid through a 25kV radial transmission line via a 575V/25kV transformer. The main grid is represented by a three phase voltage source with 100MVA and X/R ratio of 7. A circuit breaker is installed between the main grid and the microgrid system as a protection. The microgrid system shown in Figure 5.1 consists of a 575V distribution system, two wind turbine generators, a load, a traditional diesel generator. This hybrid diesel-wind powered

microgrid is designed to provide maximum 5 MW of load (worst case), so that the configuration includes 5 MW of diesel generation and two DFIG-based wind turbines of 1.5 MW each. That means that the system could eventually provide a maximum power of 8 MW. Since it is hard to estimate the wind power generation, it is considered that the load can vary between 0 and 5 MW. This way, this islanded microgrid has a 60% of wind-power penetration, which is relatively high. If the wind speed is moderated, it may be enough power to supply the most common medium load (2.5 MW) without starting the diesel, for instance during the night. This design is very convenient for places that are windy major part of the year and with the long distance electricity transmission lines.

There are two DFIG wind turbines (WT1, WT2) GE 1.5 MW with parameters presented in [28]. The machine part is modeled in the *d-q-0* frame with two rotor windings on each axis. The excitation and governor systems of the machine are also included in the model. The converters of the DFIG are connected to the system through lumped series RL branches. The control system of the converter is represented in the d-q-0 frame and utilizes the concept of instantaneous power to control real/reactive power exchange with the system by specifying d and q components of converter currents [32][33].There are two three phase RLC loads within this microgrid connected to the two wind turbines WT1 and WT2. Further, a5 MVA diesel generator will be working as an auxiliary generator (AG) when needed. Considering that this size of diesel generators present losses of around 15% at no-load, it will be very interesting to develop energy management systems (EMS) to decide the start or stop of the engine depending on the predictions and forecasting of the wind power in order to save fuel and to optimize the overall fuel consumption. In this sense, as shown in Figure 5.1, this chapter aims to

propose the combination of the proposed neural networks based prediction algorithm to estimate the total amount of wind power generation, and a forecasting algorithm that will be able to predict the variations of the power generated in the near future at the microgrid.

In order to verify and integrate the concepts shown in previous chapters, a Matlab/Simulink model of the hybrid wind-diesel microgrid is presented here. Several scenarios can be simulated based on this islanded wind powered microgrid model, including black start transient analysis, wind powered microgrid with droop control, and wind prediction techniques applied to the microgrid system. In this chapter, techniques to develop future EMS systems that determine the operation mode in order to reduce the time that the diesel generator should be operated in standby mode.

A. Diesel generator modeling and control

The three phase 4-pole synchronous generator model in machine library of Matlab/Simulink has been adopted as the diesel generator in this microgrid system adapting it to the proper system parameters, which has been implemented to simulate electromechanical transients in the proposed microgrid. The diesel engine and governor with an excitation block, accepts three phase voltage and rotor speed signals of the synchronous generator as feedback inputs.

For the diesel generator, initial values of rotor angle/magnitudes, speed deviation, and phases of currents in stator windings are set to 0, initial values of field voltage and speed reference are set to 1 p.u. The diesel generator is assumed ideal presenting sinusoidal and constant speed without consideration of the inertia of the loads. The active power generation of the diesel generator should be controlled according to its reference

value. The PID controller driving the actuator for the speed governor system, shown in Figure 5.2, is applied to improve frequency performance in islanded mode for the wind powered microgrid. In that figure, T_d indicates the reaction time delay of the diesel engine for rotor speed changes, which is selected as 0.024s and is depended on the technology of the diesel generator. The selected value of Td can be found in Power System Factory with the parameters shown in [106]. The purpose of the diesel engine and governor blocks is to maintain its terminal voltage and to control the generated active power according to the reference values [107][108].

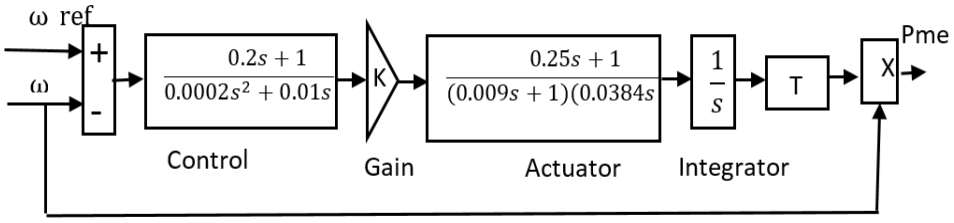

Figure 5.2 Diesel engine and governor system [107].

Notice that when the microgrid system has to restart without the presence of the main grid, the so-called *black start* process, the diesel generator is responsible to fix the voltage and frequency at 1 p.u. To provide a black start, some power stations have small diesel generators, normally called the black start diesel generator (BSDG), which can be used to start larger generators (of several megawatts capacity), which in turn can be used to start the main power station generators. A successful black start could deal with blackout or some emergency situations within the grid under predefined operating procedures, test its ability to restore its system status and frequency, especially with non-

controllable power source, such as wind power, solar power within a short time, e.g. 50s to 100s in paper [109][110].

On the other hand, wind turbines may not be suitable for black start because wind may not be available when needed. In that case, the diesel generator could be started firstly and then DFIG wind turbines would be gradually connected. Nevertheless, the EMS may suddenly decide to stop the diesel generation if a long-term wind power generation is predicted in order to avoid huge diesel losses due to its standby operation which may impact on economic feasibility of the microgrid system and on CO_2 emissions. In that case, DFIG wind turbines may take responsibility of the voltage and frequency.

In order to show the *black start* operation of the microgrid, the following sequence has been simulated. First the diesel generator start, then at 10s the first wind turbine WT1 is connected, and after, the second wind turbine WT2 is connected at 30s. Figure 5.3shows the wind speeds situations during black start. Figure 5.4shows the transient response of the microgrid frequency, with the integration of wind at 10s and 30s, frequency oscillations occur. The frequency of this microgrid system achieved 60 Hz stable within 60s simulation time. Note that the frequency is always inside ±1.5 Hz and going back to 60 Hz in steady-state. Figure 5.5shows the operation of the diesel generator during the wind turbines connection process, in particular the parameters mechanical power (P_{mec}), V_t, and rotating speed are monitored, where *Vt* represents the voltage from the stator. Notice the stable operation of the system in steady state and transient response. Figure 5.6 and Figure 5.7 show two wind turbines' performance in pitch angle and speed. Due to the

existence of the wind speeds and wind turbine's inertia, initial values of pitch angles are large because of wind turbine's stall control system.

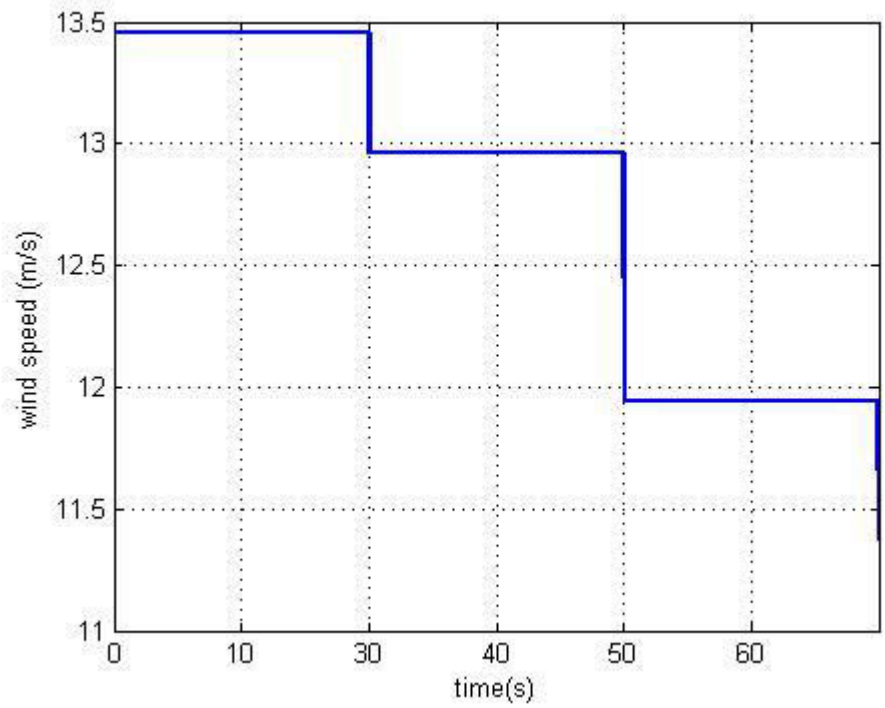

Figure 5.3 Wind speeds during black start

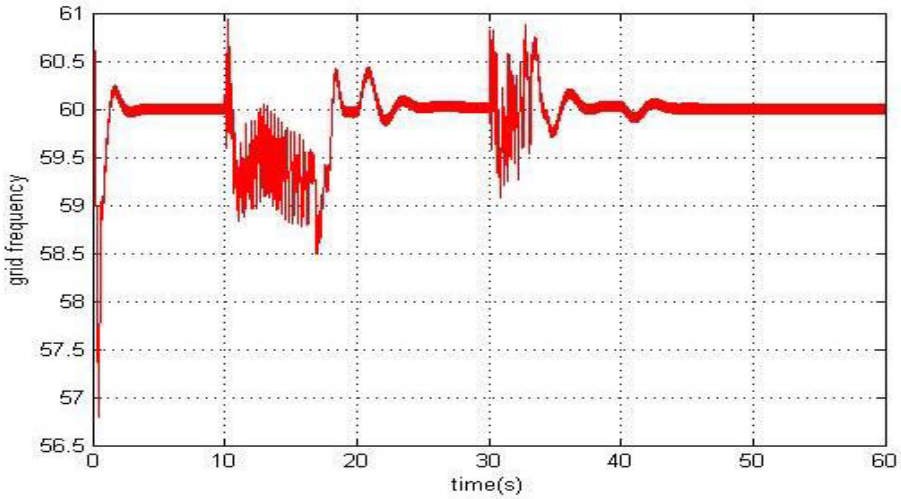

Figure 5.4 Microgrid frequency transient response.

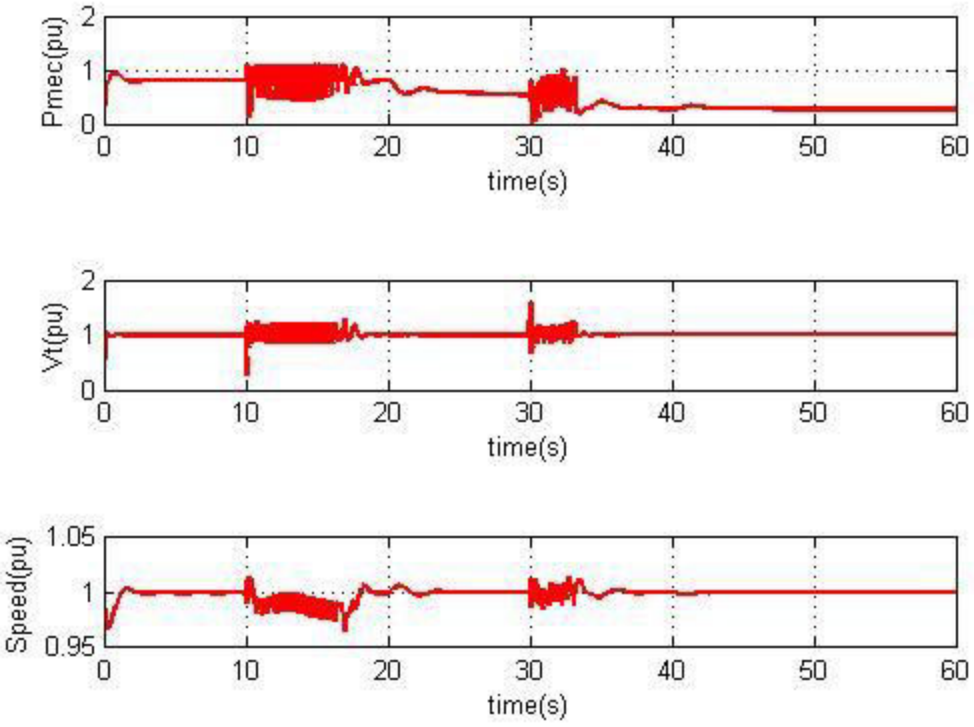

Figure 5.5 Diesel generator transient response (all in p.u.).

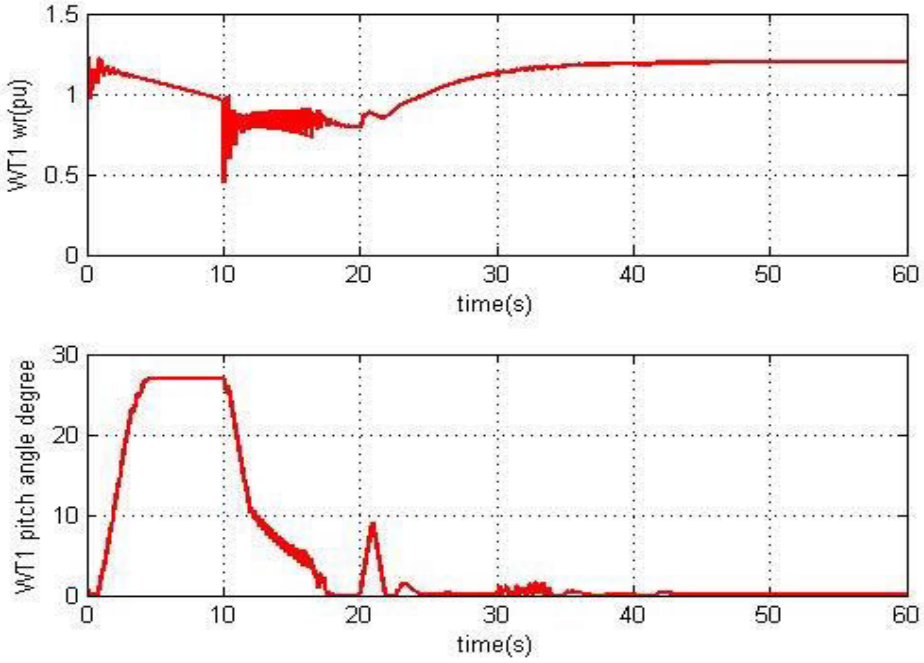

Figure 5.6 Rotor speed (p.u.) and pitch angle (degrees) of WT1.

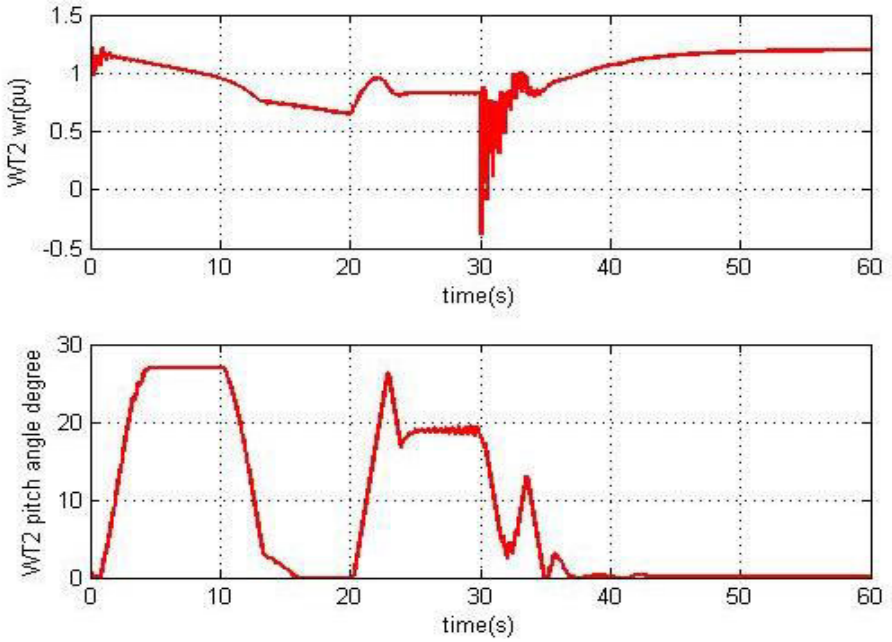

Figure 5.7 Rotating speed (p.u.) and pitch angle (degrees) of WT2.

B. Islanded mode DFIG based wind turbine control

In case of the islanding operation of two or more DFIG are trying to impose frequency and amplitude voltage in the microgrid, as constant-frequency constant-voltage sources, they may conflict when connected them in parallel, resulting in huge circulating currents among generators.

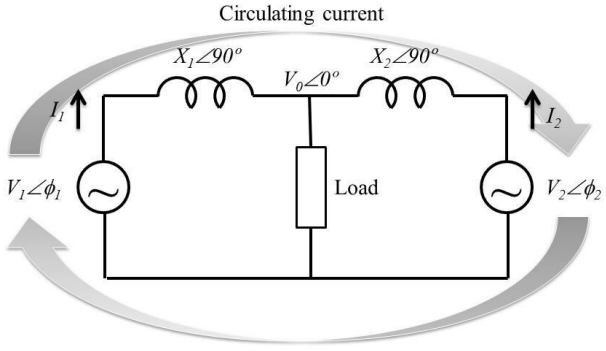

Figure 5.8 Circulating current concept.

In order to study this effect, Figure 5.8 shows two voltage source generators (V_1 and V_2) connected in parallel to the common load through their output inductances (X_1 and X_2). Thus circulating current can be defined as:

$$I_C \equiv I_1 - I_2 \tag{5.1}$$

From that definition, we can derive that:

$$I_C = \frac{V_1 V_2}{X_1 + X_2} \tag{5.2}$$

By expressing the equation in terms of active and reactive power, and by considering the typical small power angles ϕ_1 and ϕ_2 approximation ($sin\phi \cong \phi$ and $\cos\phi \cong \phi$), we can derive the circulating active and reactive power as follows:

$$P_C = \frac{V_1 V_2}{j(X_1 + X_2)} \Delta\phi \tag{5.3}$$

$$Q_C = \frac{V_1}{j(X_1 + X_2)} \Delta V \tag{5.4}$$

being $\Delta\phi$ and ΔV phase and voltage differences, defined as $\Delta\phi \cong \phi_1 - \phi_2$ and $\Delta V \cong V_1 - V_2$. In Figure 5.8, the two generators, when trying to impose individual frequencies, e.g. f_1 and f_2, small frequency difference and drifts can generate phase differences along the time $\Delta\phi=(f_1 - f_2)t$, and according to (5.3), the circulating active power may increase considerably. With the situation goes on, both generators will go out of phase, and angle difference may be higher enough to make the system unstable. In this sense, by observing (5.3), when the power angle increases, also active power increases proportionally with the consideration of the infinitesimal approximation $\sin\phi \cong \phi$. In

order to compensate it, active power can be measured and the individual angle needs to be reduced. However, since the frequency difference can create a ramp of the difference of phases, a steady state error may persist, so that a frequency droop is preferred. Since the phase is the integral of the frequency, thus an integrative effect needs to be created to cancel the steady state error.

Subsequently, from (5.3) and (5.4), we can derive that active power mainly depends on phase difference while reactive power depends mainly on the voltage amplitude. This concept, also well-known in power transmission systems, bring a control approach that tries compensate the circulating active and reactive powers by using a reverse characteristic, i.e. when active power increases, frequency decreases to reduce the power angle. That has been used for decades in large power systems, in which big power plants present those characteristics thanks of the big inertia that presents the synchronous generator. Similar approach can be obtained by reducing the voltage amplitude when increasing the reactive power of the generator. This approach is also known as droop control, which includes the following *P–f* and *Q–V* characteristics:

$$f = f^* + K_P(P^* - P) \tag{5.5}$$

$$V = V^* + K_Q(Q^* - Q) \tag{5.6}$$

where f and V are the nominal microgrid frequency and voltage; P^* and Q^* are the power reference signals received from the secondary control, P and Q are the measured output of the wind turbine, and K_P and K_Q are droop parameters for frequency and voltage, of which value is 0.0004 and 0.0032.

Figure 5.9 shows the $f - P$ and $V - Q$ droop control characteristics, in orange line, and the frequency and voltage deviations with a red arrow (named primary control action). By proper adjustment of P^* and Q^*, the frequency and voltage can be restored properly with a blue arrow (name secondary control action), getting new droop characteristics, in green line.

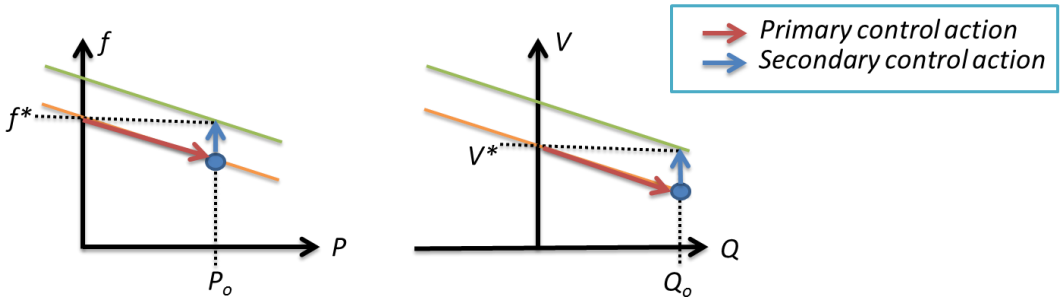

Figure 5.9 f – P and V – Q droop control principle.

Notice that when the generator deliver a certain amount of active and reactive power (P_o and Q_o), according to (5.5) and (5.6), the voltage and frequency deviations for $P^* = Q^* = 0$ can be expressed as

$$\Delta f = -K_P P \tag{5.7}$$

$$\Delta V = -K_Q Q \tag{5.8}$$

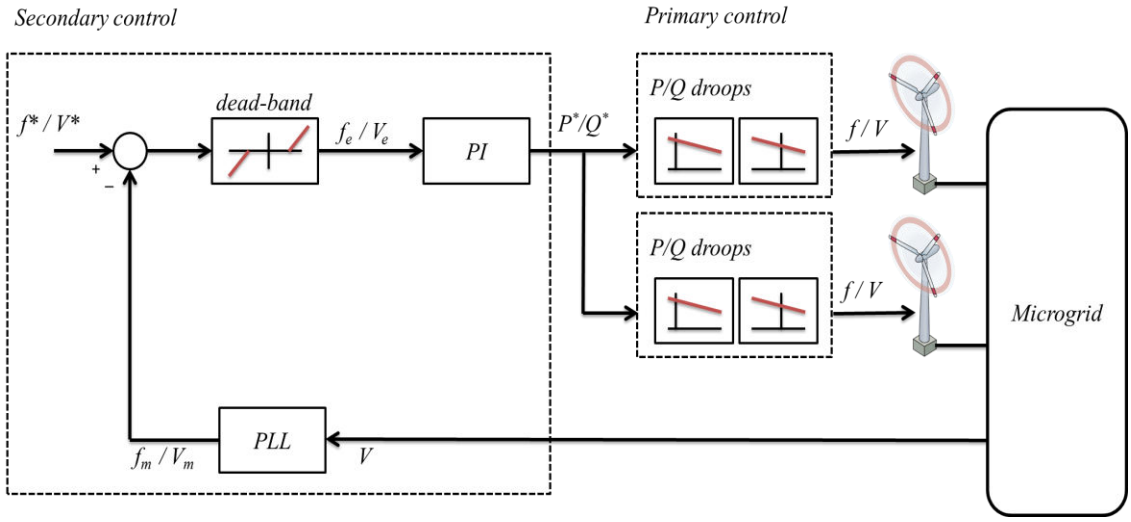

Figure 5.10 Block diagram of the secondary control in relation with the primary control.

The secondary control consists of a centralized controller that measures frequency, or eventually voltage, and computes the error, which passes through a dead-band that discriminates maximum and minimum allowable frequency/voltage deviation. Figure 5.10shows the secondary control bock diagram, consisting in two loops placed in a central controller, often named microgrid central controller (MGCC), which is a SCADA system that may receive signals from the microgrid, measuring frequency and voltage (f_m and V_m) and compare with their references (f^* and V^*). In this sense, the secondary control can be expressed as

$$P^* = k_{pf} f_e + k_{if} \int f_e \, dt \tag{5.9}$$

$$Q^* = k_{pv} V_e + k_{iv} \int V_e \, dt \tag{5.10}$$

being f_e and V_e the frequency and voltage errors after the dead-bands, k_{pf}, k_{if}, k_{pv} and k_{pi} are the proportional and integral constants for the frequency and voltage restorations.

Notice that the time constants of such a PI controllers have to be adjusted to be much slower than the time constant of the wind turbines in order to avoid instabilities.

Finally, the third level of the hierarchical control devoted to develop an EMS will be defined in the next subsection of this chapter.

Considering the scenario in which enough wind power is available for long term, in order to verify the performances of the multi-level control, simulation results have been performed. The system consists of two DFIG supplying local loads. In this case, the islanding operation depends exclusively on the DFIGs since the diesel generator has been disconnected to avoid the stand by consumption. In such a case, droop control has been implemented in each DFIG local control, and a centralized secondary controller has been integrated in the SCADA system in order to restore the system frequency. For that case slightly different wind speed has been considered for each turbine, i.e. 14m/s and 15m/s.

Figure 5.12 shows the frequency for the two wind turbines. At t=0 both DFIGs where operated disconnected each other. At t=5, a transient on the frequency can be seen when interconnecting both DFIGs. Nevertheless, thanks to the droop control, both DFIGs reach a stable frequency point. Note that a frequency deviation can be observed in steady-state due to the inherent action of the droop control. Then, at t=40 the secondary control is activated, allowing the frequency restoring to 60 Hz.

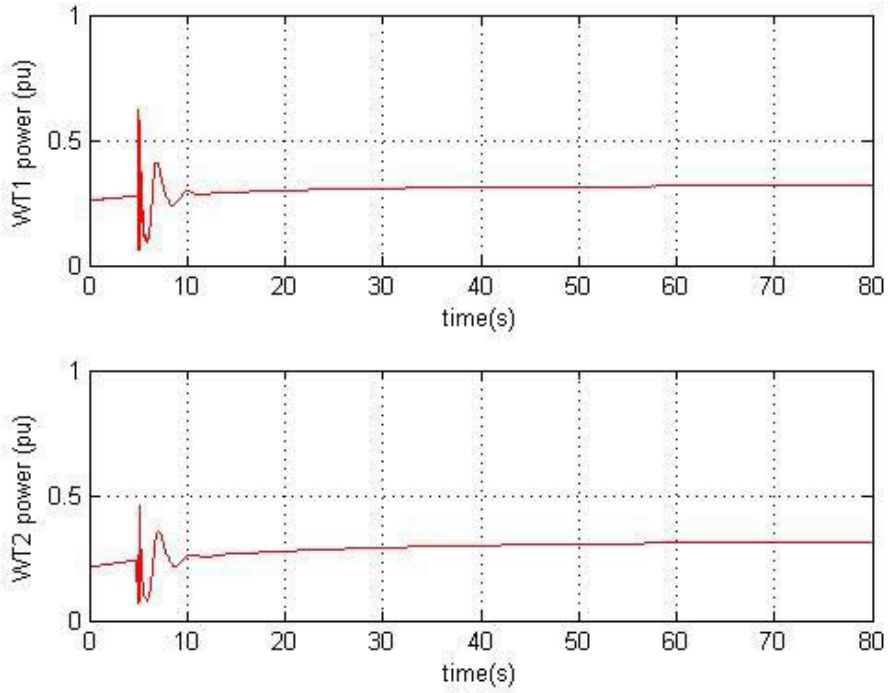

Figure 5.11Wind power generation of WT1 and WT2 (p.u.).

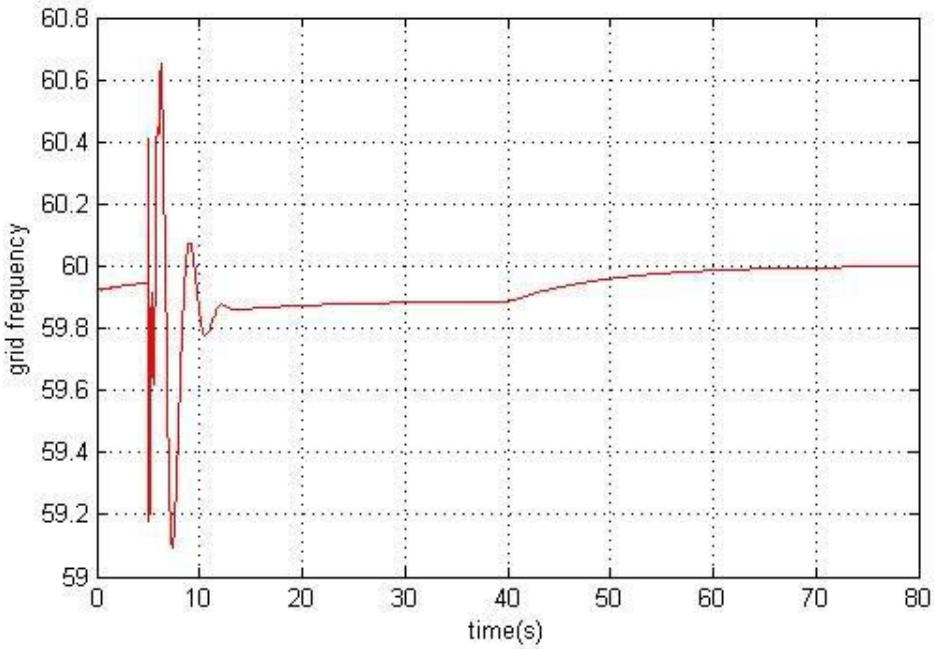

Figure 5.12 Frequency for microgrid and wind turbines.

In Figure 5.11 the power sharing performance among both DFIGs is illustrated, showing similar active powers injected in the microgrid. Finally, the microgrid frequency acquired by a PLL unit placed in the secondary control is monitored as shown in Figure 5.12. In Figure 5.12, the secondary control is manually connected at 40 s. However, the secondary control can be automatically activated by a deadband controller. In large power systems the band is typically tuned around +/-50 mHz. In terms of transient response, the secondary control has to be slower than the primary controller. For instance, in large size power systems the secondary controller may have a time constant of hundreds to thousand seconds, while for a small microgrid, like the one presented in this Dissertation, which just depend on the inertia of the machines included, a time constant of several tenths of seconds is enough.

5.3 Application of wind prediction for improving EMS performance

The wind powered microgrid operates in islanded mode with the help of the wind power prediction information obtained inside the EMS, which enables wind turbine tracks the secondary control given by EMS through wind power prediction results which enable wind turbines regulation by using a cascaded observer. This module will provide the wind powered microgrid a better optimization. During the islanded operation time, wind turbine can restore frequency and voltage regulation of the microgrid system.

The information of the wind powered microgrid would be collected by the EMS system firstly, which includes historical wind speed and wind power generation data, diesel generation operation history, and load information. The short term forecasting module is built based on the wind profile historical data in the data acquisition part, which can get wind power prediction results by means of the neural network models

(NNM) proposed in Chapter 4. The neural network can be built based on the training process of wind profile data, i.e. historical data of wind speed and wind power generation, which gave the neural network parameter values.

The wind speed data adopted by the wind powered microgrid Simulink model is the same as the data source used in Chapter 4, which comes from the aforementioned wind power plant in Colorado, US. The time frame of the wind profile data is from Jan 2011 to March 2011, which includes 6591 sampled wind profiles, including wind speed and wind power generation. The data points were obtained and averaged every 10 minutes from the wind plant and were used to build the prediction models that were integrated in the wind powered microgrid Simulink model.

The neural network is applied to estimate the wind turbine's output active power based on wind speed. For the structure of the neural network, the training data size of the NNM is 6591, and the number of hidden layer units is set to 10. The training algorithm of the neural network model is one-step secant back propagation with a training absolute error of 0.001 and the learning rate is 0.1. The sampled wind profile data sets are normalized to [0, 1] and smoothed through moving average algorithm for increasing the accuracy of regression. Then the normalized sample data of wind speed data points from 5001 to 6591 are used as inputs for the validation of the trained neural network to estimate outputs of wind turbine comparing to the original sampled power, as shown in Figure 5.13, and detailed blocks can be found in Figures 5.14 and 5.15. As for the wind speed prediction part, a support vector machine (SVM) algorithm is applied through a *S-function* in Simulink part, which will predict the future wind speed data based on the

previous ten wind speed data. By using the SVM and the neural network model prediction system, the wind profile will update every 20 seconds, as shown in Figure 5.16.

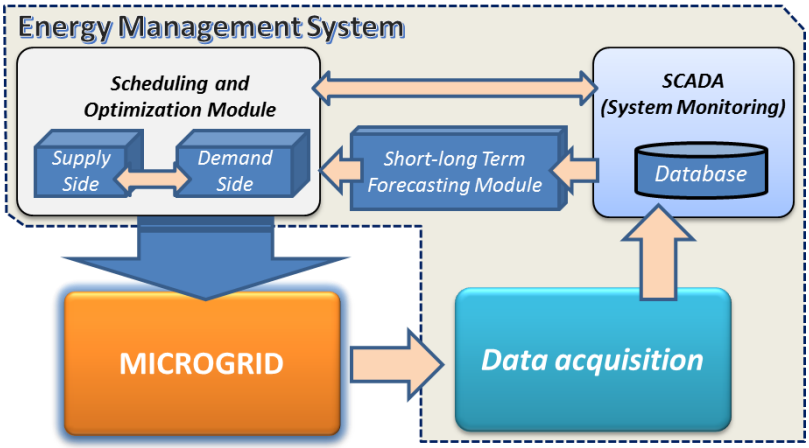

Figure 5.13 Modules that integrate the energy management system.

The scheduling and optimization modules in the EMS part is to maintain the supply and demand balance in islanded mode according to the wind prediction results and to ensure that the microgrid present both good static and dynamic performances. If power demand P_d is less than the extracted wind power P_w, there is no need to use power from the diesel generator and the DFIG wind turbines can be operated with the control mechanism proposed before in order to supply the load either in deloaded mode or in MPPT mode. If P_d is greater than P_w, the diesel engine is turned on to make up the shortfall.

In order to verify the methodology developed in this subsection, the case-study of a wind power microgrid shown in previous subsection has been used. The microgrid system is operating at the voltage level of 575V and then connected to the main grid through a 25kV radial transmission line via a 575V/25kV transformer. The microgrid system consists of a 575V distribution system, two wind turbine generators with wind

power prediction module, loads, a diesel generator. The rated power of the two DFIG wind turbine generators is 1.5 MV and for diesel generator is 5MV.

Results of the predicted wind speed and output wind power of 10 and 20 minutes in advanced are compared with the real wind speed are shown in Figure 5.16 and Figure 5.17. Note the good correlation between the real and predicted wind speed and output powers.

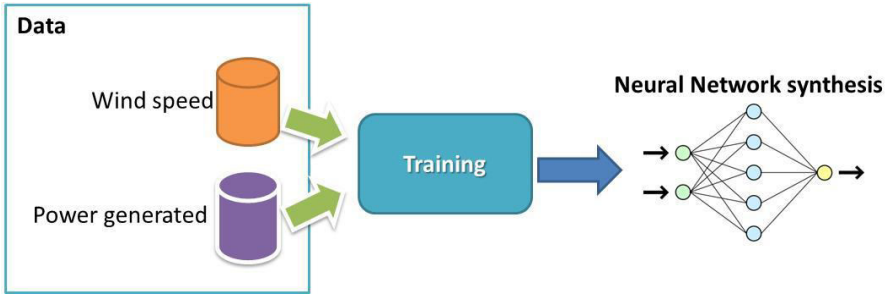

Figure 5.14 Training process of the neural network.

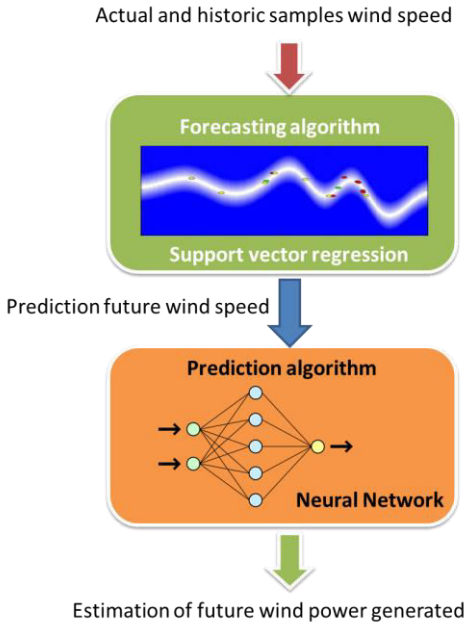

Figure 5.15 Forecasting process to estimate the future wind power generated.

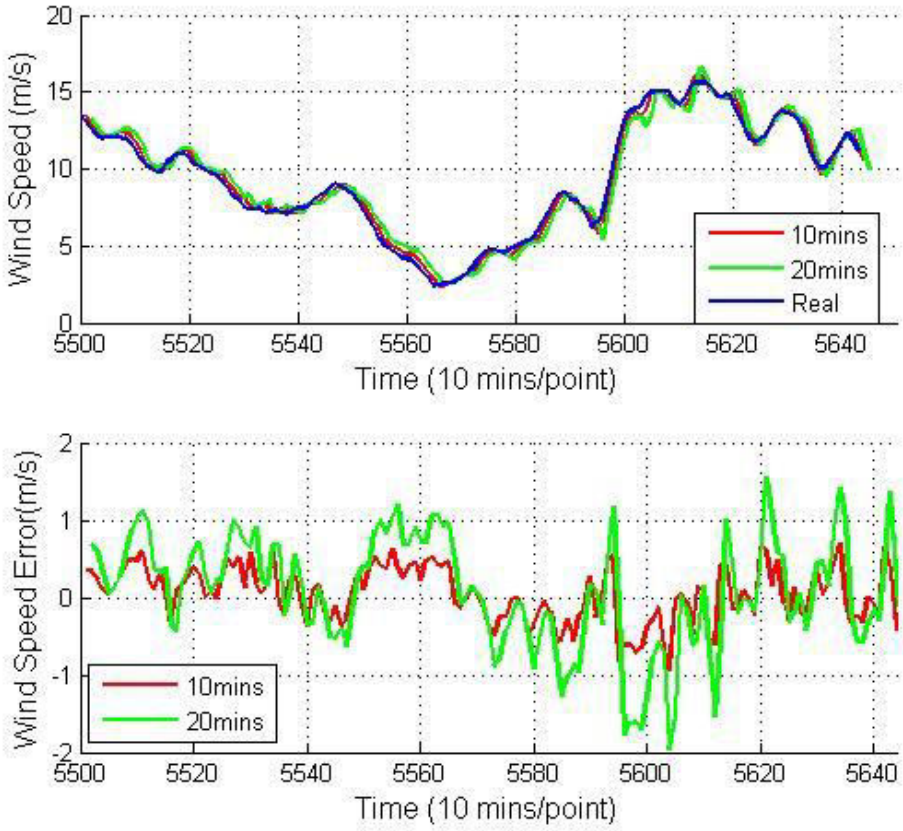

Figure 5.16 Predicted wind speed of 10 and 20 minutes in advance.

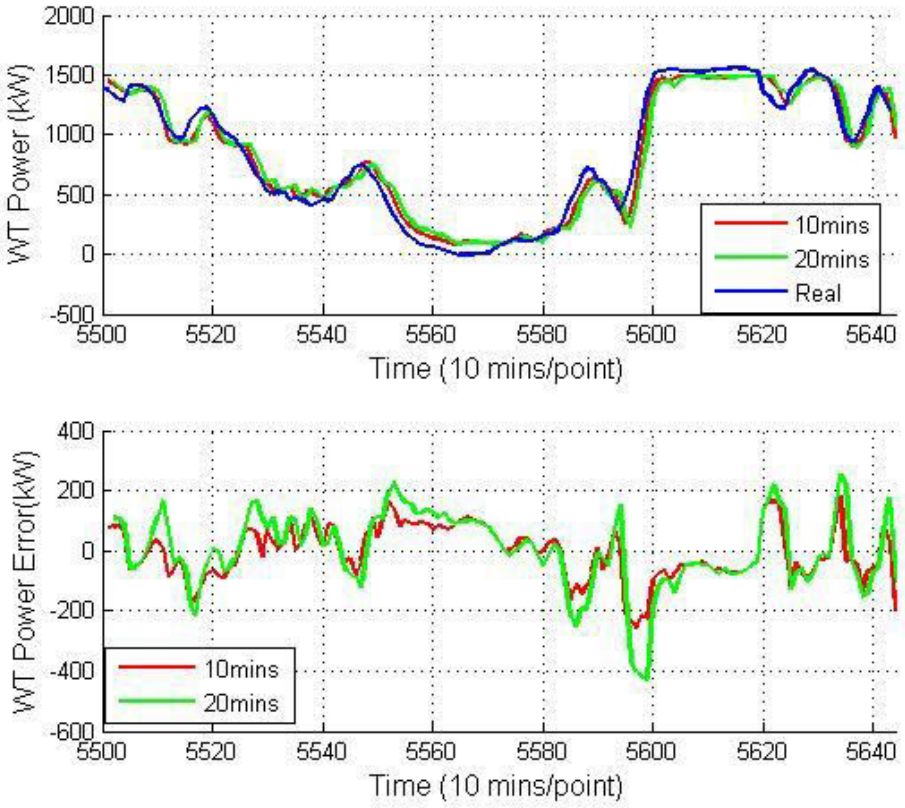

Figure 5.17 Predicted wind power of 10 and 20 minutes in advance.

The simulation results are presented in a period of 200s, so that 10 points discretization are selected to sample it every 10 s. Figure 5.18 shows the discretized data of the wind speed for that period. Figure 5.19 shows the pitch angle variations which present peaks due to the discretization of the wind speed variations. Figure 5.20 illustrates the rotor speed variations, being smooth due to the wind turbine inertia. As a result, in Figure 5.21 and Figure 5.22 the frequency response and voltage of the microgrid system are stable and well-regulated to 60 Hz and 1 p.u., respectively. Finally, Figure 5.23 and Figure 5.24 show the diesel generator and wind turbine output powers. Notice that as the load is constant and the wind power generated lies below the load (1 MW), the diesel generator supply the difference of power in this case. In this case, wind

power is predicted in the near future within the microgrid, when the predicted wind power generation is larger than the load, the diesel generator can be disconnected in order to reduce the stand by losses in diesel which improves the system efficiency and reduces CO2 emissions. In the secondary control of the EMS, frequency and voltage would be controlled regardless of the prediction accuracy of the wind which is in the third level of control. This is not the same case in big power systems, in which the inertia of the wind turbines could be used as a primary frequency reserve.

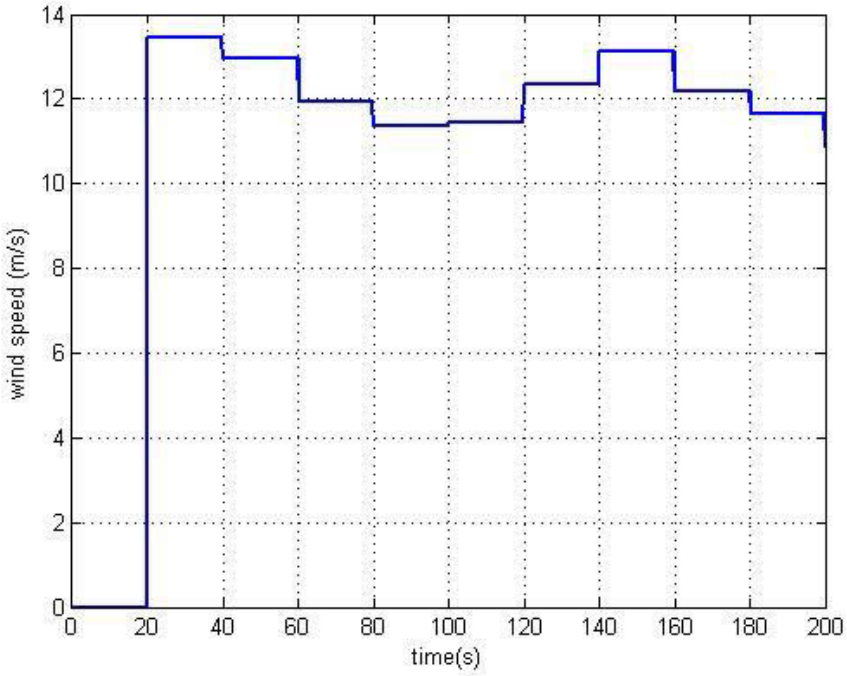

Figure 5.18 Wind speed discretization process.

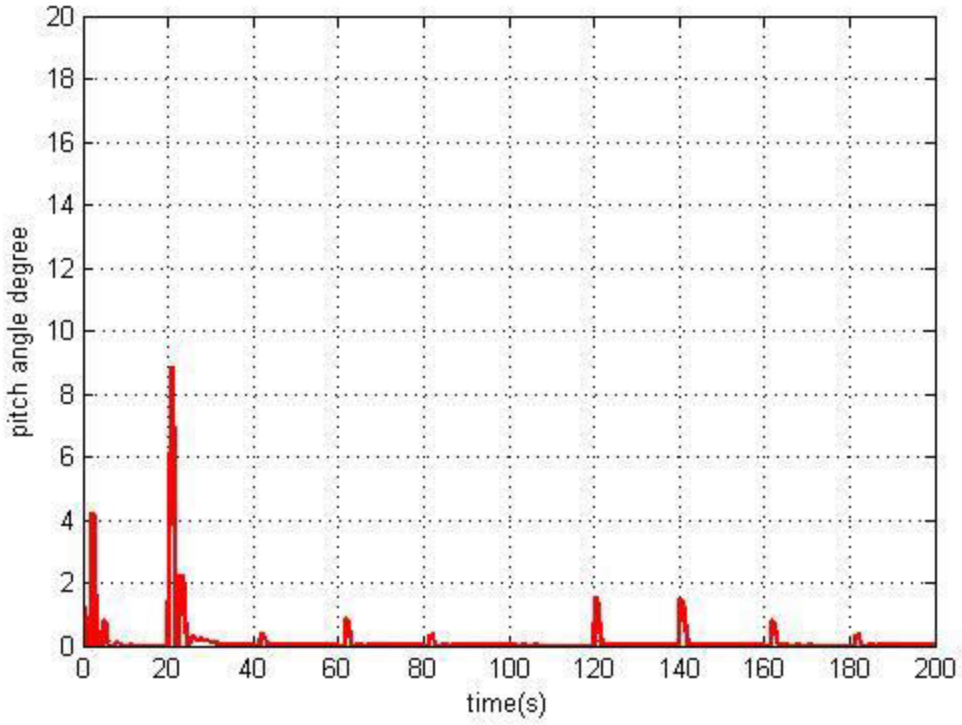

Figure 5.19 Pitch angle variations according to the changes of wind speed.

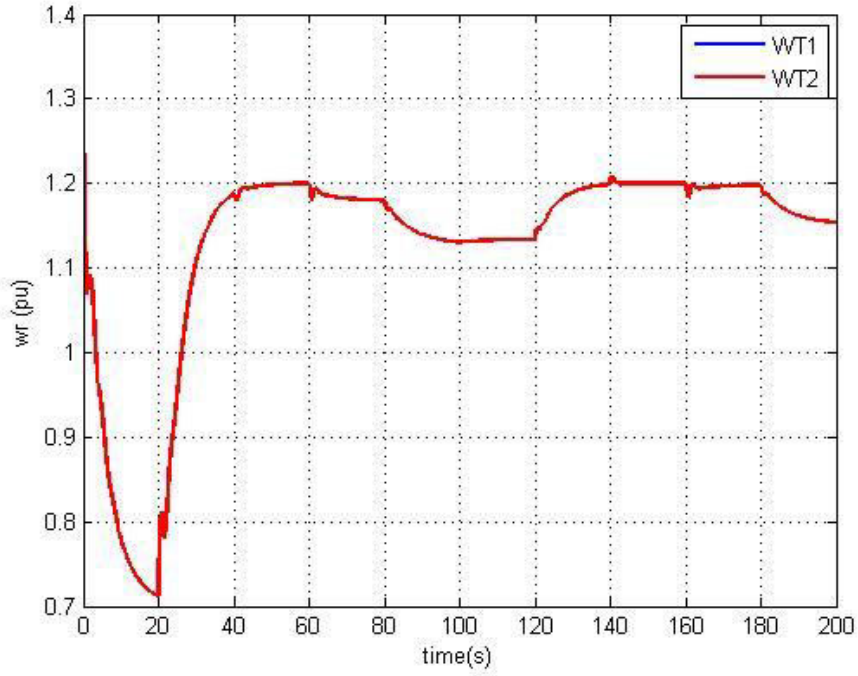

Figure 5.20 Rotor speed variations according to the changes in wind speed.

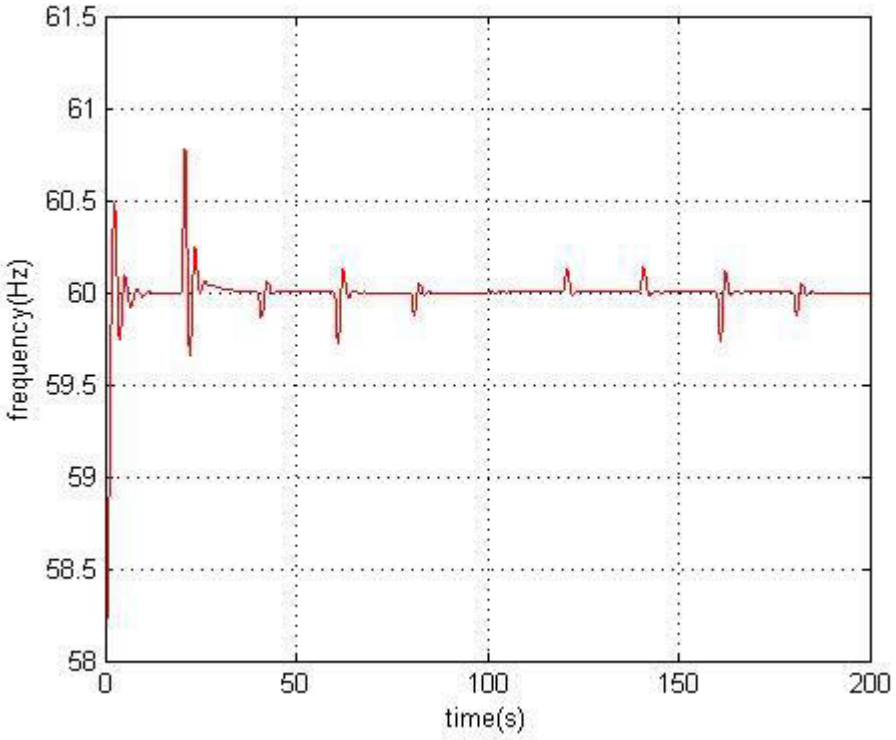

Figure 5.21 Microgrid frequency response according to wind variations.

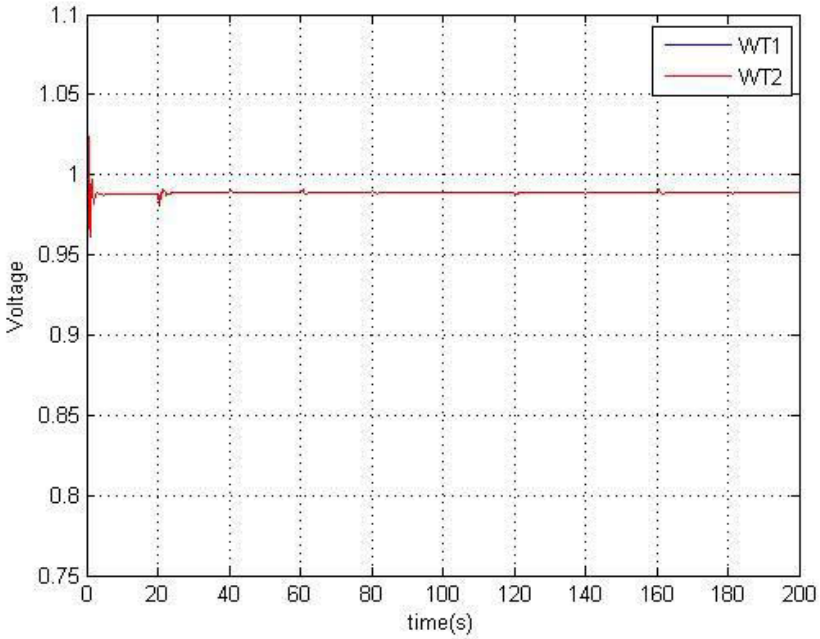

Figure 5.22 Voltage regulation.

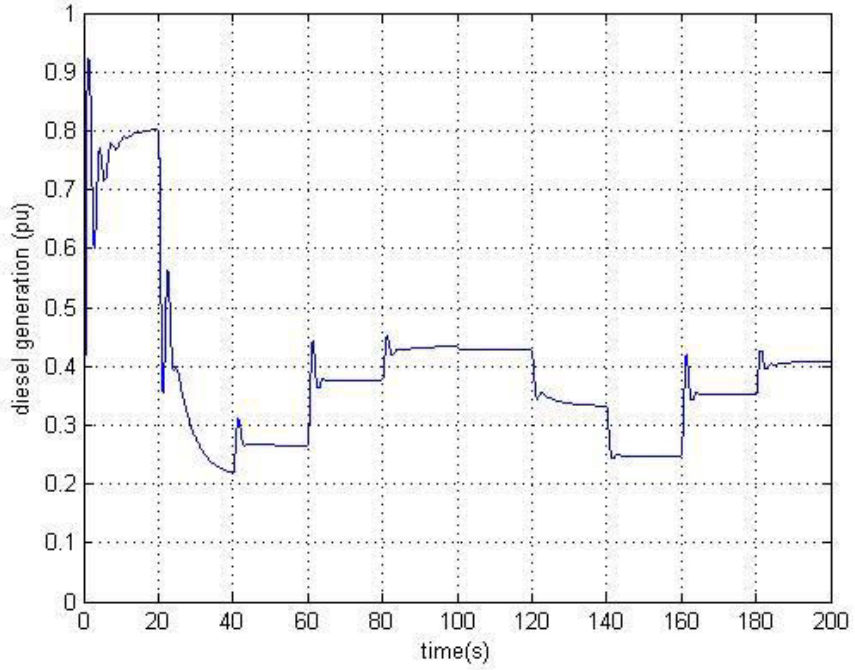

Figure 5.23 Diesel generator output power.

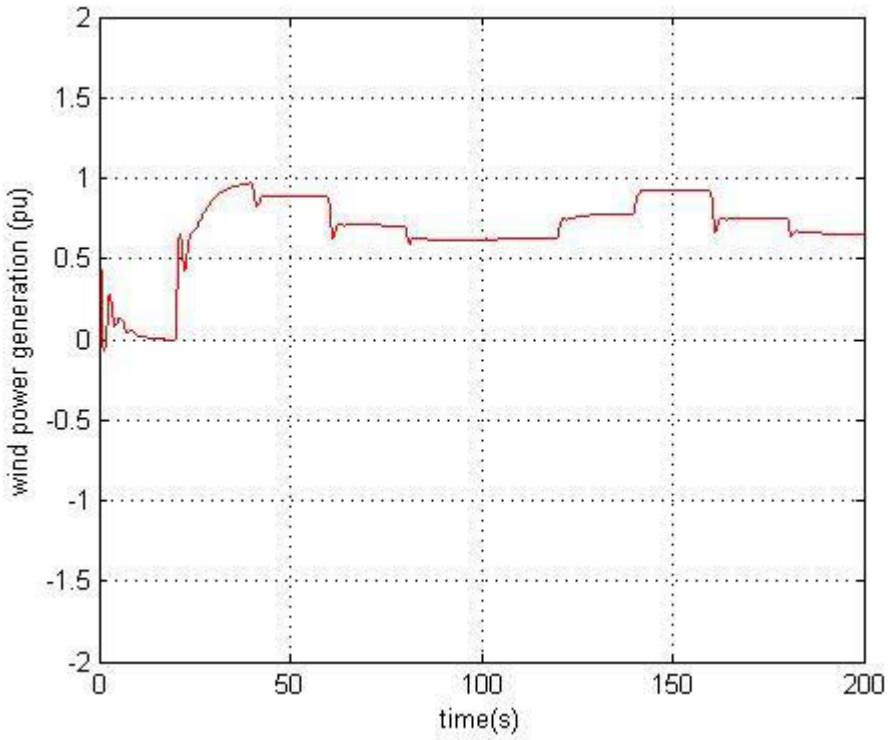

Figure 5.24 Wind turbine output power generated.

5.4 Summary

This Chapter has presented the application of the research done in previous Chapters into a wind powered microgrid system. A hierarchical control has been applied consisted on three main levels. The first level includes all the inner control loops related to the wind generation control, and the external active/reactive power droop controllers. This kind of control is local, so that does not rely on communications, however, it presents frequency and voltage deviations that depend on the active and reactive power delivered. In order to solve this problem, a secondary control is used to restore frequency and voltage at the microgrid. The secondary control is placed in the SCADA system, and it monitors information from the microgrid, computes and give back to the primary droop control references and setting-points. The tertiary control is based on neural networks in order to predict the wind power generated, and to decide the operation of the diesel generator, thus optimizing the microgrid operation.

Furthermore, the black start operation of the microgrid has been introduced and tested, which is needed when restoring the energy to support the loads when the system comes from a black out and still remain in island, i.e. without the help of the main electrical grid.

In summary, the Chapter is showing a case of study in which the methodologies developed along this Dissertation have been tested and integrated, showing the applicability of those methodologies in different blocks of the EMS. The obtained results point out the feasibility of the proposed holistic approach.

Chapter Six: Conclusions

This Dissertation has researched wind power prediction by using neural networks models and its application to islanded wind energy management systems.

Firstly, DFIG wind turbine power generation principles have been studied, which include the electrical equivalent circuit of DFIG model, active and reactive powers adjusted through the rotor speed control, pitch control, direct power control based on synchronous reference frame (*dq*) decoupling of DFIG, and direct torque control (DTC).The comparison between different control strategies are presented and discussed as well.

A grid-connected DFIG wind power system model has been developed in detail and implemented by using *Matlab/Simulink*, which includes the aerodynamic model of the wind turbine, mechanical parts, electrical parts (DFIG, PWM energy conversion part, and so on) of the wind turbine system. An internal model controller (IMC) has been applied as a robust controller allowing wind power system operating under different wind speeds with stable voltage and frequency. The DFIG wind power system structure was developed based on GE 1.5MV wind turbines where different control systems can be designed. The control part in DFIG wind power simulation system is based on a vector control structure with rotor side and grid side control applied to the back-to-back PWM converter. The grid-side control system purpose is to maintain the DC link voltage

constant without consideration of the rotor side. The rotor side control purpose is making sure control of stator side active and reactive power of the wind system under safety speed range, which can realize MPPT energy capture from wind and deloaded control. Simulation results show that DFIG wind turbine systems controllers design meets the requirements that wind power system can provide satisfactory steady state and transient performances, thus allowing wind power system simulation model be applied to microgrid simulation. Those studies aim at making sure wind power has no issue whether being integrated into the grid or working in islanded mode within a microgrid.

Further, this Dissertation built a model of a DFIG wind turbine by using generator vector representation with consideration of harmonic emissions of the DFIG wind turbine. This model can be applied to assess the potential harmonic resonance frequency point in the wind power system and the corresponding harmonic filter circuit can be designed in order to increase the stability of the system.

Due to the feature of intermittency of the wind power generation, the wind power prediction is an essential part in wind power applications, so that neural networks, as a well-developed artificial intelligence algorithms, are applied in this Dissertation to predict the wind power generation of a real plant in northeastern Colorado, US, by using the information of the wind speed and direction. Prediction results achieved relatively good accuracy, while keeping the prediction error within ±20%.

Finally, a wind powered islanded microgrid simulation model has been built, which includes two 1.5 MW DFIG wind turbines, a diesel generator, and local loads. This wind powered microgrid can realize balance of load and power supply by using information of wind power prediction results from neural network model, which assist

the energy management of the microgrid in islanded mode operation. A three level hierarchical control system, including an EMS based on neural networks has been integrated in order to optimize the operation of the microgrid. Furthermore, the black start operation has been performed successfully.

All the theoretical proposals have been tested by means of validated Matlab/Simulink models. The simulation results shown in this Dissertation validate the proposed approaches, showing their feasibility. Those results point out that the research done may benefit more wind power integration into different grid systems configurations in near future.

Chapter Seven: Contributions and future work

7.1 Contributions of the Dissertation

According to the research results presented in this Dissertation, the main contributions are listed as follows:

- Wind turbine model

In this part, a comprehensive review on variable speed wind turbine control strategies has been done for grid connected wind turbines, which may be able to operate on islanded mode. With regards to islanded operated variable speed wind turbines, which should have more stable performance on voltage/frequency at the point of common coupling (PCC), a modified vector control method, i.e. internal model control (IMC) has been applied for the rotor side controller of the DFIG wind turbine through Matlab/Simulink simulation model. This control method shows that the transfer function of a DFIG wind turbine and its corresponding controller parameters can be adjusted in order to satisfy various active/reactive control purposes. Transient responses of the DFIG wind turbine system equipped with IMC have been analyzed, showing that IMC can stabilize voltage and frequency under different wind speed situations. DFIG wind turbine system with IMC method may be used on the control design for other types of wind turbine system.

- Harmonic analysis in wind power system

It is possible to have harmonics injected through rotor side of the wind power generator during its operation, which may degrade the power quality. A mathematic model including harmonic voltage components shows how different harmonic signals are coupled and reveals the generation of different harmonic resonance peaks. This mathematic model can be applied together with the harmonic resonance mode analysis to detect harmonic resonance peaks and it is helpful for different wind power configurations to avoid instabilities caused by harmonics. Part of this content has been published in this paper:

Ziqiao Liu; Abu-Hajar, A.; Gao, D.W., "Modeling DFIG Using General Vector Representation in the Presence of Harmonics," Green Technologies Conference, 2013 IEEE , vol., no., pp.113,119, 4-5 April 2013. doi: 10.1109/GreenTech.2013.25

- Wind power prediction

Since the same type wind turbine may present different performances under different situations, an accurate wind power prediction results can aid having a better power schedule. After a comprehensive study on wind power prediction approaches, neural networks have been selected due to it is low computational cost and can satisfy various requirements of the mathematic modeling. Research of this part is based on historical data collected from a wind power plant located at northeastern Colorado, USA. Two neural network models have been considered to fulfill wind plant power prediction. Probabilistic neural network has been implemented on raw wind profile data to classify and filter out aberrant data ones, which is a key pre-step in wind power prediction model and may obtain good quality data for modeling, thus increasing model accuracy.

Complex valued recurrent neural network model has been built based on wind speed and wind direction, which are two factors affecting wind power generation, and accurate prediction results may be obtained. Moreover, the reasons behind prediction results with large error have been explored. Part of this content has been published in this paper:

> *Ziqiao Liu; Wenzhong Gao; Yih-Huei Wan; Muljadi, E., "Wind power plant prediction by using neural networks," Energy Conversion Congress and Exposition (ECCE), 2012 IEEE , vol., no., pp.3154,3160, 15-20 Sept. 2012. doi: 10.1109/ECCE.2012.6342351*

- Islanded operation of wind powered microgrid

In many cases, the wind power resource is available in remote areas where microgrids are suitable to be built. A microgrid with high wind penetration has been designed in the Dissertation and can operate in islanded mode under different wind speeds. Two features of this wind powered microgrid are the wind speed prediction results that have been applied to assist the energy management system (EMS).The EMS includes prediction and forecasting of the wind power, which allows the system determine the diesel generator mode in order to optimize the microgrid operation. The proposal also includes a hierarchical control system with three levels. In the primary control active and reactive power droops are implemented; in the secondary frequency and voltage regulation is enhanced; and in the third level the EMS is deployed. Further, the microgrid has been tested to operate in island mode and a black start sequence has been implemented and tested.

Although lot of research has been done in the primary and secondary control of microgrids, which are mainly based on fast power sources like photovoltaic systems and/or batteries, little work has been done on integrating a tertiary control that concerns such an intermediate renewable energy source like the wind. Here, in this Dissertation a novel EMS which also includes wind prediction parts that can be used to reduce the amount of fuel consumption, to improve the efficiency, reliability and the lifetime of the machines, depending on the objective functions to be programmed. In this work, all the control levels are accurately designed, from the inner current and voltage loops, DFIG controllers, droop controllers, frequency/amplitude secondary controllers and EMS with wind power prediction.

This new proposal can be also applied to other cases, like photovoltaic systems, estimation and prediction of load variations, thus extending the concept not only to generation but also to load side management. Beyond that, attractive applications such as smart-homes, electrical vehicle charging stations, and virtual power plans could be applied under the same concept.

7.2 Future work

Based on the contributions accomplished in this Dissertation, several future research works are proposed and listed as follows:

- High performances of the internal model controller application on other type various speed wind turbine can be investigated through simulation or lab equipment.
- Battery system could be installed on various speed wind turbine to help generating smoothing wind power and alleviate harmful effects caused by unstable wind power.

- A more detailed protection scheme should be developed for DFIG wind power system to reduce the risks caused by harmonics, resonances and power quality problems, such as over-voltage, disordered frequency, or PWM device protection. Practical laboratory experiments should be implemented based on simulation results.
- A whole harmonic model of the microgrid including converters, generators and loads will be interesting to build in order to assess the power quality of the microgrid. The harmonic model could be added into the EMS in order to improve the power quality by sending harmonic references to the PWM converters or by using separated active power filters.
- It is also possible to add a battery system to the wind powered microgrid in order to check its performance on assisting wind turbines working in islanded mode. Transients phenomena of battery's energy charging/discharging process can be observed, and the voltage/frequency stability performances should be tested under different supply and load situations. Pros and cons of the battery application in microgrids can be researched. Comprehensive tests should be carried out to verify simulation results.
- A more completed EMS could be implemented that could also take care of the demand side, so that load forecasting, prediction and load-shedding may be also included together with an advanced metering infrastructure.

References

[1] WWEA World Wind Energy Report 2014 (April 2015): http://www.wwindea.org/new-record-in-worldwide-wind-installations/.

[2] T. Sun, "Power quality of grid connected wind turbines with DFIG and their interaction with the grid," PhD dissertation, Faculty Eng. Sci., Inst. Energy Technol., Aalborg University, Denmark, 2004.

[3] M.P. Papadopoulos, S.A. Papathanassiou, N.G. Boulaxis, and S.T. Tentzerkis, "Voltage quality change by grid-connected wind turbines," in European Wind Energy Conference, Nice, France, 1999, pp.783-785.

[4] E. Muljadi, D. Yildrim, T. Batan and C. P. Butterfield, "Understanding the unbalanced-voltage problem in wind turbine generation," International Conf. Rec. IEEE IAS Annual Meeting, 1999, vol.2, pp. 1359-1365.

[5] Miller, E. Muljadi and D. S. Zinger, "A variable speed wind turbine power control," IEEE Trans. Energy Conversion, vol.12, no. 2, pp. 181-186.

[6] L. Sainz, J. J. Mesas, R. Teodorescu and P. Rodriguez, "Deterministic and stochastic study of wind farm harmonic currents," IEEE Trans. Energy Conversion, vol.25, no. 4, Dec 2010.

[7] Blooming, T.M., Carnovale, D.J., "Application of IEEE STD 519-1992 harmonic limits," in Proc Pulp and Paper Industry Technical Conference, 2006, Conference Record of Annual, pp. 1-9.

[8] Dugan, Mark F. McGranghan, Surya Santoso, H. Wayne Beaty, "Electrical Power System Quality," second edition, McGraw-Hill, 2002.

[9] Yuan-Kang Wu, Jing-Shan Hong, "A literature review of wind forecasting technology in the world," presented at 2007 IEEE Lausanne Power Tech Conf., pp. 504-509.

[10] Ziqiao Liu, Wenzhong Gao, Yih-Huei Wan, Eduard Muljadi, "Wind Power Plant Prediction by Using Neural Networks," presented at 2012 IEEE Energy Conversion Congress and Exposition (ECCE), pp. 3154-3160.

[11] B.H. Chowdhury, H.T.MA, and N. Ardeshna, "The challenge of operating wind power plants within a microgrid framework," in Proc. Power Energy Conf., IL, 2010, pp. 93-98.

[12] Standard interconnection agreements for wind energy and other alternative technologies, Washington, DC: Federal Energy Regulatory Commission (FERC) 661-A, Dec 2005.

[13] M. Kayikci and J.V. Milanovic, “Reactive power control strategies for DFIG-based plants,” IEEE Trans. Energy Convers., vol.22, pp.389-396, June 2007.

[14] B. Kroposki, R. DeBlasio and M. Simoes, “Benefits of power electronic interface for distributed energy systems,” IEEE Trans. Energy Convers., vol.25, pp. 901-908, Sep 2010.

[15] M. Fazeli, G. M. Asher, C. Klumpner, L. Yao, “Novel integration of DFIG-based wind generators within microgrids,” IEEE Trans. Energy Converters., vol.26, no.3, pp.840-850, Sep 2011.

[16] H. Kanchev, D. Lu, F. Colas, V. Lazarov, B. Francois, “Energy management and operation planning of a microgrid with a PV-based active generator for smart grid applications,” IEEE Trans. Ind. Electron., vol.58, no.10, pp.4583-4592, Oct 2011.

[17] S. Herier, Grid integration of wind energy conversion systems, John Wiley & Sons Ltd, Chichester, 1998.

[18] J.G. Slootweg, H. Polinder, W.L. Kling, ”Dynamic modeling of a wind turbine with direct drive synchronous generator and back to back voltage source converter and its control,” Proc. of the European Wind Energy Conference, pp.1014-1017, July 2001.

[19] T. Butron, D. Sharpe, N. Jenkins, E. Bossanyi, Wind energy handbook, John Wiely & Sons Ltd, Chichester, 2001.

[20] Pena, R.; Cardenas, R.; Asher, G., “Overview of control systems for the operation of DFIGs in wind energy applications,” in Proc. 39th Annual Conference of the IEEE IECON 2013 Industrial Electronics Society, pp.88,95, 10-13, Nov 2013

[21] S. Benelghali, M.E.H. Benbouzid, J.F. Charpentier, “Comparison of PMSG and DFIG for marine current turbine applications,” in Proc. 2010 XIX International Conference on Electrical Machines (ICEM), pp.1-6, 6-8, Sep 2010.

[22] M. Heller and W. Schumacher, ”Stability analysis of doubly fed induction machines in stator flux reference frame,” in Proc. EPE’97 Conf. vol.2, Brussels, Beligum, Sep. 8-10, 1997, pp. 707-710.

[23] F. B. del Blanco, M.W. Degner, and R.D. Lorenz, “Dynamic analysis of current regulators for ac motors using complex vectors,” in Proc. ICEMS’01 Conf., vol.2, Shenyang, China, Aug 18-20,2001, pp.1203-1206.

[24] P. Jungwoo, L. Kiwook, K. Dongwook, L. Kwangsoo, and P. Jinsoon, “An encoder free grid synchronization method for a doubly fed induction generator,” in Proc. EPE Conf., Aalborg, Denmark, Sep 2-5,2007, pp.1-6.

[25] Z. Xueguang, X. Dianguo, L. Yongqiang, and M. Hongfei, "Study on stage wise control of connecting DFIG to the grid," in Proc. IEEE-IPEMC, Shanghai, China, Aug 14-16, 2006, pp.1-5.

[26] G. Iwanski and W. Koczara, "Grid connection to stand alone transitions of slip ring induction generator during grid faults," in Conf. Rec. IEEE-IPEMC, Shanghai, China,Aug.14-16, 2006, pp.1-5.

[27] S. Muller, M. Deicke, and R.W. DeDoncker, "Doubly fed induction generator system for wind turbines," IEEE Ind. Appl. Mag., vol.17, no.1, pp.26-33, May-Jun.2002.

[28] H. Akagi and H. Sato, "Control and performance of a doubly fed induction machine intended for a flywheel energy storage system," IEEE Trans. Power Electron., vol.17, no.1, pp.109-116, Jan.2002.

[29] R. Pena, J.C. Clare, and G.M. Asher, "Doubly fed induction generator using back-to-back PWM converter and its application to variable speed wind energy generation," Proc. IEE B Electr. Power Appl., vol. 143, no.3, pp.231-241, May 1996.

[30] B. Hopfensperger, D.J. Atkinson, and R.A. Lakin, "Stator flux oriented control of a doubly fed induction machine with and without position encoder," Proc. Inst. Elect. Eng., vol.147, pp.241-250, Jul 2000.

[31] W. Leonhard, Control of Electrical Drives, 2nd ed. Berlin, Germany: Springer-Verlag, 1996.

[32] R. Pena, J.C. Clare, and G.M. Asher, "Doubly fed induction generator using back to back pwm converters and its application to variable speed wind energy generation," Proc. Inst. Elect. Eng., vol.143, pp.231-241, May 1999.

[33] Y. Tang and L. Xu, "Flexible active and reactive power control strategy for a variable speed constant frequency generating system," IEEE Trans. Power Electron., vol.10, no.4, pp.472-478, Jul 1995.

[34] L. Xu and C. Wei, "Torque and reactive power control for a doubly fed induction machine by position sensorless scheme," IEEE Trans. Ind. Appl., vol.31, no.3, pp.636-642, May/Jun. 1995.

[35] S. Wang and Y. Ding, "Stability analysis of field oriented doubly fed induction machine drive based on computer simulation," Elect. Mach. Power Syst., vol.21, no.1, pp.11-24, 1993.

[36] Lie Xu, Phillip Cartwright, "Direct active and reactive power control of DFIG for wind energy generation", IEEE Trans. Energy Conversion, pp. 750-758, Sep 2006.

[37] W. Leonhard, Control of Electrical Drives, 2nd ed. Berlin, Germany: Springer-Verlag, 1996.

[38] R. Data and V.T. Ranganthan, "Decoupled control of active and reactive power for a grid-connected doubly fed wound rotor induction machine without position sensors," in Proc. IEEE Industry Applications Soc. Annual Meeting, vol.4, Phoneix, AZ, Oct 1999, pp.2623-2628.

[39] L. Morel, H. Godfroid, A. Mirzaian, and J. Kauffmann, "Doubly fed induction machine: Converter optimization and field oriented control without sensor," Proc. Inst. Elect. Eng., vol.145, no.4, pp.360-368, Jul 1998.

[40] J. Arbi, I. Slama-Belkhodja, and S.A. Gomez, "Control of a DFIG-based wind system in presence of large grid faults: Analysis of voltage ride through capability," in Proc. IEEE-EPQU, Barcelona, Spain, Oct 2007, pp.1-6.

[41] Z. Liu, O.A. Mohammed, and S. Liu, "A novel direct torque control of doubly fed induction generator used for variable speed wind power generation," in Proc. IEEE Power Eng. Soc. Gen. Meeting, Jun.2007, pp.1-6.

[42] L. Xu and P. Cartwright, "Direct active and reactive power control of DFIG for wind energy generation," IEEE Trans. Energy Convers., vol.21, no.3, pp. 750-758, Sep 2006.

[43] D. Zhi and L. Xu, "Direct power control of DFIG with constant switching frequency and improved transient performance," IEEE Trans. Energy Convers., vol.22, no.1, pp.110-118, Mar 2007.

[44] G. Abad, M.A. Rodriguez, and J. Poza, "Two level VSC based predictive direct torque control of the doubly fed induction machine with reduced torque and flux ripples at low constant switching frequency," IEEE Trans. Power Electron., vol. 23, no.3, pp. 1050-1061, May 2008.

[45] Takahashi and T. Noguchi, "A new quick response and high efficiency control strategy of an induction motor," IEEE Trans. Ind. Appl., vol. 22, no.5, pp.820-827, Sep-Oct 1986.

[46] M. Depenbrock, "Direct self-control of inverter fed induction machines," IEEE Trans. Power Electron., vol.3, no.5, pp.420-429, Oct 1989.

[47] G.S. Buja and M.P. Kazmierkowski, "Direct torque control for PWM inverter fed AC motors—A survey," IEEE Trans. Ind. Electron., vol.51, no.4, pp.744-745, Aug 1995.

[48] M.P. Kazmierkowski and A. Kasprowicz, "Improved direct torque and flux vector control of PWM inverter-fed induction motor drives," IEEE Trans. Ind. Electron., vol.42, no.4, pp.344-350, Aug 1995.

[49] P. Vas, Sensorles Vector and Direct torque control. Oxford, U.K. Charendon, 1998.

[50] L. Zhong, M.F. Rahman, W.Y.Hu, and K.W. Lim, “Analysis of direct torque control in permanent magnet synchronous motor drives,” IEEE Trans. Power Electron., vol. 12, no.3, pp.528-536, May 1998.

[51] A.D. Cheok and Y. Fukuda, “A new torque and flux control method for switched reluctance motor drives,” IEEE Trans. Power Electron., vol. 17, no.4, pp.543-557, Jul 2002.

[52] K.P. Gokhale, D.W .Karaker, and S.J. Heikkia, “Controller for a wound rotor slip ring induction machine,” U.S. Patent, 6448735B1, Jul 22, 2002.

[53] JihenArbi, ManelJebali-Ben Ghorbal, IlhemSlama-Belkhodja, LotfiCharaabi, “Direct virtual torque control for doubly fed induction generator grid connection,” IEEE Trans. Industrial Electronics, pp. 4163-4173, Oct 2009.

[54] J. Ribrant and L. Bertling, “Survey of failures in wind power systems with focus on Swedish wind power plants during 1997-2005,” in Proc. IEEE Power Eng. Soc. Gen. Meeting, Jun 2007, pp.1-8.

[55] S.A. Gomez and J.L.R. Amenedo, “Grid synchronization of doubly fed induction generators using direct torque control,” in Proc. IEEE IECON Conf., Nov 2002, pp.3338-3343, CD-ROM.

[56] T. Noguchi, H. Tomiki, S. Kondo, and I. Takahashi, “Direct power control of PWM converter without power-source voltage sensors,” IEEE Trans. Ind. Appl., vol.34, no.3, pp.473-479, May-Jun 1998.

[57] M. Malinowski, M.P. Kazmierkowski, S. Hansen, F. Blaabjerg, and G.D. Marques, “Virtual flux based direct power control of three phase PWM rectifiers,” IEEE Trans. Ind. Appl., vol.37, no.4, pp.1019-1027, Jul-Aug 2001.

[58] G. Escobar, A.M. Stankovic, J.M. Carrasco, E. Galvan, and R. Ortega, “Analysis and design of direct power control (DPC) for a three phase synchronous rectifier via output regulation subspaces,” IEEE Trans. Power Electron., vol. 18, no.3, pp. 823-830, May 2003.

[59] Pablo Ledesma, Julio Usaola, “DFIG model for transient stability analysis,” IEEE Trans. Energy Conversion, pp.388-397, Jun 2005.

[60] P. Kundur, Power System Stability and Control. New York: McGraw Hill, 1994.

[61] A.E. Feijoo, J. Cidras, and C. Carrillo, “A third order model for the doubly fed induction machine,” Elect. Power Syst. Res., vol. 56, pp.121-127, 2000.

[62] K.C Wong, S.L Ho, K.W.E Cheng, “Direct control algorithm for doubly fed induction generators in weak grids,” IET Electric Power Applications, pp.371-380, 2008.

[63] Wilsun Xu, Zhengyu Huang, Yu Cui, Haizheng Wang, "Harmonic resonance mode analysis," IEEE Transactions on Power Delivery, vol.20, no.2, April 2005.

[64] Bradt, M., Badrzadeh, B., Camm, E., Mueller, D., Schoene, J., Siebert, T., Starke, M., Walling, R., "Harmonics and resonance issues in wind power plants," in Proc. 2011 IEEE Power and Energy Society Meeting, pp. 1-8, 24-29 July 2011.

[65] Yu Cui, Wilsun Xu, "Assessment of potential harmonic problems for systems with distributed or random harmonic sources," in Proc. IEEE Power Engineering Society General Meeting, 2007.

[66] E. Muljadi, D. Yildrim, T. Batan and C. P. Butterfield, "Understanding the unbalanced-voltage problem in wind turbine generation," International Conf. Rec. IEEE IAS Annual Meeting, 1999, vol.2, pp. 1359-1365.

[67] Miller, E. Muljadi and D. S. Zinger, "A variable speed wind turbine power control," IEEE Trans. Energy Conversion, vol.12, no. 2, pp. 181-186, 1997.

[68] Roger C. Dugan, Mark F. McGranghan, Surya Santoso, H. Wayne Beaty, "Electrical Power System Quality," second edition, McGraw-Hill, 2002.

[69] K. Rauma, K. N. Md Hasan, C. Gavriluta, C. Citro, "Resonance analysis of a wind power plant with modal approach," in Proc. IEEE International Symposium on Industrial Electronics (ISIE), 2012, vol., no., pp.2042,2047, 28-31 May 2012.

[70] Yuan-Kang Wu, Jing-Shan Hong, "A literature review of wind forecasting technology in the world," presented at 2007 IEEE Lausanne Power Tech Conf., pp.504-509.

[71] Miller, A., Muljadi, E. and Zinger, D.S."A Variable Wind Turbine Power Control," IEEE Trans. Energy Conversion, vol. 12, no.2, 1997, pp. 181-186.

[72] Shuhui Li, Donald C. Wunsch, Edgar A. O'Hair and Michael G. Giesselmann, "Using neural networks to estimate wind turbine power generation," IEEE Trans. on Energy Conversion, vol. 16, pp.267-282, Sep 2001.

[73] Takahiro Kitajima, Takashi Yasuno, "Output Prediction of Wind Power Generation System Using Complex-valued Neural Network," in Proc. 2010 SICE Annual Conf., pp.3610-3613.

[74] Andrew Kusiak, Haiyang Zheng, Zhe Song, "Short-term prediction of wind farm power: a data mining approach," IEEE Trans on Energy Conversion, vol.24, no.1, pp.125-135, Mar 2009.

[75] Yih-Huei Wan, Erik Ela, Kirsten Orwig, "Development of an Equivalent Wind Plant Power Curve," NREL, Golden, CO, Tech. Rep. NREL/CP-550-48146, Jun 2010.

[76] Kang Meei-Song, Chen Chao-Shun, Ke Yu-Lung and Lin Chia-Hung, " Load Profile Syn Dissertation and Wind Power Generation Prediction for an Isolated Power System," IEEE Trans. on Industry Applications, vpl.43, pp.1459-1484, Nov 2007.

[77] http://www.mathworks.com/help/toolbox/nnet/ug/bss38ji-1.html

[78] T. Sun, Z. Chen, F. Blaabjerg, "Flicker study on variable speed wind turbines with doubly fed induction generators," IEEE Trans. Energy Convers., vol.20, pp.896-905, Dec 2005.

[79] Y.S. Kim, D.J. Won, "Mitigation of the flicker level of a DFIG using power factor angle control," IEEE Trans. Power Del., vol.24, pp.2457-2458, Oct 2009.

[80] T. Thiringer, "Frequency scanning for power system property determination applied to a wind power grid," IEEE Trans. Power Syst., vol.21, pp.702-708, May 2006.

[81] Larsson, "Flicker emission of wind turbines during continuous operation," IEEE Trans. Energy Convers., vol. 17, pp. 114-118, Mar 2002.

[82] R. Li, S. Bozhko, G. M. Asher, L. Yao, and L. Ran, "Offshore grid frequency control design for line commutated converters high voltage direct current link connected wind farm," IET Renew. Power Gener., vol. 1, no. 4, pp. 211–219, 2007.

[83] M. Shahabi, M. R. Haghifam, M. Mohamadian, and S. A. Nabavi-Niaki, "Microgrid dynamic performance improvement using a doubly fed Induction wind generator," IEEE Trans. Energy Convers., vol. 24, no. 1, pp. 137–145, Mar 2009.

[84] T. Sun, "Power quality of grid connected wind turbines with DFIG and their interaction with the grid," Ph.D. dissertation, Faculty Eng. Sci., Inst. Energy Technol., Aalborg Univ., Aalborg, Denmark, 2004.

[85] R. G. de Almeida, E. D. Castronuovo, and J. A. P. Lopes, "Optimum generation control in wind parks when carrying out system operator requests," IEEE Trans. Power Syst., vol. 21, no. 2, pp. 718–725, May 2006.

[86] P. Moutis, E. Loukarakis, S. Papathanasiou, and N. D. Hatziargyriou, "Primary load-frequency control from pitch-controlled wind turbines," Proc. 2009 IEEE Bucharest Power Tech, pp. 1–7.

[87] W. Leonhard and E. M. Grobe, "Sustainable electrical energy supply with wind and pumped storage—A realistic long-term strategy orutopia?," in Proc. IEEE Power Eng. Soc. Gen. Meet., Jun. 2004, vol.2, pp. 1221–1225.

[88] Daneshi, M. Khederzadeh, N. Sadrmomtazi, and J. Olamaei, "Integration of wind power and energy storage in SCUC problem," in Proc. World Non-Grid-Connected Wind Power Energy Conf. (WNWEC),Nov 2010, pp. 1–8.

[89] L. Qu, W. Qiao, “Constant power control of DFIG wind turbines with supercapacitor energy storage,” IEEE Trans. Ind. Appl., vol. 47,no. 1, pp. 359–367, Jan/Feb 2011.

[90] R. Aghatehrani, R. Kavasseri, “Reactive power management of a DFIG wind system in microgrids based on voltage sensitivity analysis,” IEEE Trans. Sustainable Energy, vol.2, no.4, pp.451-458, Jun 2011.

[91] M. Falahi, S. Lotfifard, M. Ehsani, K. Butler-Purry, “Dynamic model predictive based energy management of DG integrated distribution systems,” IEEE Trans. Power Delivery, vol.28, no.4, pp.2217-2227, Aug 2013.

[92] Wei Zhang, Yingliang Xu, Wenxin Liu, Frank Ferrese, Liming Liu, “Fully distributed coordination of multiple DFIGs in a microgrid for load sharing,” IEEE Trans. Smart Grid, vol.4, no.2, Jun. 2013.

[93] Meghdad Fazeli, Greg M. Asher, Christian Klumpner, Liangzhong Yao, “Novel integration of DFIG-based wind generators within microgrids,” IEEE Trans. Energy Conversion, vol.26, no.4, Sep 2011.

[94] F. Katiraei, M.R. Iravani, P.W. Lehn, “Microgrid autonomous operation during and subsequent to islanding process,” IEEE Trans. Power Delivery, vol.20, no.1, Jan 2005.

[95] F. Katriaei, M.R. Iravani, “Power management strategies for a microgrid with multiple distributed generation units,” IEEE Trans. Power Systems, vol.21, no.4, Nov 2006.

[96] Fernandez, F. D. F., Chaudhary, S., Teodorescu, R., Guerrero, J. M., Bak, C. L., Kocewiak, H., & Jensen, C. F., “Harmonic Resonances in Wind Power Plants: Modeling, Analysis and Active Mitigation Methods,” In Proceedings of the IEEE Power Tech, Eindhoven 2015.

[97] Horne, Bill G. “Progress in supervised neural networks,” Signal Processing Magazine, IEEE 10.1 (1993): 8-39.

[98] Neural Network Toolbox TM, Mathworks, URL:

http://www.mathworks.com/help/toolbox/nnet/ug/bss38ji-1.html

[99] Thomsen, B., Guerrero, J. M., & Thogersen, P. “Faroe Islands Wind-Powered Space Heating Microgrid Using Self-Excited 220 kW Induction Generator,” IEEE Transactions on Sustainable Energy, no. 5, vol. 4, 1361-1366, 2014.

[100] R. H. Lasseter, “MicroGrids,” in 2002 IEEE Power Engineering Society Winter Meeting. Conference Proceedings (Cat. No.02CH37309), vol. 1, pp. 305–308.

[101] J. M. Guerrero, P. C. Loh, T. L. Lee, and M. Chandorkar, "Advanced control architectures for intelligent microgrids—Part II: Power quality, energy storage, and

AC/DC microgrids," IEEE Transactions on Industrial Electronics, vol. 60, no. 4, 1263-1270, 2013.

[102] C. Marnay, N. Zhou, M. Qin, and J. Romankiewicz, “Lessons Learned from Microgrid Demonstrations Worldwide,” 2012.

[103] J. M. Guerrero, M. Chandorkar, T. L. Lee, P. C. Loh, Advanced control architectures for intelligent microgrids, part I: decentralized and hierarchical control. IEEE Transactions on Industrial Electronics, vol. 60, no. 4, pp. 1254-1262, 2013.

[104] D. E. Olivares, C. A. Canizares, and M. Kazerani, “A centralized optimal energy management system for microgrids,” 2011 IEEE Power Energy Soc. Gen. Meet., pp. 1–6, 2011.

[105] R. H. Lasseter, “Smart Distribution: Coupled Microgrids,” Proc. IEEE, vol. 99, no. 6, pp. 1074–1082, Jun. 2011.

[106] Yeager K.E, J.R. Willis, “Modeling of Emergency Diesel Generators in an800 Megawatt Nuclear Power Plant,” IEEE Transactions on Energy Conversion, Vol.8, No.3, September 1993.

[107] Wies, R.W., Chukkapalli, E., Mueller-Stoffels, M., “Improved frequency regulation in mini-grids with high wind contribution using online genetic algorithm for PID tuning,” PES General Meeting Conference & Exposition, 2014 IEEE, vol., no., pp.1-5, 27-31 July 2014.

[108] Power System Block set User's Guide, TEQSIM International, Inc., 2001.

[109] Shafiee Qobad, Guerrero Josep M., Quintero Juan Carlos Vasquez, “Distributed secondary control for islanded microgrids---A Novel Approach,” IEEE Trans. on Power Electronics, Vol. 29, No.2, April 2013, pp.1-14.

[110] C.L. Moreira, F.O. Resende, J.A. Pecas Lopes, “Using low voltage microgrids for service restoration,” IEEE Trans. on Power Systems, Vol. 22, No.1, February 2007, pp. 395-403.